

EXPERIMENTAL AND CFD SIMULATION OF A HELICO-AXIAL PUMP

A Dissertation

by

SUJAN REDDY GUDIGOPURAM

Submitted to the Office of Graduate and Professional Studies of
Texas A&M University

in partial fulfillment of the requirements for the degree of

DOCTOR OF PHILOSOPHY

Chair of Committee,	Gerald L. Morrison
Committee Members,	Debjyoti Banerjee
	Je-Chin Han
	Robert Randall
Head of Department,	Andreas A. Polycarpou

December 2016

Major Subject: Mechanical Engineering

Copyright 2016 Sujan Reddy Gudigopuram

ABSTRACT

Multiphase flows are encountered in the majority of crude oil wells. Electrical Submersible Pumps (ESPs) are used to pump the crude oil in wells that do not have sufficient pressure head. Conventional ESPs are mixed or radial flow pumps which have limited gas handling capabilities. For handling high GVF (Gas Volume Fraction) fluids, advanced gas handlers (a type of ESP) were used in series before the conventional ESPs. These homogenize the flow and eliminate gas lock occurrence. The behavior of ESPs (Advanced Gas Handlers) under two phase flows was not widely understood. To better understand the behavior, a helico-axial pump capable of handling fluids up to 90% GVF has been investigated.

Using the high pressure closed loop test facility at the Turbo Machinery Laboratory, a 4-stage helico-axial pump has been tested experimentally using water and air as test fluids for varying conditions such as inlet pressure, flow rate, GVF, and rotating speed. Performance maps of the pump along with vibrational characteristics have been obtained to identify the Best Efficiency Point (BEP) and stable operating regimes. The head degradation of the pump under two phase flow conditions as a function of stage has been obtained. From the head degradation results, the number of advanced gas handler stages to be used before conventional ESPs in an actual assembly has been identified to improve the total system efficiency when used in the field. Based on the experimental data, a new empirical model is developed to predict the stage by stage performance under multi-phase flow conditions.

To understand the two-phase flow behavior in the pump, flow visualization was performed on a full scale single stage pump that was designed and built using transparent Polycarbonate material. Flow visualization was performed using a laser and a high speed camera. The visualization has provided much insight into how the flow goes through the pump: showing recirculation zones, back flow, vortices, and impeller diffuser blade interaction. The bubble diameter obtained from the flow visualization is being used as one of the inputs to allow two phase CFD Simulations.

The efficiency of Advanced Gas Handlers is less than conventional ESPs. To better understand the flow behavior, 3-D single- and two-phase flow through the pump was modeled numerically using the commercial software ANSYS. The pump flow model was validated using the experimental data. From the single-phase simulations, regions of improvement were identified to increase the efficiency of the pump. Different diffuser designs were evaluated to improve the performance of the pump. Two-phase simulations are performed to study the homogeneity of the flow and to identify head degradation. Head degradation can be improved by identifying the regions where the phases tend to separate in the flow path and eliminating them.

DEDICATION

To my mother and father

ACKNOWLEDGEMENTS

I would like to thank my committee chair and advisor Dr. Gerald Morrison for all the support, encouragement and help during the course of my PhD study, I am greatly indebted to you.

I would like to thank my committee members Dr. Banerjee, Dr. Han and Dr. Randall for their comments and encouragement during the course of my PhD study.

I would like to thank Dr. Stuart Scott, Mr. Hector Casillas and Ms. Marisella Rojas from Shell Company for funding this project.

I would like to thank Mr. Jeff Miller, Mr. Kevin Scarsdale, Mr. Grant Harris, Mr. Arthur Watson and Dr. Kean Wee Cheah from Schlumberger Company for providing the pump components and training us in assembling the equipment.

I would like to thank Turbomachinery Laboratory staff, especially to Mr. Ray for his help in the machine shop. I would like to thank Naitik and Tesjasvi for introducing me to Turbo Lab.

I would like to thank my colleagues at Turbo Lab for their help in conducting experiments, special thanks to Sahand, Klayton, Joey, Craig, Yi and Peng.

Special appreciation to my friends at College Station for their help and support during my stay at College Station.

Finally I would like to thank my Mother, Father and Brother for their encouragement.

NOMENCLATURE

GVF	Gas Volume Fraction
ESP	Electrical Submersible Pump
BEP	Best Efficiency Point
BPD	Barrels per day
VFD	Variable Frequency Drive
GPM	Gallons per minute
RMSE	Root Mean Square Error
Ql	Liquid Flow rate
Qg	Gas flow rate
ρ_{mix}	Density of mixture
ρ_l	Density of liquid phase
ρ_g	Density of gas phase
α	Gas volume fraction
N	Rotating speed
p	Pressure
P	Power
d	Bubble diameter
D	Impeller diameter
h	head

TABLE OF CONTENTS

	Page
ABSTRACT	ii
DEDICATION	iv
ACKNOWLEDGEMENTS	v
NOMENCLATURE	vi
TABLE OF CONTENTS	vii
LIST OF FIGURES	ix
LIST OF TABLES	xix
1 INTRODUCTION	1
1.1 Literature Review.....	5
1.1.1 Experimental Testing.....	5
1.1.2 Flow Visualization.....	17
1.1.3 CFD Simulation	30
2 OBJECTIVES.....	41
3 METHODOLOGY.....	43
3.1 Experimental Set up.....	43
3.1.1 Test Rig	43
3.1.2 Instrumentation	51
3.1.3 Flow Visualization.....	55
3.1.4 Data Acquisition System.....	57
3.1.5 Test Matrix	59
3.2 Numerical Methodology.....	60
3.2.1 Single Phase Simulations.....	61
3.2.2 Two Phase Simulations.....	65
3.2.3 Simulation Matrix.....	70
3.3 Theory.....	71

4	RESULTS AND DISCUSSION	74
4.1	Experimental Results	74
4.1.1	Pump Performance	74
4.1.2	Effect of Inlet Pressure	77
4.1.3	Effect of Rotating Speed.....	79
4.1.4	Stage By Stage Performance	81
4.1.5	Diffuser Performance	84
4.1.6	Head Ratio	87
4.1.7	Empirical Model	88
4.1.8	Vibration Analysis.....	90
4.2	Flow Visualization	93
4.2.1	Pump Performance	93
4.2.2	Bubble Diameter	94
4.2.3	Bulk Flow Visualization.....	99
4.3	Simulation Results	104
4.3.1	Grid Independence Study.....	104
4.3.2	Single Phase Simulations.....	106
4.3.3	Two Phase Simulations.....	116
4.3.4	Different Diffuser Designs	133
5	CONCLUSIONS AND RECOMMENDATIONS	139
	REFERENCES	142

LIST OF FIGURES

	Page
Figure 1-1: Artificial lift Systems(Schlumberger 1999).....	1
Figure 1-2: ESP types (a) Radial Flow (b) Mixed Flow(Nguyen-2011).....	2
Figure 1-3: Performance of a mixed flow pump(C-72) for different inlet pressure (a) 10% GVF (b) 15% GVF (lea 1982)	4
Figure 1-4: Schematic diagram of helico-axial pump or poseidon pump(Cao 2004)	4
Figure 1-5: Changes of flow pattern under two phase flow (Murukami 1974a)	6
Figure 1-6: (a) Effect of $\Delta\Psi$, $\Delta\Psi_{imp}$, $\Delta\Psi_h$, and Ψ_a , to q_s/Q (b) Maximum allowable air for water air mixture (Murukami 1974a).....	7
Figure 1-7: (a) Pump Performance Map for P3, P5and P7 impeller blades (b) Comparison of Performance Map for Different Impeller Blades (Murukami 1974b)	8
Figure 1-8: a. Head flow rate curve for 100 psig inlet pressure for I-42B pump b. Effect of Speed and Inlet pressure on I-42B pump for 20%GVF (lea 1982)	9
Figure 1-9: Pressure flow rate curve using Diesel/CO ₂ Mixture, 10% Vol CO ₂ for different inlet pressure (a) K-70 Pump (b) C-72 Pump	9
Figure 1-10: Head flow rate curve for different number of stages at 200 psig inlet pressure, 15% GVF and 4000 BPD liquid flow rate (Cirilo 1998).....	11
Figure 1-11: (a) Pressure rise as a function of Liquid flow rate and Stage number for gas flow rate of 15 Mscf/D (b) Pressure rise as a function of Liquid and gas flow rate (Rui 2003)	13
Figure 1-12: (a) Effect of Rotating Speed on GVF versus pressure rise (b) Effect of rotating speed on GVF versus efficiency (Zhang 2011).....	15

Figure 1-13: Performance of the pump for 100 psig Inlet pressure, 3600 RPM (Kirkland 2012)	16
Figure 1-14: (a) Flow pattern in Impeller near the limit of pumping action (b) Effect of Pump speed on Bubble diameter(Murukami 1974a).....	17
Figure 1-15: Location of electrical resistivity probes in the impeller (Sekoguchi 1984).....	18
Figure 1-16: Pump performance map for different GVF (Sekoguchi 1984).....	19
Figure 1-17: Flow Pattern in the Impeller for (a) $\beta=0.0116$ (b) $\beta=0.0497$ (c) $\beta=0.0497$ at Break Down (Sekoguchi 1984)	20
Figure 1-18: Slip ratio as a function of GVF for different liquid flow rates (Sekoguchi 1984).....	21
Figure 1-19: Different two phase flow regimes in impeller passages (Chisley 1997).....	22
Figure 1-20: Gas accumulation in the impeller (a) Low gas content (b) Medium gas content (c) High gas content (d) Flow separation (Poullikkas 2003)	24
Figure 1-21: Two stage ESP setup (Barrios 2007).....	25
Figure 1-22: (a) Two phase flow through Impeller for 250 BPD liquid flow rate (b)Gas Pocket Formation in impeller at 175 BPD liquid flow rate for 600RPM, and 0.15 scf/hr gas flow rate (Barrios 2007)	26
Figure 1-23: Variation of bubble diameter for different operating conditions at the onset of surging (Barrios 2007).....	26
Figure 1-24: Schematic view of the ESP pump (Gamboa 2009).....	27
Figure 1-25: (a) Effect of gas density on pressure rise (b) Effect of surface tension on pressure rise at 2 psig, 600 rpm, $q_{ld} = 0.6$ (Gamboa 2009).....	27
Figure 1-26: Impeller flow patterns for 2 psig, 600 rpm and $q_{ld} = 0.6$ (Gamboa 2009).....	28

Figure 1-27: Performance map using oil and air for different viscosities at 15 Hz (Trevisan 2009).....	30
Figure 1-28: Pressure distribution on the pump with volute and circular casing at mid span (Majidi 2000).....	32
Figure 1-29: Velocity vector at different cross sections of the volute (Majidi 2000)	33
Figure 1-30: Liquid phase distribution in the impeller for (a) 1300 BPD, 10%GVF (b)2100 BPD, 10%GVF (c)1700 BPD, 10%GVF (d)2100 BPD, 17%GVF (Caridad 2002).....	36
Figure 1-31: Pump performance for (a) Single phase flow (b) 10% GVF, bubble diameter = 0.1 mm (c) 15% GVF, bubble diameter = 0.1 mm (d) 17% GVF, bubble diameter = 0.1 mm (Caridad et al. 2004).....	37
Figure 1-32: Air volume fraction for 500 BPD, 1500 RPM at (a) 0.05% GVF (b) 0.1% GVF (Barrios 2007)	38
Figure 1-33: Air volume fraction for 25 kBPD flow rate and 25% GVF (Marsis 2013)	39
Figure 1-34: Different diffuser design with corresponding pressure rise (Marsis et al. 2013).....	40
Figure 3-1: P&ID diagram of the Experimental Setup.....	44
Figure 3-2: a. Picture of Stainless Steel Tank b. Picture of Fischer valve c. Picture of Tee's	45
Figure 3-3: a. Reciprocating Pump b. Oil Pump and Heat Exchanger	45
Figure 3-4: Transparent Window in a. Water Line b. Air Line.....	46
Figure 3-5: Secondary Loop with Pump, filter and Heat exchanger	46
Figure 3-6: 3-D model of Impeller, Different Views	47
Figure 3-7: 3-D model of Diffuser.....	48

Figure 3-8: a. Single Stage pump b. 4-Stage Pump Assembly c. Cross Sectional View of 4-Stage Pump	48
Figure 3-9: Test rig Picture with pump.....	49
Figure 3-10: Picture of Clear Pump Impeller a. Front View B. Top View	50
Figure 3-11: Picture of Clear Pump Diffuser a. Front View B. Top View.....	50
Figure 3-12: Picture of Clear Pump a. Impeller-Diffuser with Casing b. Test rig.....	51
Figure 3-13: Line diagram of the pump with different instruments.....	53
Figure 3-14: Static Pressure Taps on Diffuser	54
Figure 3-15: Phantom V711 High Speed Camera.....	56
Figure 3-16: a. LSR 532H-1W laser b. High Intensity Fiber light source.....	57
Figure 3-17: Screen Shot of Front Panel Window of Performance VI in LabVIEW	58
Figure 3-18: Screen Shot of Front Panel Window of Vibration Monitoring VI in LabVIEW	59
Figure 3-19: Flow path a. Impeller b. Diffuser	60
Figure 3-20: Mesh a. Impeller b. Diffuser c. Impeller tip clearance.....	61
Figure 3-21 a. Inlet Body Flow Domain b. Pump First Stage Flow Domain c. Zone numbers on mixer body outlet	69
Figure 4-1: Performance map of the 4-stage pump at 100 psig inlet pressure, 3600 RPM (a) Total dP (b) Total head (c) Power (d) Efficiency	75
Figure 4-2: System Curve of the test rig.....	76

Figure 4-3: Performance map comparison of the 4-stage pump at 300 psig and 40 psig Inlet Pressure, 3600 RPM (a) Total dP (b) Total head (c) Power (d) Efficiency	78
Figure 4-4: Performance map comparison of the 4-stage pump at 100 psig inlet pressure, 3600 RPM and 3000 RPM (a) Total dP (b) Total head (c) Power (d) Efficiency	79
Figure 4-5: Comparison of pressure rise from affinity laws and experimental data for 3600 RPM. (a) 1 st Stage (b) Total dp.....	81
Figure 4-6: Comparison of VFD power from affinity laws and experimental data for 3600 RPM.....	81
Figure 4-7: Stage by stage head versus stage inlet total flow rate comparison at 200 psig inlet pressure, 3600 RPM (a) 1 st Stage (b) 2 nd Stage (c) 3 rd Stage (d) 4 th Stage	82
Figure 4-8: GVF variation in the pump for different inlet GVF at 200 psig inlet pressure, 20 kBPD liquid flow rate, 3600 RPM	83
Figure 4-9: Temperature variation in the pump for different inlet GVF at 200 psig inlet pressure, 20 kBPD liquid flow rate, 3600 RPM	84
Figure 4-10: Pressure variation in the pump for different liquid flow rates at 100 psig inlet pressure, 3600 RPM (a) 0% GVF (b) 20% GVF	85
Figure 4-11: Pressure variation in 1 st stage diffuser across different planes at 100 psig Inlet pressure, 3600 RPM, 0%GVF (a) 10 kBPD liquid flow rate (b) 20 kBPD liquid flow rate (c) 30 kBPD liquid flow rate (d) 40 kBPD liquid flow rate	86
Figure 4-12: Stage by stage head ratio versus stage inlet GVF comparison at 100psig inlet pressure, 3600 RPM (a) 1 st stage (b) 2 nd stage (c) 3 rd stage (d) 4 th stage.....	88
Figure 4-13: Comparison of experimental head and empirical model head for different rotating speeds.....	89

Figure 4-14: Orbit plots of the shaft for flow conditions of 200psig inlet pressure, 3600 RPM, 10 kBPD liquid flow rate a) 0% GVF b) 70% GVF	91
Figure 4-15: Peak to peak amplitude of the shaft at 60 Hz for 1 st stage diffuser X-direction proximity probe at 200 psig inlet pressure and 3600 RPM.	92
Figure 4-16: Peak to peak amplitude at 60 Hz for inlet flange spiral axis accelerometer data at 200 psig inlet pressure and 3600 RPM.....	92
Figure 4-17: Performance map of the single stage pump at 50 psig inlet pressure, 1800 RPM	93
Figure 4-18: Schematic of the laser and camera.....	94
Figure 4-19: a. Captured image b Processed Image of impeller at 8.7 kBPD liquid flow rate, 50 psig inlet pressure and 1800 RPM	95
Figure 4-20: Output of processed Images from INSIGHT 4G software for flow conditions of 1800 RPM, 50psig inlet pressure and 8.7 kBPD liquid flow rate a. Bubble diameter histogram b. Average bubble diameter per frame c. Bubble velocity histogram d. Average bubble velocity per frame	96
Figure 4-21: Schematic of the laser and camera for high GVF flow.....	97
Figure 4-22: Captured image in Impeller at 8.7 kBPD liquid flow rate, 6% GVF, 50 psig inlet pressure and 1800 RPM.....	98
Figure 4-23: Variation of bubble diameter versus total flowrate at 50 psig inlet pressure, 1800 RPM	99
Figure 4-24: Picture and halogen lamp and camera	100
Figure 4-25: Video of the impeller flow field at 1800 RPM, 50 psig inlet pressure, 8.7 kBPD liquid flow rate and 2% GVF.....	101
Figure 4-26: Video of the impeller flow field at 1800 RPM, 50 psig inlet pressure, 8.7 kBPD liquid flow rate and 8% GVF.....	101

Figure 4-27: Schematic of the flow	102
Figure 4-28: Video of the diffuser flow field at 1800 RPM, 50 psig inlet pressure, 8.7 kBPD liquid flow rate and 2% GVF.....	103
Figure 4-29: Video of the diffuser flow field at 1800 RPM, 50 psig inlet pressure, 12 kBPD liquid flow rate and 2% GVF.....	104
Figure 4-30: Effect of Number of elements Vs Percentage change in dP for flow conditions of 30 kBPD liquid flow rate and 3600 RPM	105
Figure 4-31: Performance comparison of simulation and experimental results for 1 st stage	107
Figure 4-32: Pressure rise versus time step at 35 kBPD liquid flow rate, 3600 RPM.....	107
Figure 4-33: Performance comparison of simulation and experimental results for 2 nd stage using periodic boundary conditions.....	109
Figure 4-34: Performance comparison of simulation and experimental results for 2 nd stage using velocity inlet and pressure outlet as boundary condition	109
Figure 4-35: Static pressure variation along the stream wise location in a single stage pump for the flow conditions of 25 kBPD liquid flow rate, 3600 RPM	110
Figure 4-36: Stream lines for the flow conditions of 25 kBPD liquid flow rate, 3600 RPM at span=0.1 (a) 1st Stage (b) Second Stage	110
Figure 4-37: Pressure variation on 1 st stage impeller blade for flow conditions of 25 kBPD liquid flow rate, 3600 RPM at span = 0.98.....	112
Figure 4-38: Velocity vectors at different stream wise locations for flow conditions of 25 kBPD liquid flow rate, 3600 RPM. (a) 0.13 stream wise location (b) 0.65 stream wise location	113
Figure 4-39: Stream lines of the 2 nd Stage fluid domain for flow conditions of 15 kBPD liquid flow rate, 3600 RPM using Periodic Boundary Conditions (a) span = 0.1 (b) span = 0.5 (c) span = 0.9	114

Figure 4-40: Stream lines of the 2 nd stage fluid domain for flow conditions of 35 kBPD liquid flow rate, 3600 RPM using periodic boundary conditions (a) span = 0.1 (b) span = 0.5 (c) span = 0.9	114
Figure 4-41: Stream lines of the 2 nd stage fluid domain for flow conditions of 15 kBPD liquid flow rate, 3600 RPM using velocity inlet and pressure outlet as boundary condition (a) span = 0.1 (b) span = 0.5 (c) span = 0.9	115
Figure 4-42: Stream lines of the 2 nd stage fluid domain for flow conditions of 35 kBPD liquid flow rate, 3600 RPM using velocity inlet and pressure outlet as boundary condition (a) span = 0.1 (b) span = 0.5 (c) span = 0.9	116
Figure 4-43: Inlet Body air volume fraction contours for the flow conditions of 20 kBPD liquid flow rate, 3600 RPM (a) 10% GVF (b) 50% GVF	118
Figure 4-44: Inlet Body stream lines for the flow conditions of 20 kBPD liquid flow rate, 50% GVF and 3600 RPM. (a) Air (b) Water	119
Figure 4-45: Zone wise mass flow rate variation at outlet of inlet body for the flow conditions of 20 kBPD liquid flow rate, 50% GVF and 3600 RPM	119
Figure 4-46: Zone wise variation of air volume fraction at outlet of inlet body for the flow conditions of 20 kBPD liquid flow rate, 50% GVF and 3600 RPM	120
Figure 4-47: Two phase performance comparison of simulation and experimental results for 1 st stage	121
Figure 4-48: Two phase performance comparison of simulation and experimental results for 2 nd stage	122
Figure 4-49: 1 st stage air volume fraction contours for the flow conditions of 20 kBPD liquid flow rate, 50% GVF, 200 psig inlet pressure and 3600 RPM (a) Impeller Inlet (b) Impeller-Diffuser Interface (c) Diffuser Outlet	123
Figure 4-50: 1 st stage velocity vectors at diffuser outlet for the flow conditions of 20 kBPD liquid flow rate, 50% GVF, 200 psig inlet pressure and 3600 RPM (a) Water velocity (b) Air velocity	123

Figure 4-51: 1 st stage cascade of air volume fraction contours for the flow conditions of 20 kBPD liquid flow rate, 50% GVF, 200 psig inlet pressure and 3600 RPM (a) Span = 0.1 (b) Span = 0.5 (c) Span = 0.9	124
Figure 4-52: 1 st stage cascade of air velocity stream lines for the flow conditions of 20 kBPD liquid flow rate, 50% GVF, 200 psig inlet pressure and 3600 RPM (a) Span = 0.1 (b) Span = 0.5 (c) Span = 0.9	125
Figure 4-53: Pressure variation on 1 st stage impeller blade for the flow conditions of 20 kBPD liquid flow rate, 50% GVF, 200 psig inlet pressure and 3600 RPM at span = 0.5.....	125
Figure 4-54: 1 st stage cascade of air volume fraction contours for the flow conditions of 20 kBPD liquid flow rate, 10% GVF, 200 psig inlet pressure and 3600 RPM (a) Span = 0.1 (b) Span = 0.5 (c) Span = 0.9	127
Figure 4-55: 1 st stage cascade of air velocity stream lines for the flow conditions of 20 kBPD liquid flow rate, 10% GVF, 200 psig inlet pressure and 3600 RPM (a) Span = 0.1 (b) Span = 0.5 (c) Span = 0.9	127
Figure 4-56: 1st stage cascade of air velocity stream lines for the flow conditions of 200 psig inlet pressure and 3600 RPM at span=0.1 for (a) 30 kBPD liquid flow rate, 10% GVF (b) 20 kBPD liquid flow rate, 40% GVF	128
Figure 4-57: 1st stage cascade of air volume fraction contours for the flow conditions of 200 psig inlet pressure and 3600 RPM at span=0.1 for (a) 30 kBPD liquid flow rate, 10% GVF (b) 20 kBPD liquid flow rate, 40% GVF.....	129
Figure 4-58: Cascade of air velocity stream lines at span=0.1 for the flow conditions of 25 kBPD liquid flow rate, 20% GVF, 200 psig inlet pressure and 3600 RPM (a) 1 st stage (b) 2 nd stage.....	130
Figure 4-59: Cascade of air volume fraction contours at span=0.1 for the flow conditions of 25 kBPD liquid flow rate, 20% GVF, 200 psig inlet pressure and 3600 RPM (a) 1 st stage (b) 2 nd stage.....	131
Figure 4-60: Cascade of air velocity contours at span=0.1 for the flow conditions of 25 kBPD liquid flow rate, 20% GVF, 200 psig inlet pressure and 3600 RPM (a) 1 st stage (b) 2 nd stage.....	131

Figure 4-61: 2 nd stage cascade of air volume fraction contours for the flow conditions of 28% GVF, 215 psig inlet pressure and 3600 RPM at span=0.1 for different liquid flow rates (a) 20 kBPD (b) 30 kBPD	132
Figure 4-62: 2 nd stage cascade of air velocity stream lines for the flow conditions of 28% GVF, 215 psig inlet pressure and 3600 RPM at span=0.1 for different liquid flow rates (a) 20 kBPD (b) 30 kBPD	133
Figure 4-63: Pressure rise comparison for three different designs	135
Figure 4-64: Design-2 2 nd stage cascade of water velocity stream lines for the flow conditions of 35 kBPD liquid flow rate and 3600 RPM (a) Span = 0.1 (b) Span = 0.5 (c) Span = 0.9	135
Figure 4-65: Design-3 2 nd stage cascade of water velocity stream lines for the flow conditions of 35 kBPD liquid flow rate and 3600 RPM (a) Span = 0.1 (b) Span = 0.5 (c) Span = 0.9	136
Figure 4-66: 2 nd stage cascade of water velocity stream lines for the flow conditions of 15 kBPD liquid flow rate and 3600 RPM at span=0.5 (a) Standard (b) Design-1 (c) Design-2.....	136
Figure 4-67: Power consumption comparison for three different designs	137
Figure 4-68: Efficiency and Pressure gradient comparison for three different designs at 35kBPD liquid flow rate.....	138

LIST OF TABLES

	Page
Table 3-1: List of Different Flow Meters	52
Table 3-2: List of Pressure Transducers and Specifications	54
Table 3-3: List of Thermocouples and Specifications	55
Table 3-4: Details of Accelerometer and Proximity Probes	55
Table 3-5: Specifications of Phantom V711 High Speed Camera.....	56
Table 3-6: List of Different Modules Used for DAS.....	57
Table 3-7: Test Matrix for 4-Stage Pump	59
Table 3-8: Test Matrix for Single Stage Clear Pump.....	60
Table 4-1: Mesh Sizes for Different Models.....	105

1 INTRODUCTION

With the increasing demand for oil products globally there is a need to efficiently recover the crude oil from wells. Artificial lift is a way to continue producing crude oil from wells where the bottom hole pressure is not sufficient to overcome the pressure losses that occur along the flow path from oil well to the production platform. Artificial lift is used to reduce the pressure losses or increase the static pressure of the fluid being pumped. Several common artificial lift systems are shown in Figure 1-1. From left to right are Rod Pump, Hydraulic Pump, Electric Submersible Pump, and Gas lift.

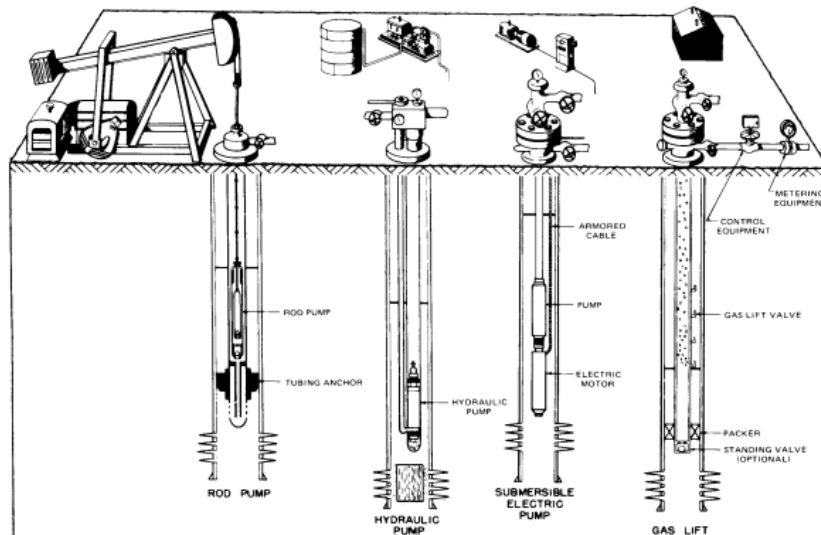


Figure 1-1: Artificial lift Systems(Schlumberger 1999)

A Rod Pump system is the oldest type where pieces of rod are connected together from the surface to the down hole pump. The rod can have either rotatory

motion or oscillatory motion depending on the type of down hole pump. Hydraulic pumping systems utilize a pressurized hydraulic fluid from the surface to run a hydraulic pump located down hole which is used for pumping crude oil. In continuous gas lift, high pressure gas is injected to the bottom of the well and used to reduce mixture density, therefore reducing flow losses occurring along the flow path. In Intermittent gas lift, large volumes of gas at high pressure are periodically injected in to the well to push the liquid that has accumulated in the bottom of the well to the surface. In an Electric Submersible Pump (ESP), power from the surface is used to run an electric motor connected with a centrifugal pump stacked in series. ESP's are typically used for pumping high flow rates from deep oil wells.

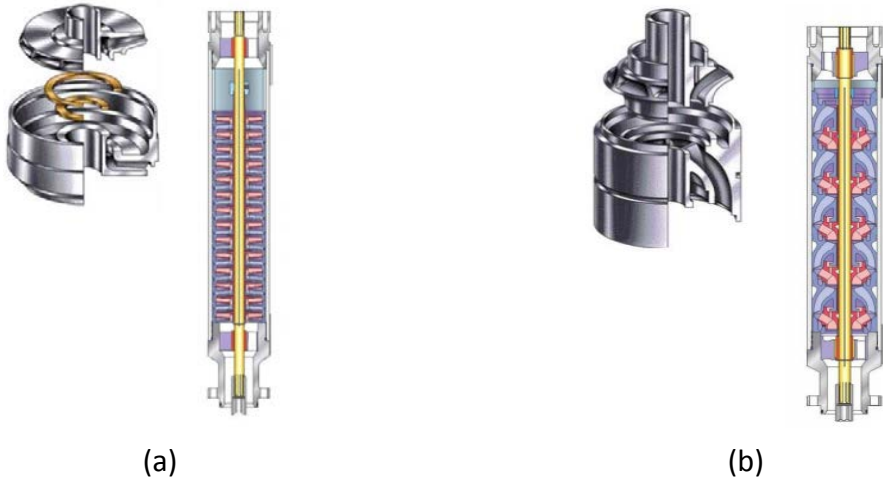


Figure 1-2: ESP types (a) Radial Flow (b) Mixed Flow(Nguyen-2011)

A typical centrifugal pump consists of a rotating impeller which is used to transfer kinetic energy to the fluid and a stationary diffuser which converts kinetic

energy to pressure head. The performance of an ESP depends on the type of pump used. Common ESP pumps have radial or mixed flow impellers.

Radial flow pumps, as shown in Figure 1-2(a), are low specific speed pumps where the head is generated with pure centrifugal action. In a radial flow pump, flow enters axially in to the impeller and leaves radially from the impeller outlet. The flow is redirected in the diffuser where the flow enters axially in the next stage impeller. Radial flow pumps are susceptible to higher head degradation with the introduction of free gas(Lea 1982). With increase in the gas content, gas bubbles occupy a major portion of the impeller flow area until gas lock occurs(Barrios 2007). Radial flow pumps are limited to a maximum flow rate of 3000 BPD.

Mixed flow pumps, as shown in Figure 1-2(b), are used to generate head based on a combination of centrifugal action and impeller design. These pumps have higher specific speeds. Mixed flow pumps perform slightly better in comparison with radial flow pumps under multi-phase flow conditions (Lea(1982) and Cirilo(1998)). With Increase in GVF based on inlet pressure and rotating speeds initially head degradation occurs as shown in Figure 1-3(a), followed by surging as shown in Figure 1-3(b)and finally gas lock where pumping action stops.

The main reason for surging is the separation of phases caused by high centrifugal forces in mixed and radial flow impellers under multi-phase flow conditions. For better performance of the pumps under multi-phase flow conditions, advanced gas handlers were developed. Advanced gas handlers are used between the ESP stages and

the pump inlet. One of the advanced gas handler is a helico-axial Pump or Poseidon Pump as shown in Figure 1-4.

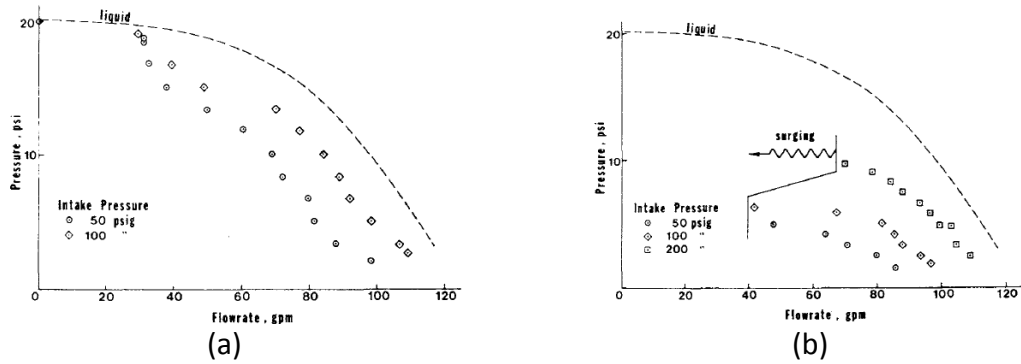


Figure 1-3: Performance of a mixed flow pump(C-72) for different inlet pressure (a) 10% GVF (b) 15% GVF (Iea 1982)

These are used for homogenization of flow under multi-phase flow conditions.

The Poseidon Project was initiated in the 1987 by Total, Statoil and IFP with first prototype tested in the 1992.

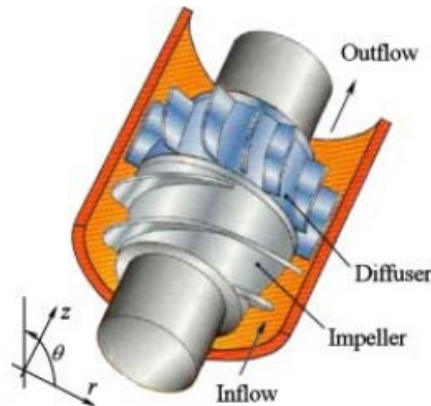


Figure 1-4: Schematic diagram of helico-axial pump or poseidon pump(Cao 2004)

In these pumps, the head is generated based on lifting action and not by centrifugal forces. Helico-axial pumps can handle high gas content flows (Zhang 2011), since low centrifugal forces causes very low radial velocities thereby preventing phase separation and gas lock in the impellers and effectively mixing two phases.

1.1 Literature Review

The literature review is divided into three sections covering experimental work, flow visualization and CFD simulations.

1.1.1 Experimental Testing

Initial studies on the performance of a centrifugal pump under two phase flow conditions were carried out by Murukami et al. (1974a). Experiments were carried out in a semi-open impeller low specific speed pump with a transparent casing to study the performance and behavior of entrained gas bubbles. The pump specifications were BEP at 8200 BPD and 1750 RPM, Specific speed 179. According to the author, the head loss ($\Delta\Psi$) under two phase flow is a combination of head loss in compressing air (Ψ_a), hydraulic flow losses ($\Delta\Psi_h$) and decrement of head developed by impeller ($\Delta\Psi_{imp}$). For $GVF < 4\%$ there was no considerable drop in the head developed by the impeller. For $GVF > 4\%$ there was a considerable drop in the head developed by the impeller because the bubbles disturb the flow condition. Figure 1-5 describes the changes in the flow pattern and velocity triangle due to presence of air bubbles.

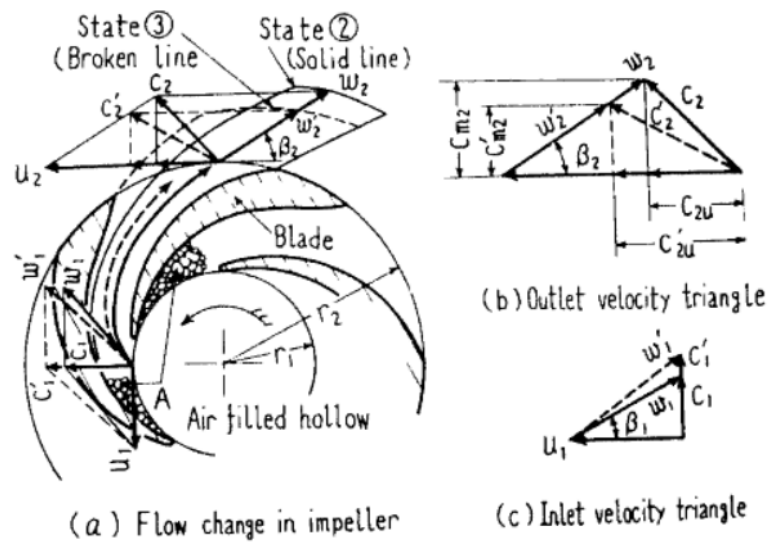
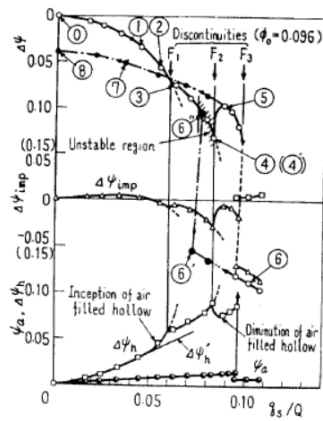


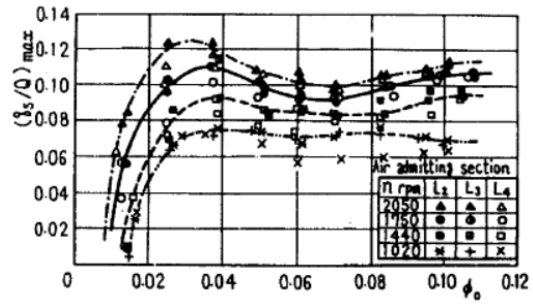
Figure 1-5: Changes of flow pattern under two phase flow (Murukami 1974a)

When $GVF < 2\%$ the head loss was mainly caused by the work used in compressing air, for $GVF > 2\%$ the hydraulic losses increase in comparison with the work used for compressing air. Figure 1-6a shows the variation in head loss for different GVF. From this graph, there is no variation in the head developed by the impeller under low GVF conditions. With increasing GVF, there are discontinuities in the head losses due to the changes in the flow pattern of the impeller.

Figure 1-6b shows the variation of maximum allowable air under two phase flow for different speeds. As the speed increases, GVF increases due to the fact that air is broken into finer bubbles at higher speeds by the impeller.



(a)



(b)

Figure 1-6: (a) Effect of $\Delta\Psi$, $\Delta\Psi_{imp}$, $\Delta\Psi_h$, and Ψ_a , to q_s/Q (b) Maximum allowable air for water air mixture (Murukami 1974a)

Murukami et al. (1974b) studied the effect of the number of impeller blades on pump performance under two phase flow conditions. Experiments were carried out using semi-open low specific speed impellers having three, five and seven blades. Figure 1-7(a) shows the performance map for different impeller blades, where Ψ , Φ and μ are non-dimensional head, liquid flow rate and power, η is the efficiency, Q is liquid flow rate and q_s is gas flow rate. For the pumps having five and seven blades on the impeller the pump performance under two phase flow conditions is independent of the number of blades. When the number of impeller blades are three, unevenness of flow was observed for low GVF (<3.5%) due to which the head developed increases in comparison with no gas conditions as shown in Figure 1-7(b). As the GVF is increased the unevenness of flow reduces. As the number of impeller blades increase, the maximum GVF delivered by the pump increases due to fact that the bubbles are broken in to finer particles at the entrance of the impeller. Based on the experimental

data, the author has developed correlations to predict pump head, flow rate, power and efficiency under two phase flow conditions. These correlations hold well for $GVF < 6\%$ and large flow rates.

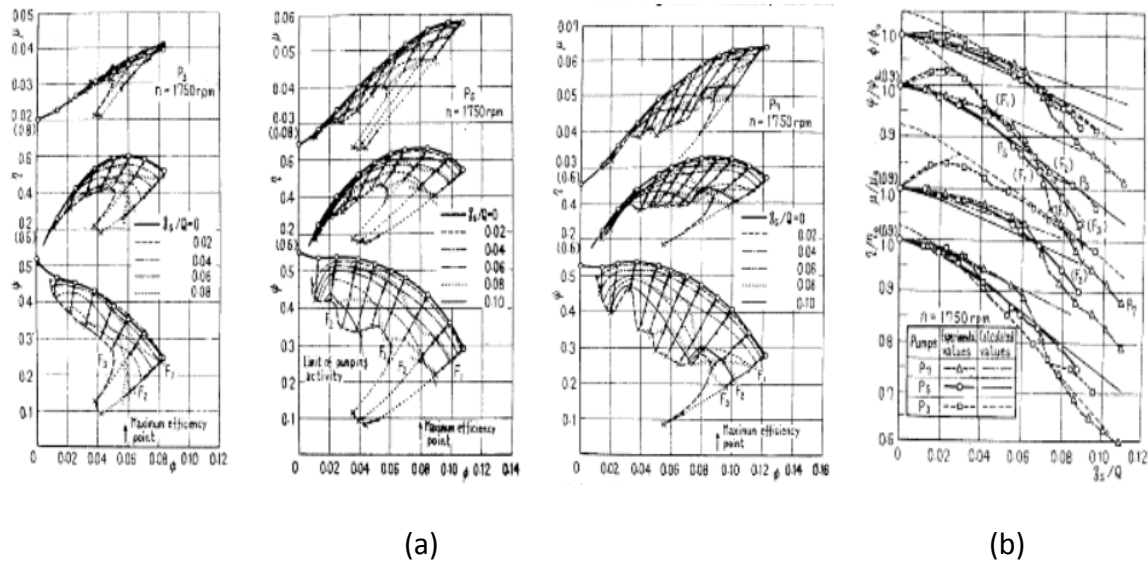


Figure 1-7: (a) Pump Performance Map for P3, P5 and P7 impeller blades (b) Comparison of Performance Map for Different Impeller Blades (Murukami 1974b)

Lea et al. (1982) were the first to report the performance of an ESP under two phase flow conditions. The authors carried out performance evaluation for three different types of ESPs namely the I-42 (1500 BPD optimal flow), K-70 (2750 BPD optimal flow), and C-72 (2500 BPD optimal flow) by varying inlet pressure, speed, and GVF. The working medium used was Diesel/ CO_2 and Water/Air. Diesel/ CO_2 was used as the test fluid to simulate the effect of gas solubility present in an actual working medium. Figure 1-8 shows the performance of an I-42B pump using Diesel/ CO_2 as working medium. From Figure 1-8(a), surging is observed for flows above 15% GVF.

With increase of GVF the head drops considerably in comparison with liquid flow rate.

Figure 1-8(b) shows the effect of speed and inlet pressure for 20% GVF flow.

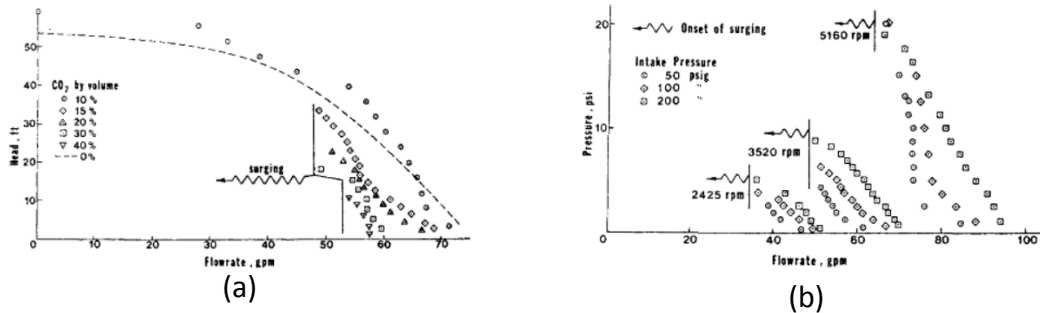


Figure 1-8: a. Head flow rate curve for 100 psig inlet pressure for I-42B pump b. Effect of Speed and Inlet pressure on I-42B pump for 20%GVF (lea 1982)

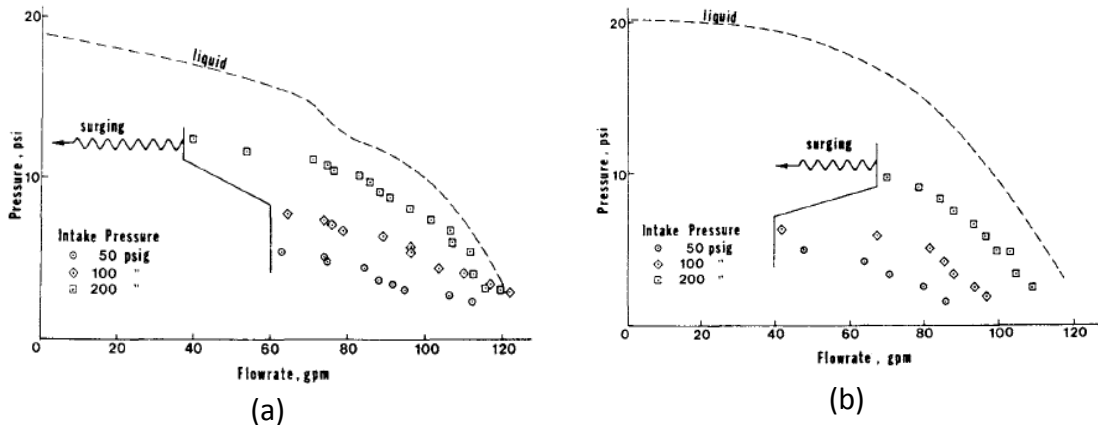


Figure 1-9: Pressure flow rate curve using Diesel/CO₂ Mixture, 10% Vol CO₂ for different inlet pressure (a) K-70 Pump (b) C-72 Pump

Figure 1-9 shows the performance comparison of two different pumps K-90 and C-72. K-90 has a mixed flow design and C-72 has a radial flow design. From the figure, the mixed flow pump has lesser pressure deterioration in comparison with the liquid only curve. According to the author, using a highly mixed flow or axial flow pump increases gas handling capabilities.

Turpin et al. (1986) developed correlations to predict the head developed under two phase flow conditions for the results presented by Lea (1982). He assumed that the head developed is only a function of flow rate, GVF, and inlet pressure. These correlations are specific to particular pump and there was no theoretical background. The head developed by the I-42 and K-70 pumps is given by the Equation 1-1

$$\frac{H}{H_{Sp}} = e^{-a(q_s/Q)} \quad 1-1$$

Where H is head with gas-liquid flow, H_{Sp} is head with single phase liquid flow, q_s is volumetric flow rate of gas at pump suction, Q is volumetric flow rate of gas at pump suction and 'a' is given by the Equation 1-2

$$a = \frac{346430}{P_s^2} \left(\frac{q_s}{Q} \right) - \frac{410}{P_s} \quad 1-2$$

Where P_s is the pressure at the pump suction location.

Head developed by the C-72 pump is given by Equation 1-3

$$\frac{H}{H_{Sp}} = e^{-a(q_s/Q)} [1 - 0.0258(Q - Q_D) + 0.00275(Q - Q_D)^2 - 0.0001(Q - Q_D)^3] \quad 1-3$$

Where Q_D is total volume flow rate at P_s which is given by the Equation 1-4 and 'a' is given by Equation 1-5.

$$Q_D = 98.3 - 33.3\phi \quad 1-4$$

$$a = \frac{285340}{P_a^2} \left(\frac{q_s}{Q} \right) \quad 1-5$$

The above equations hold good when Φ is close to 1 and deteriorates rapidly when the value of Φ exceeds 1.

Cirilo (1998) performed multi-phase performance evaluation of three different pumps (2100 BPD, 4000 BPD and 7000 BPD BEP liquid only flow rate) for varying inlet pressure, speed, and number of stages of the pump using water and air as test fluids. It was observed that with an increase in inlet pressure the ability of pump to handle gas percentage increased.

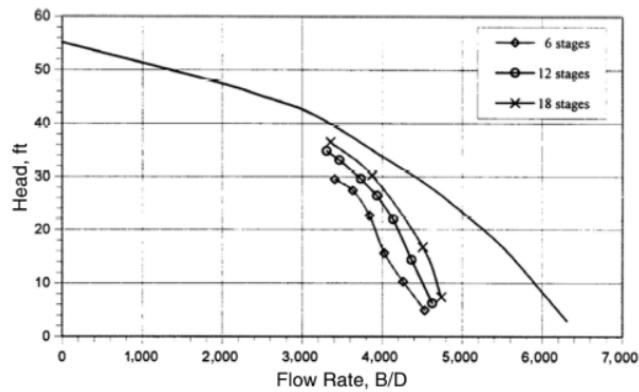


Figure 1-10: Head flow rate curve for different number of stages at 200 psig inlet pressure, 15% GVF and 4000 BPD liquid flow rate (Cirilo 1998)

There was no considerable change in gas handling capability as the speed was varied from 2700 to 3600 RPM. As the stages of the pump were added on, it was observed that the average head of the pump increased for two phase flow conditions. The change was attributed to the fact that flow becomes more homogenized and the volume of the gas decreases as the flow traverses through the pump resulting in

decreasing local GVF. Figure 1-10 shows the head flow rate curve for different stages for 15% GVF and 4000 BPD liquid flow rate at the pump inlet.

Based on the experimental data, a correlation (Equation 1-6) has been developed to determine the maximum GVF (λ_g) for stable operation of the pump.

$$\lambda_g = 0.0187p_i^{0.4342} \quad 1-6$$

Romero (1999) was the first to test a 12-stage ESP which was designed for handling two phase flows with liquid only BEP at 4000 BPD flow rate. A slotted impeller was designed to increase the amount of GVF the pump can handle. Based on the performance data, correlations have been developed to predict the head produced under two phase flow conditions. Equation 1-7 predicts the non-dimensional head developed under two phase flow conditions

$$H_d = \left(1 - \frac{q_d}{q_{dmax}}\right) \left[a \left(\frac{q_d}{q_{dmax}} \right)^2 + \frac{q_d}{q_{dmax}} + 1 \right] \quad 1-7$$

Where H_d is dimensionless head per stage, q_d is dimensionless liquid flow rate, and q_{dmax} are calculated using Equations 1-8 and 1-9 and λ_g is the GVF

$$a = 2.902\lambda_g + 0.2751 \quad 1-8$$

$$q_{dmax} = 1 - 2.0235\lambda_g \quad 1-9$$

The minimum liquid flow rate under which surging occurs is given by Equation 1-10

$$q_{dlim} = -6.6465\lambda_g^2 + 3.5775\lambda_g + 5.4e^{-3} \quad 1-10$$

Pessoa (2003) performed experiments on a 22 stage mixed flow ESP to map the performance data with two phase flow conditions using air and water as test fluids with liquid only BEP at 7000 BPD and 3600 RPM. The pressure rise across each stage was measured instead of average pressure rise across each stage as shown in Figure 1-11(a). The pressure rise across each stage increases as the flow traverses through the pump. Figure 1-11(b) shows the dimensionless pressure rise as a function of liquid and gas flow rates, the change of slope corresponds to the surging point for each gas flow rate in comparison to the liquid only curve. To the left of the surging point, the minimum point is the condition of gas lock.

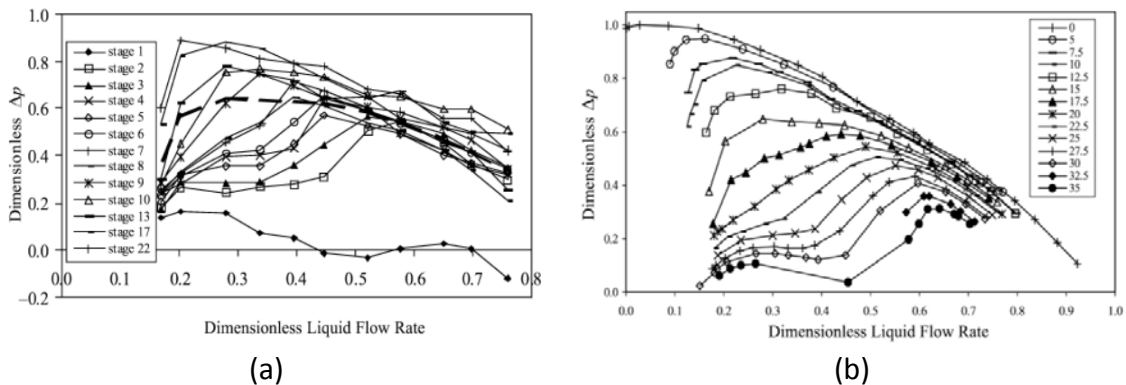


Figure 1-11: (a) Pressure rise as a function of Liquid flow rate and Stage number for gas flow rate of 15 Mscf/D (b) Pressure rise as a function of Liquid and gas flow rate (Rui 2003)

Duran et al. (2003) performed multiphase modeling and experimentation on a 22 stage commercial mixed flow ESP with liquid only BEP at 6100 BPD and 3500 RPM. Detailed measurements were carried out on the 10th stage for modeling purpose. A drift flux model was used to correlate the performance for small no-slip GVF conditions and the bubbly flow regime using Equation 1-11.

$$\Delta P = (1 - \alpha)\rho_l H \left\{ \frac{q_l}{(1 - \alpha)} \right\} + \alpha\rho_g H \left\{ \frac{q_g}{\alpha} \right\} \quad 1-11$$

Where α is no slip GVF, q_l and q_g are in situ liquid and gas flow rates ρ_l and ρ_g are liquid and gas densities and H is liquid stage head

For bubbly flow regime, q_g is obtained using Equation 1-12. During this regime the head degradation is minimal.

$$q_g = \left(a \frac{\rho_m}{\rho_l} + b \right) * (q_l)^c \quad 1-12$$

Where ρ_m is the density of the mixture under two phase flow conditions, and a, b, and c are constants

Using Equations 1-11 and 1-12 the pressure rise under two phase flow conditions can be expressed as a function of GVF.

Equation 1-11 doesn't hold well for the elongated bubble flow regime where severe head degradation will be observed in the pump. For this regime, the pressure rise can be correlated using Equation 1-13

$$\Delta P = a + b * \ln(q_g) \quad 1-13$$

Where a and b are constants.

Zhou et al. (2010) presented an improved empirical model for the experimental data of Lea et al. (1982). The model is used to evaluate head rise per stage under two phase flow conditions using the equation

$$\frac{H_m}{H_{max}} = K(C_1 p_{in})^{\alpha E1} + (1 - \alpha)^{E2} + \left(1 - \frac{q_l}{(1 - \alpha)q_{max}} \right)^{E3} \quad 1-14$$

Where H_m is the stage head, H_{max} is the maximum head of the pump, q_{max} is the maximum flow rate of the pump, p_{in} is inlet pressure, α is GVF, q_l is liquid flow rate and C_1 is conversion factor. K , E_1 , E_2 , E_3 are constants and are pump dependent.

Zhang (2011) performed multi-phase experiments on a 5-stage helico-axial pump with liquid only BEP at 7500 BPD, 4500 RPM using water and air as test fluids. Performance of the pump was evaluated for different speed and GVF at 30psi inlet pressure. Due to its impeller blade which is spiral in shape, these pumps were able to handle high GVF without liquid gas separation. These pumps are typically designed for high GVF flows. Figure 1-12(a) shows the variation of Pressure rise Vs GVF for different rotating speeds. The efficiency of these pumps is typically lower since the main function of the pump is to homogenize the flow. Figure 1-12(b) shows the variation of Efficiency Vs GVF for different rotating speeds.

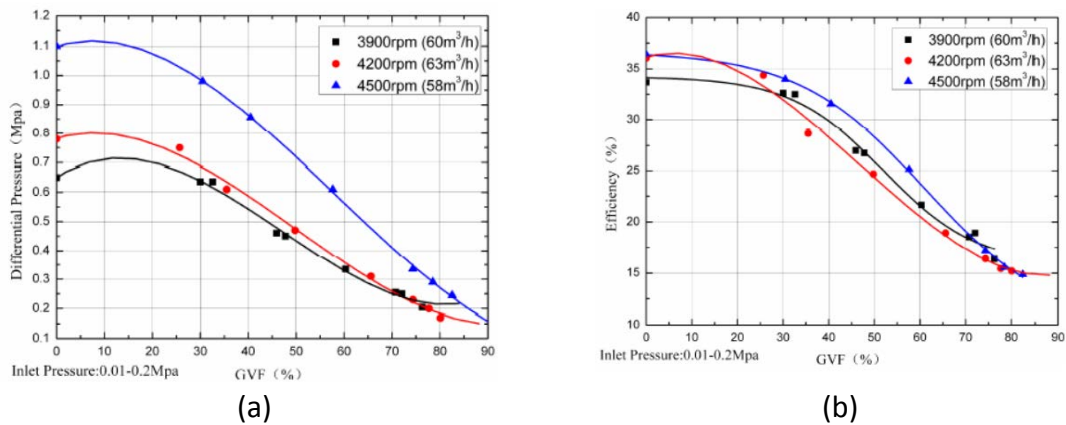


Figure 1-12: (a) Effect of Rotating Speed on GVF versus pressure rise (b) Effect of rotating speed on GVF versus efficiency (Zhang 2011)

Kirkland (2012) designed a test loop for evaluating the performance of an ESP in a vertical configuration using air and water as test fluids. The test loop can handle flow rates ranging from 10 kBPD to 60 kBPD and for different inlet pressures and rotating speeds. The author presented two phase performance results of a 3- stage mixed flow ESP. The ESP has a patented split vane impeller design which enhances the gas handling capability. Figure 1-13 shows the performance map of the pump for different liquid and gas flow rates. With the addition of gas there is a decrease in the pressure rise, with corresponding decrease in the power consumed by the pump. The efficiency of this pump is slightly lower than a mixed flow ESP having standard impellers and decreases with addition of gas. The BEP of the pump shifts to lower flow rates with addition of gas. Pirouzpanah (2014) performed detailed studies on the same pump using stage by stage pressure measurements, according to the author the head degradation of the pump increases with increase in GVF.

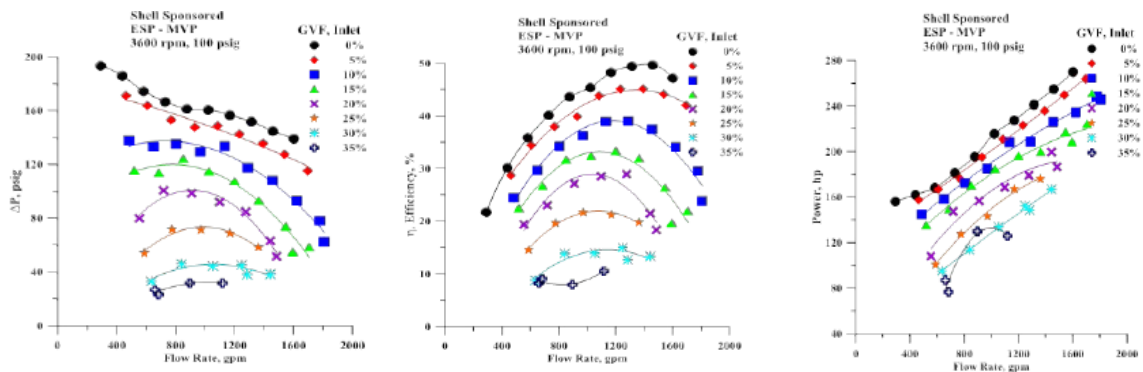


Figure 1-13: Performance of the pump for 100 psig Inlet pressure, 3600 RPM (Kirkland 2012)

1.1.2 Flow Visualization

Initial studies of two phase flow visualization were carried out by Murukami et al. (1974a) to determine the behavior of entrained air in the radial flow centrifugal pump. Experiments were performed in a semi-open impeller pump having a transparent casing. Flow of an air water mixture through the impeller was photographed using a strobe-light and high speed camera. The pump specifications are liquid only BEP at 8200 BPD and 1750 RPM. Figure 1-14 (a) shows the flow pattern of the mixture in the impeller nearing maximum air limit. From this figure it can be clearly observed that air accumulates on the pressure side of the impeller blade, any further increase in the air limit will cause gas-lock in the impeller. Figure 1-14(b) shows the variation of bubble diameter with impeller speed for a constant GVF, as the speed increases the bubble size becomes smaller due to chopping of the bubbles by the impeller blades.

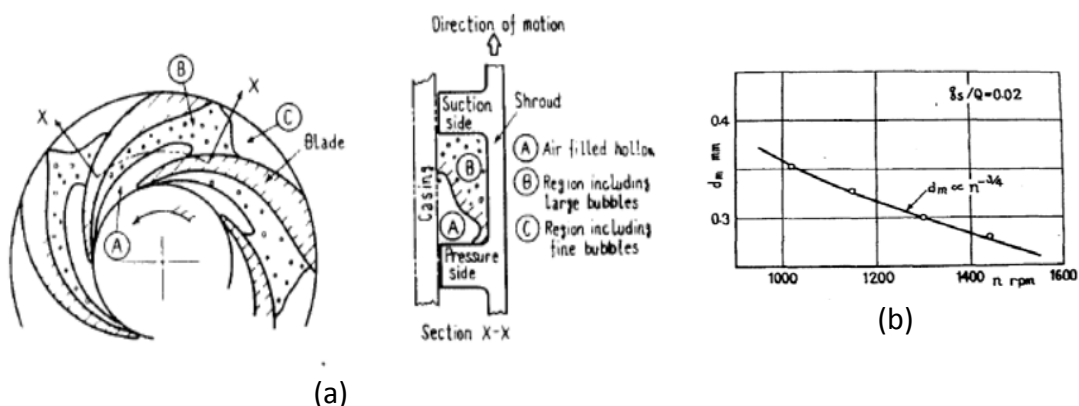


Figure 1-14: (a) Flow pattern in Impeller near the limit of pumping action (b) Effect of Pump speed on Bubble diameter(Murukami 1974a)

Murukami et al. (1974b) studied the effect of impeller blades on the flow pattern under two phase flow conditions. Under low GVF (<0.06) flow remained unaltered due to air addition. During high GVF conditions, changes in the flow pattern were clearly visible and were amplified with lesser number of impeller blades.

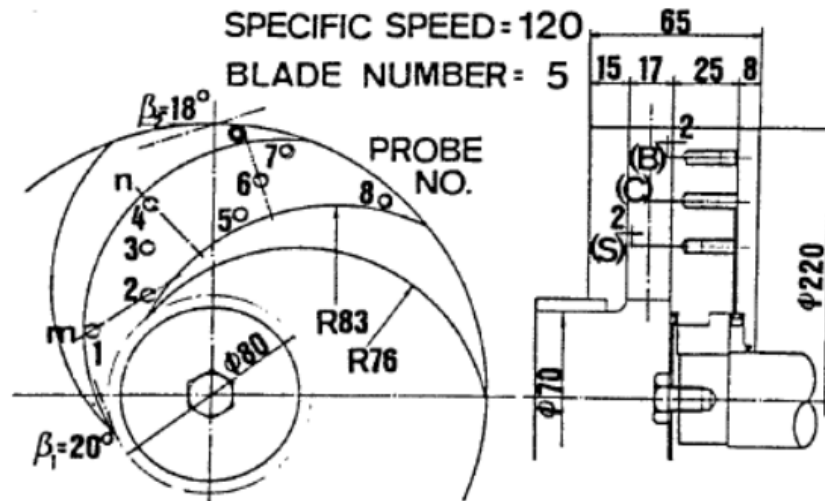


Figure 1-15: Location of electrical resistivity probes in the impeller (Sekoguchi 1984)

Sekoguchi et al. (1984) performed air-water performance study by using electrical resistivity probes in the closed radial flow impeller with liquid only BEP at 1750RPM and 3.6 kBPD. The pump was made of acrylic resin to observe the flow pattern visually. Electrical resistivity probes were used to measure local GVF distribution. Figure 1-15 shows the location of the electrical resistivity probes in the impeller. These probes can be moved axially to measure the variation of GVF from boss to shroud side.

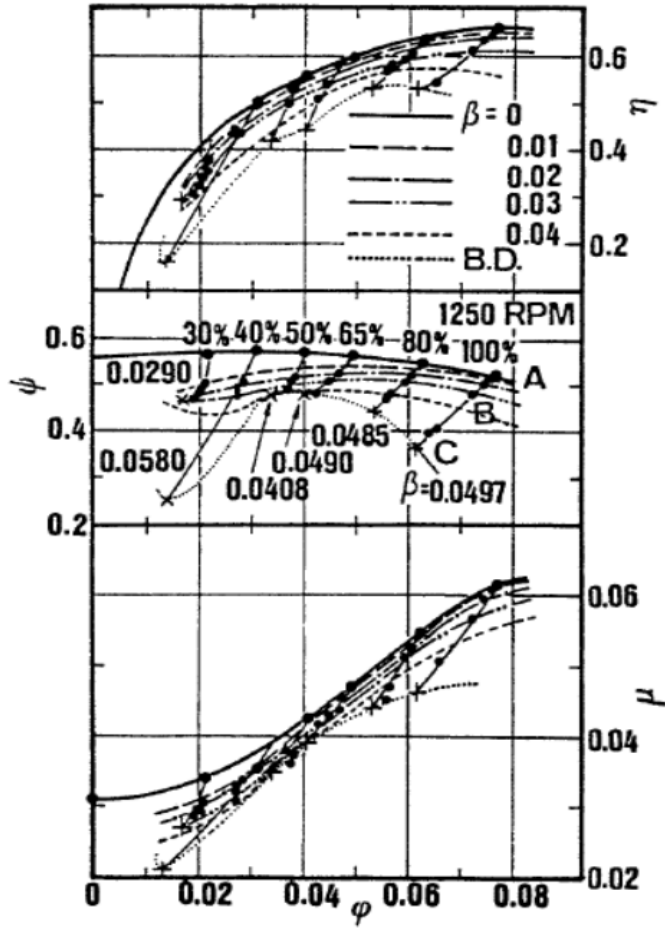


Figure 1-16: Pump performance map for different GVF (Sekoguchi 1984)

Figure 1-16 shows the performance map of the pump for different GVF as a function of flow rates. The graph shows that with an increase in the GVF, the head drops from A to C for a constant liquid flow rate beyond which the pump stops pumping. According to the author, the flow changes from Bubbly flow (A) to slug flow (B) with increase in GVF. At point B when the slug flow is reached the flow fluctuates considerably. With increase in the gas percentage beyond this point, the gas slug grows

until it reaches the impeller periphery, point C in the graph. Once the gas reaches the impeller periphery breakdown in pumping action occurs.

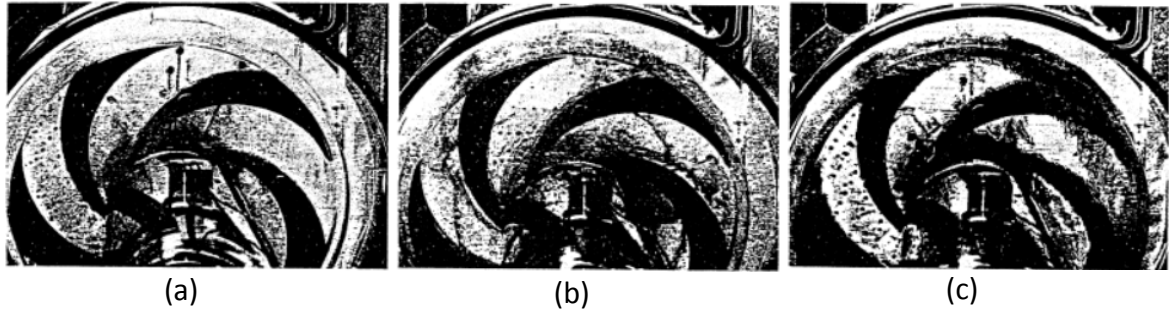


Figure 1-17: Flow Pattern in the Impeller for (a) $\beta=0.0116$ (b) $\beta=0.0497$ (c) $\beta=0.0497$ at Break Down (Sekoguchi 1984)

Figure 1-17 shows the flow pattern in the impeller for different GVF. From Figure 1-17(c) the impeller periphery is occupied by air near break down of pumping action. From the local GVF distribution, the slip ratio is evaluated and it decreases as the GVF increases. Figure 1-18 shows the variation of slip rate for different GVF and liquid flow rate. Near the breakdown of pumping action, slip ratio is close to zero.

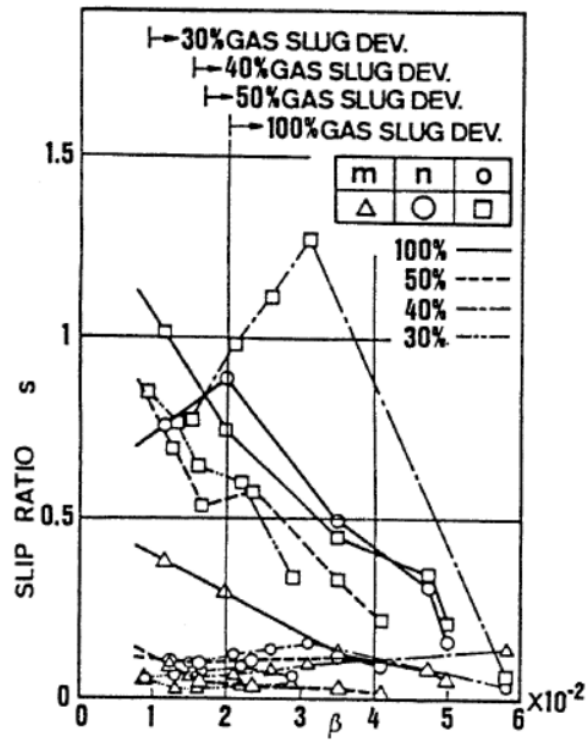


Figure 1-18: Slip ratio as a function of GVF for different liquid flow rates (Sekoguchi 1984)

Sato et al. (1996) performed a two phase performance study on a radial flow centrifugal pump using five kinds of closed impellers having different inlet and outlet blade angles. The flow behavior through the pump was visualized by using a transparent shroud casing in the pump. Pictures were recorded using a camera and stroboscopic light. From the pictures for the impeller with high incidence angle at low water flow rate flow pattern changes discontinuously from bubbly flow on the pressure side of the impeller blade flow to separated flow with an air cavity on the suction side of the blade. For flows having low incidence angles, an air cavity was observed on the pressure side of the impeller blade. Sudden head degradation was observed at lower

air flow rates as the blade outlet angle increases due to the formation of the air cavity. Any further increase in air flow rate beyond this does not cause sudden change in the head. With increase in incidence angle the head drop was discontinuous and no clear pattern is noticeable.

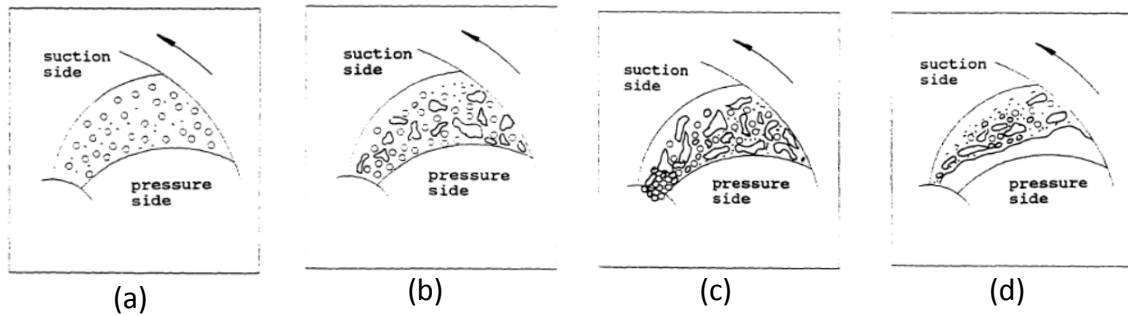


Figure 1-19: Different two phase flow regimes in impeller passages (Chisley 1997)

Chisley (1997) studied two phase flow performance in a centrifugal pump used in the nuclear industry. The study was carried out to simulate the performance of the pump under loss of coolant accident conditions. Pressure measurements and flow visualization were carried out using a partially shrouded, open and radial impeller. Visualization was carried out through one of the blade passages using stroboscopic light and high speed camera. Figure 1-19 shows the different flow regimes that occurred in the impeller blade passages as the GVF is varied. At low GVF bubbles start to accumulate on the pressure side of the impeller blade because of the adverse pressure gradient in the inlet of the impeller. With increase in GVF, the adverse pressure gradient extends towards the whole length of the impeller blade and hollow filled air space was formed from inlet to outlet as shown in Figure 1-19(d).

Poulikkas (2003) studied the effects of two phase liquid gas flow on the performance of nuclear reactor cooling pumps using flow visualization. High speed video camera was used to record the motion of bubble in the impeller flow passages. Under low GVF conditions gas bubbles had a tendency to concentrate on the impeller inlet closer to the suction side of the impeller blade as shown in Figure 1-20(a). As the GVF is increased the gas accumulation extends on the impeller blade as shown in Figure 1-20(b). With further increase in GVF, Figure 1-20(c) the blade passage became filled with gas which led to break down of the pumping action. For two phase flow conditions, flow separation regions existed in the impeller which caused the flow to deflect with increased relative velocity at the exit of the impeller. The change in the flow conditions at the outlet of the impeller reduced the impeller head considerably.

Estevam (2002) was the first to visualize two phase flow in a scaled ESP having radial impellers using water and air as test fluids. The pump was made of Plexiglas. Stroboscopic light and a high speed camera were used to observe the flow through the impeller. The experiments show that stationary gas bubbles were observed on the pressure side of the impeller blade and two different flow patterns were observed. Stratified flow, where gas bubbles are distributed uniformly through the whole flow domain and stationary bubbles, which occurs at the inlet of the impeller due to bubble coalescence. As the GVF was increased, the stationary bubble at the impeller inlet increased in size and tended to occupy the flow path. When the gas bubble occupied a major part of the flow path surging was observed during which a sudden drop in the pump head was also observed. With

increase in pump speed the ability of the pump to handle high GVF was increased before surging occurred.

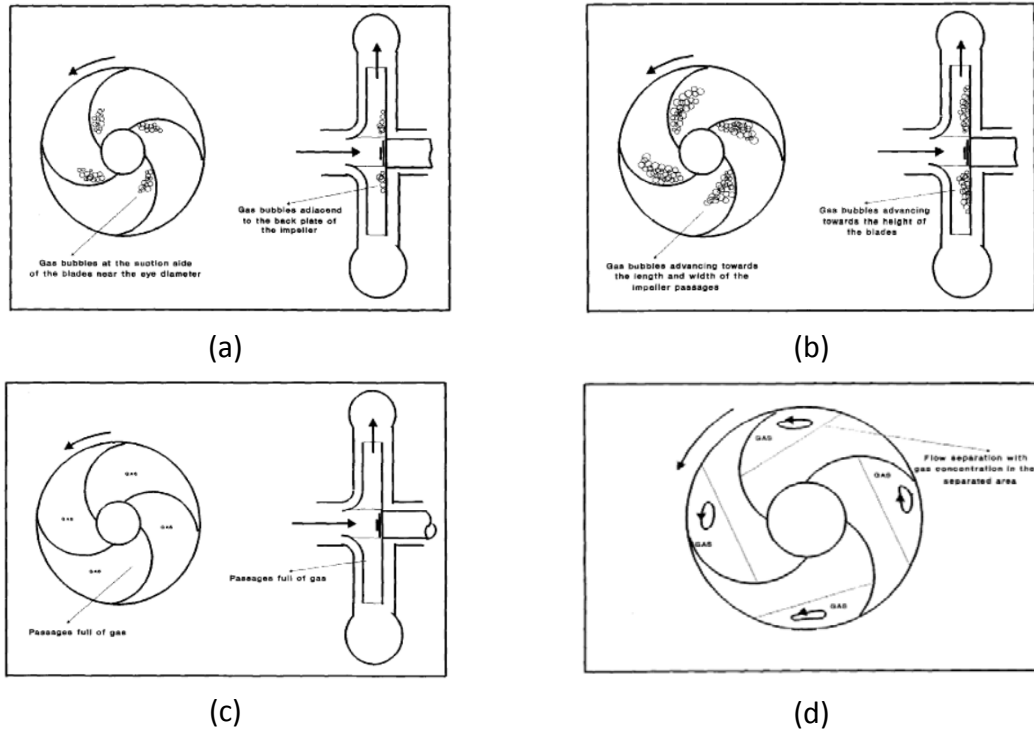


Figure 1-20: Gas accumulation in the impeller (a) Low gas content (b) Medium gas content (c) High gas content (d) Flow separation (Poullikkas 2003)

Barrios (2007) observed two phase flow visualization inside a two stage ESP having radial impellers. The second stage impeller and diffuser were modified to observe the flow from the top of the pump, where the pump was mounted vertically. On the top of the pump, a plexi glass window was used for sealing the pump and to visualize the flow as shown in Figure 1-21.



Figure 1-21: Two stage ESP setup (Barrios 2007)

Experiments were carried out to observe different flow regimes and to measure the bubble diameter using stroboscopic light and a high speed camera. The maximum limits for the operating conditions were 480 BPD liquid flow rate, 2% GVF and 1500 RPM. Gas bubbles were observed to be closer to the pressure side of the impeller blade for different flow conditions as shown in Figure 1-22(a). As the two phase flow head drops by 50% in comparison with pure liquid data, the stationary gas bubble occupied close to 75% of the impeller flow area as shown in Figure 1-22(b).

The bubbles have the shape of a prolate spheroid and are not spherical. Figure 1-23 shows the variation of bubble diameter for different operating conditions at the onset of surging for different liquid flow rates.

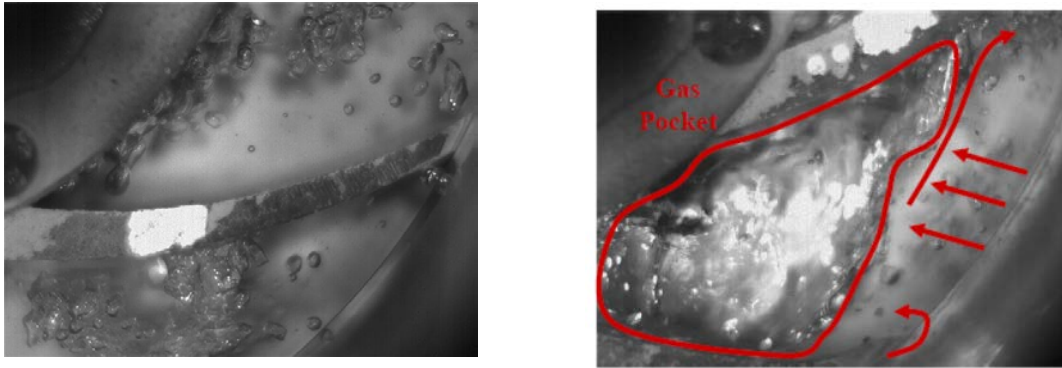


Figure 1-22: (a) Two phase flow through Impeller for 250 BPD liquid flow rate (b) Gas Pocket Formation in impeller at 175 BPD liquid flow rate for 600RPM, and 0.15 scf/hr gas flow rate (Barrios 2007)

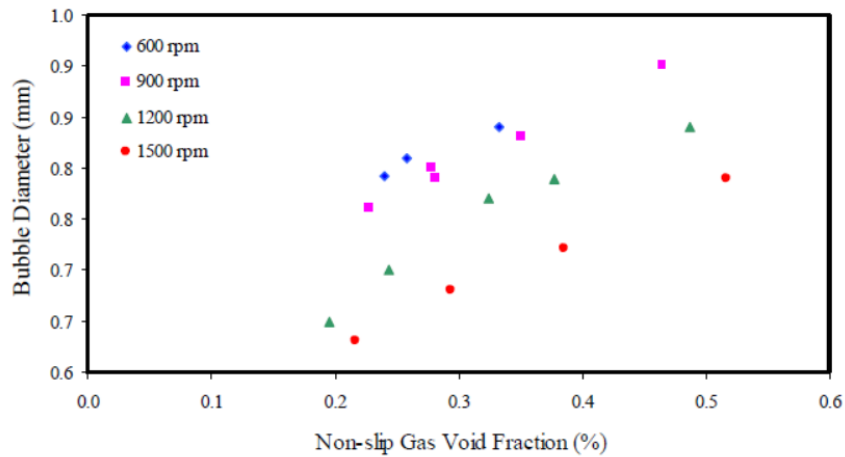


Figure 1-23: Variation of bubble diameter for different operating conditions at the onset of surging (Barrios 2007)

Gamboa (2009) extended the work of Barrios (2007) by modifying the experimental setup as shown in Figure 1-24. A transparent acrylic casing was used for the second stage along with an acrylic tube before the 2nd stage impeller to visualize the flow using a high speed CCD camera. Air, water, Sulphur hexafluoride (SF₆) and isopropanol were used as test fluids to study the effect of density and surface tension. SF₆ was used to study the effects of density, the density is lower in comparison to air.

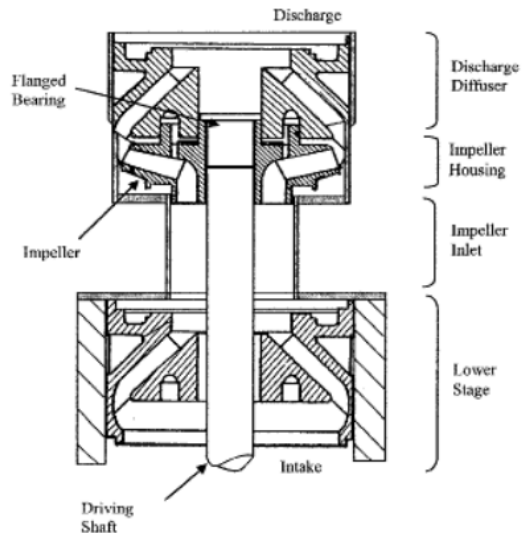


Figure 1-24: Schematic view of the ESP pump (Gamboa 2009)

Figure 1-25(a) shows the effect of gas density on pressure rise for different GVF, with increase in gas density the pressure rise was higher and surging shifted to higher GVF. Figure 1-25(b) shows the effect of gas, surface tension on pressure rise for different GVF.

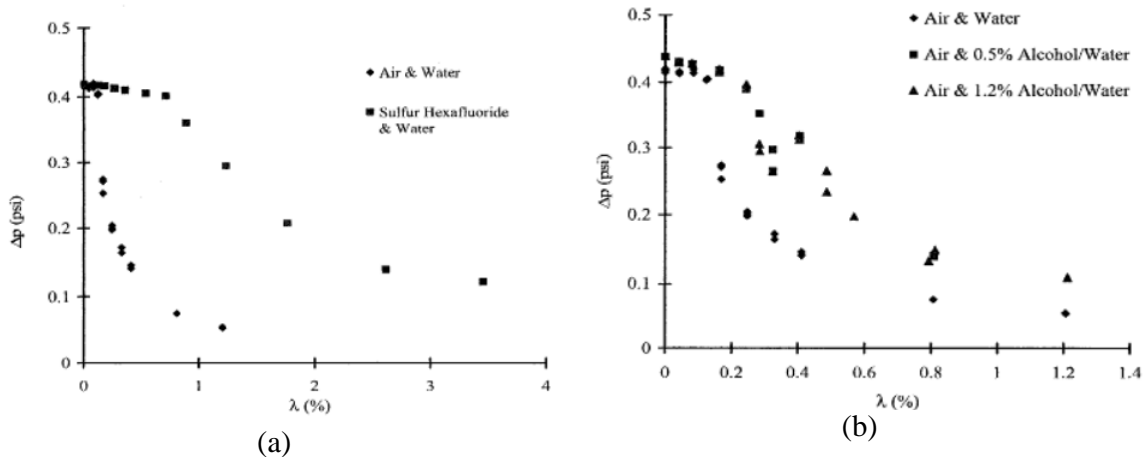


Figure 1-25: (a) Effect of gas density on pressure rise (b) Effect of surface tension on pressure rise at 2 psig, 600 rpm, $q_{ld} = 0.6$ (Gamboa 2009)

Surface tension of the liquid reduced as alcohol percentage increases. With a decrease in surface tension the onset of surging shifted to higher GVF and there was no significant change in the pressure rise.

According to the author, the flow patterns within the impeller were divided to four regimes for the performance map shown in Figure 1-26. Point (1) corresponds to Regime 1 where the bubbles are isolated and there is no significant change in the head in comparison with pure liquid. Point 2, Regime 2 corresponds to bubbly flow where the numbers of bubbles increases and interaction among bubbles is also observed. Point 3 and 4 is Regime 3 during which surging occurs and gas pockets are formed, where without a change in the GVF the head drops within a few minutes, corresponding to unstable operation of the pump. With further increase in GVF beyond Point 4, Regime 4 is observed during which gas pockets occupy the whole length of the impeller flow area.

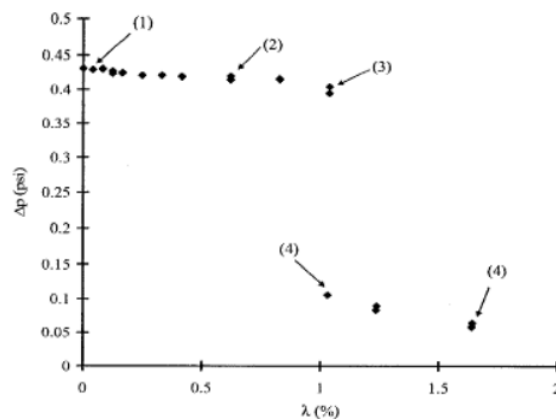


Fig. 4.19 Impeller Flow Patterns

Figure 1-26: Impeller flow patterns for 2 psig, 600 rpm and $q_{l,d} = 0.6$ (Gamboa 2009)

Trevisan (2009) extended the visualization work of Gamboa (2009) by modifying the set up for handling high viscosity fluids. Experiments were carried out using air, water, and oil to observe the effect of viscosity of fluid on performance and flow pattern. According to the author, four regimes were observed for two phase flow through the pump namely bubbly flow, agglomerated bubbles, gas pocket, and segregated gas. Bubbly flow was observed during low GVF and is independent of liquid flow rate and rotational speed. Agglomerated bubble pattern was observed when there was an increased bubble concentration on the pressure side of the impeller blade which led to bubble coalescence and small gas pocket formation. Gas pockets were formed with increasing the GVF from the agglomerated bubble where a significant portion of the impeller flow path was occupied by stationary gas bubble, restricting the liquid flow. Segregated bubble regime was observed by further increasing the GVF to where the stationary gas bubble extended to the impeller outlet. The gas liquid interface is unstable leading to bubble breakup at the stationary end trailing edge. The regimes were the same even while using oil as test fluid but the bubbly flow regime was difficult to observe even at low liquid flow rates.

The bubbles have the shape of a prolate spheroid and are not spherical. Figure 1-23 shows the variation of bubble diameter for different operating conditions at the onset of surging for different liquid flow rates.

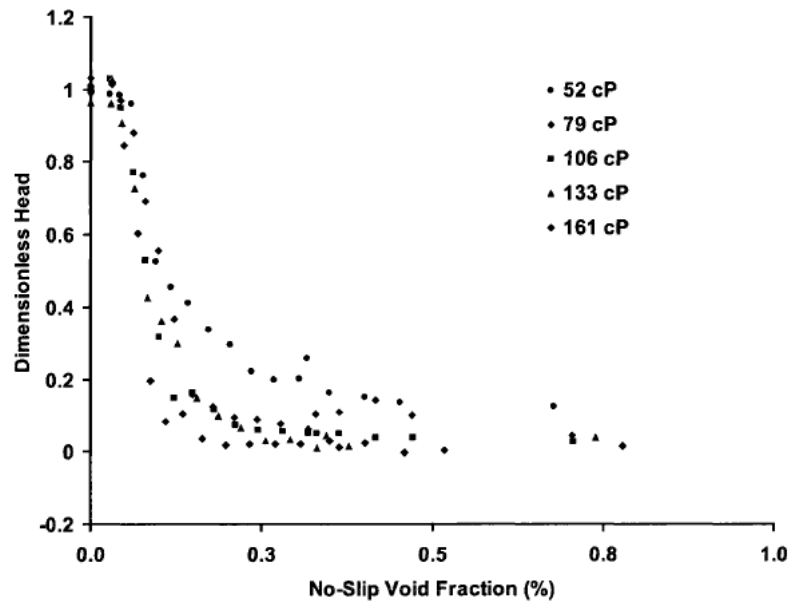


Figure 1-27: Performance map using oil and air for different viscosities at 15 Hz (Trevisan 2009)

Marchetti (2013) performed two phase flow visualization studies on a single stage, full scale transparent mixed flow ESP which are used in petroleum industry. The ESP that was tested had a split vane in the impeller, which had the ability to handle high gas content flows by providing better mixing between phases. Flow visualization was performed for water flow rates ranging from 8 kBPD to 17 kBPD with a maximum GVF of 2% for 1800 RPM using a high speed camera. According to the author, recirculation zones were observed closer to the suction side of the blade, obstructing 75% flow path area in the diffuser outlet.

1.1.3 CFD Simulation

Lakshminarayana (1991) reviewed various CFD techniques that are used for the design and analysis of turbo machinery. The review includes accuracy, efficiency,

approximations, limitations of methods, and turbulence models. Suggestions were made with regard to the applicability of methods for various flow regimes, compressible and incompressible flows, two phase flows and cascades. According to the author, Navier-Stokes equations can be commonly used for design and analysis with integration of physical models and computational techniques. At the end the author made suggestions for future research such as grid generation techniques for complex 3D flows, improved turbulence and transition models, acceleration schemes and techniques of two phase flow.

Croba et al. (1996) developed a 2-D numerical model for calculating flow through a centrifugal pump having a rotating impeller and a stationary volute. 2-D Reynolds-averaged Navier Stokes equations along with a continuity equation and $k-\epsilon$ equations were used for solving unsteady, incompressible, and turbulent flow in the pump. At the interface between the rotating impeller and stationary volute, a multi-domain overlapping grid technique was used to solve the flow field. The equations were discretized using finite volume method in space and implicit scheme for time. The flow field calculation was used to develop pump modifications, reduce vibrations, hydraulic noise, and radial forces within the pump. The simulated results were validated for a centrifugal pump having a specific speed of 32. However the model cannot accurately predict the flow field near the volute tongue.

Majidi et al. (2000) performed 3-D CFD simulations using a commercial code to determine secondary flows in a centrifugal pump having volute and circular casings.

The commercial code used equations of continuity and RANS to solve for incompressible turbulent flow with turbulent viscosity modeled using two equation model (k-ε). The interface between the stator and rotor was modeled using a sliding interface. Figure 1-28 shows the pressure distribution for both the volute and circular casing at mid span.

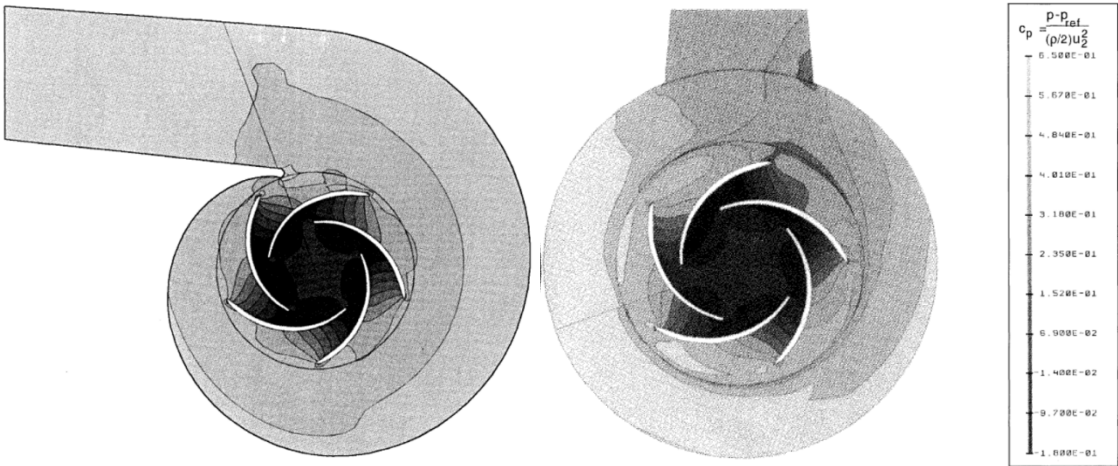


Figure 1-28: Pressure distribution on the pump with volute and circular casing at mid span (Majidi 2000)

Figure 1-29 shows the velocity vectors at different cross sections of the volute, where the presence of secondary flows is clearly noticeable.

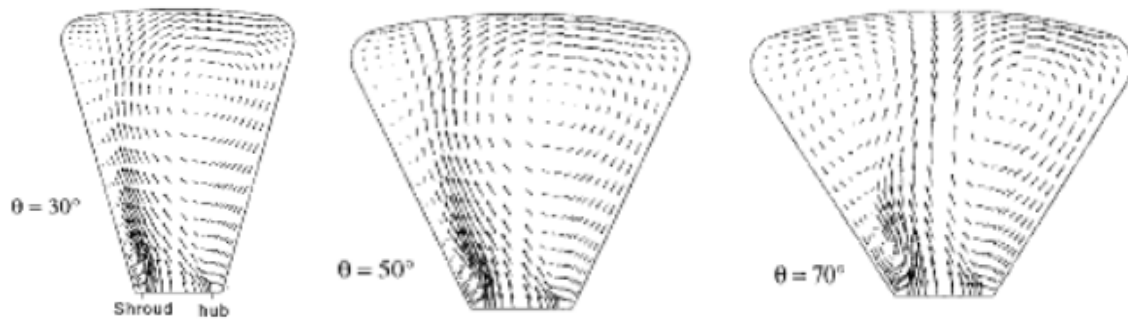


Figure 1-29: Velocity vector at different cross sections of the volute (Majidi 2000)

Gonzalez et al. (2002) carried out 3-D unsteady CFD simulations in a centrifugal pump to determine the dynamic effects of impeller volute interactions using commercial codes. 3-D Navier Stokes equation coupled with $k-\epsilon$ equations were used to model the turbulent flow. SIMPLEC algorithm was used for pressure velocity coupling. Convective terms were discretized using second order up wind schemes and diffusion terms were discretized using central difference schemes. Total pressure at the inlet and static pressure at the outlet were used as boundary conditions. These boundary conditions were used to determine the unsteady pressure and velocity fluctuations at the boundary. The simulated results agree well with experimental predictions and the pressure fluctuations at the interface of impeller outlet and volute tongue reveal blade passing frequency. Majidi (2005) performed the same type of calculations in a different pump to determine the unsteady blade loading in the impeller. The equations and boundary conditions are similar to Gonzalez (2002).

Schilling et al. (2002) performed two phase flow simulations in a centrifugal pump impeller for gas-liquid mixture by using a simple approach i.e. solving equations

for only one phase. The liquid phase was solved using continuity and momentum equations and density in the liquid phase was treated as density of mixture. A source term was added in the momentum equation to account for the forces between liquid and gas phases. The velocity of the gas phase was calculated analytically. Using this approach less computational effort is needed. The results agree well with the experimental data for GVF less than 5% for a centrifugal pump impeller having specific speed of 27. For higher percentages of air there was a sudden drop in performance, which cannot be simulated using a one equation model since the flow behavior is different. For higher percentages of air, separate equations should be solved for each phase.

Medvitz et al. (2002) performed 3-D multiphase simulations on a centrifugal pump to predict the performance under developed cavitating conditions for different flow conditions and cavitation numbers. Apart from the continuity and momentum equations for each phase, extra equations were needed for generation and destruction of the volume fraction of the liquid since the collapse of a gas cavity is modeled as phase transformation. The $k-\epsilon$ equations are used to model turbulent viscosity. Steady state simulations were carried out for most cases except for low flow coefficient and low cavitation numbers where unsteady simulations were performed. The authors successfully validated the simulated results with experimental measurements

Caridad et al. (2002) performed two phase simulations in an ESP impeller to predict the performance and flow field inside the pump using a commercial code. A

multi fluid approach was used to solve continuity and momentum equations for each phase coupled with the equation of state. The k- ϵ equations were used to account for closure of the turbulent viscosity. Total pressure was specified at the inlet of the impeller and mass flow rate at the outlet of the impeller as boundary conditions with relative velocity on the impeller blades and wall set to zero, bubble size was assumed to be 0.5 mm. Simulations were carried out to predict the radial impeller performance for a maximum flow rate of 3000 BPD and maximum GVF of 17%. Figure 1-30 shows the liquid concentration in the impeller for different flow conditions. The gas bubbles tend to be closer to the pressure side. The simulation results over predict the head developed within the impeller and it increases as GVF increases.

Tremante (2002) carried out 2-D simulations on an axial pump impeller to predict the two phase flow performance and to study the effect of GVF on lift and drag coefficients using a commercial code. A multi fluid model was used to solve the flow field using an Inter-Phase slip algorithm. The simulated results do not quite match with experimental performance measurements because of the 3D nature of the flow.

Caridad et al. (2004) performed 3D CFD simulations for a radial ESP impeller handling two phase flows to predict the performance and flow characteristics. Simulations were carried out using two fluid models with a mixture k- ϵ model for turbulent closure. The equations were solved using a commercial code with total pressure inlet and mass flow outlet as boundary conditions.

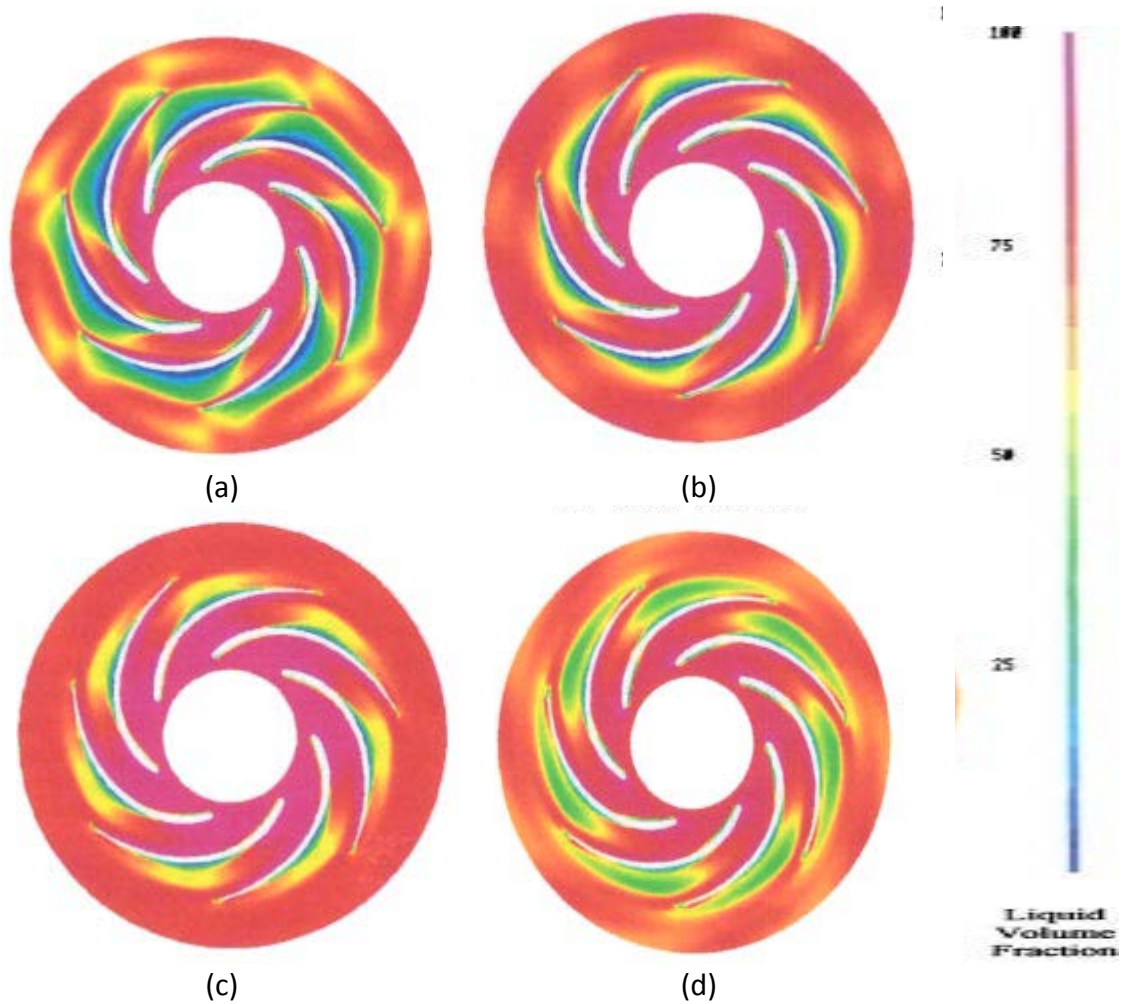


Figure 1-30: Liquid phase distribution in the impeller for (a) 1300 BPD, 10%GVF (b)2100 BPD, 10%GVF (c)1700 BPD, 10%GVF (d)2100 BPD, 17%GVF (Caridad 2002)

The author was able to predict the formation of gas pocket on the pressure side of the impeller blade, which was the main reason for head deterioration in the impeller when handling two phase flows. The effect of varying bubble size on performance was also studied. Figure 1-31 shows the comparison between experimental and simulated impeller performance. Simulations over predict the head developed by the impeller by 20 to 50 % because the impeller diffuser blade interaction was not simulated.

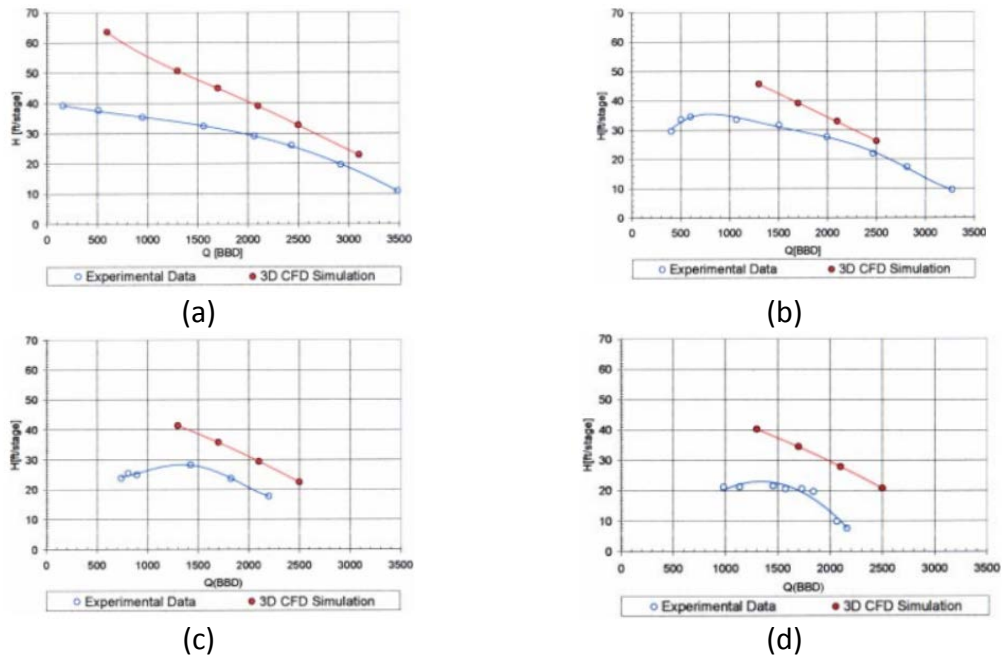


Figure 1-31: Pump performance for (a) Single phase flow (b) 10% GVF, bubble diameter = 0.1 mm (c) 15% GVF, bubble diameter = 0.1 mm (d) 17% GVF, bubble diameter = 0.1 mm (Caridad et al. 2004)

Gonzalez et al. (2006) extended his previous work on 3D CFD simulations in a centrifugal pump to correlate the effect of flow field on the torque of the impeller blades and secondary flow in the volute. The unsteady pressure distribution on the blade at different blade position appears to be the major factor affecting the variation of torque on the impeller blades. Helicity, which is a direct measure of secondary flow, was correlated to the pressure fluctuations on the impeller blade at the blade passing frequency for different impeller positions.

Barrios (2007) performed single phase and two phase simulations on a mixed flow impeller of an ESP to predict the performance and flow field. Single phase simulations were carried out using RANS equations and $k-\epsilon$ turbulence model using total pressure at inlet and mass flow at outlet of impeller as boundary conditions. The

simulated results agree well with the experimental data. Two phase simulations were performed using an Eulerian- Eulerian model with inter phase terms modeled using a particle model. The author used the experimental bubble diameter and the drag coefficient as inputs for the simulations. Simulations were able to predict the presence of gas accumulation at the inlet of the impeller as shown in Figure 1-32. The flow field from the simulation was compared with the experimental visualization data.

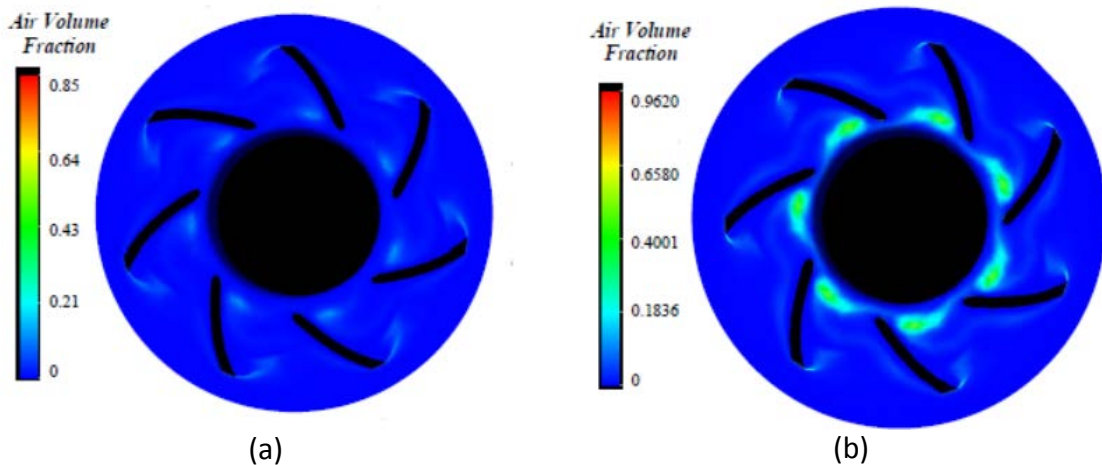


Figure 1-32: Air volume fraction for 500 BPD, 1500 RPM at (a) 0.05% GVF (b) 0.1% GVF (Barrios 2007)

Marsis (2012) performed unsteady single and two phase simulations of an MVP ESP which has been designed for handling high GVF flows. The RANS equations coupled with k- ϵ model were used to predict the single phase performance. Mass flow at the impeller inlet and pressure at diffuser outlet were used as boundary conditions. Transient analysis was carried out using moving mesh between the impeller and diffuser. The simulated results agree well with the experimental data. Two phase simulations were carried out using an Eulerian- Eulerian model, which has a separate

set of equations for each phase. A Reliable k- ϵ model was used to model turbulent viscosity. The Ideal gas law was used to obtain the density of air. Simulated results show that a single stage pump homogenizes the flow as shown in Figure 1-33.

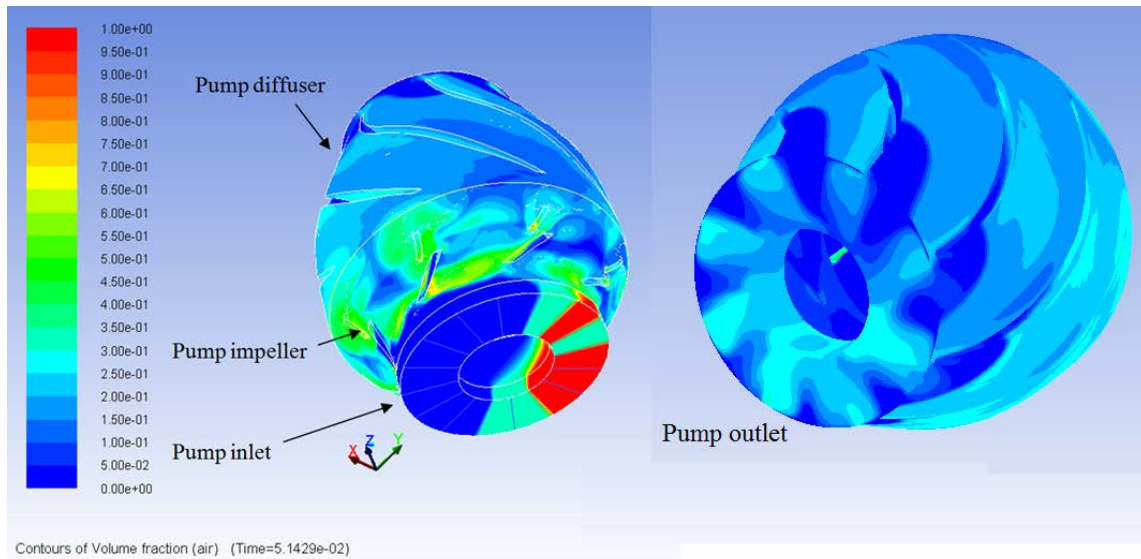
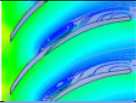
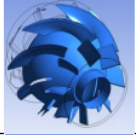
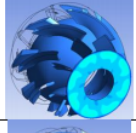



Figure 1-33: Air volume fraction for 25 kBPD flow rate and 25% GVF (Marsis 2013)

Marsis et al. (2013) carried out a CFD based design modification for an ESP pump by performing CFD simulations for different diffuser configurations. Single phase CFD results were presented for different diffuser designs and their effect on the pressure rise in the diffuser is shown in Figure 1-34. According to the author, a 4% pressure rise was obtained by modifying the diffuser design for single phase flow with a corresponding increase of 23% for two phase flows.

Design no.	Description	Increase in pump static pressure
Design 1		1%
Design 2		-4%
Design 3		-8%
Design 4		+1.5%

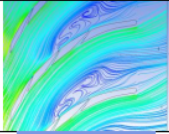
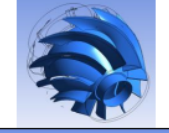
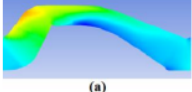
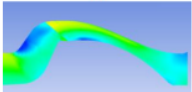
Design 5		+3.2%
Design 6		+3.2%
Design 7	 	+2.2%
Design 8	Design 5+Design 6+Design 7	+4%

Figure 1-34: Different diffuser design with corresponding pressure rise (Marsis et al. 2013)

2 OBJECTIVES

Much of the literature on experimental studies, flow visualization, and CFD simulations for pumps under multi-phase flow conditions was related to the nuclear power industry where the conditions are different from the Petroleum Industry. Nevertheless, in the last two decades considerable work has been carried out on ESP's and Advanced gas handlers with limited applicability to the exact operating conditions as seen in the field. Furthermore, experimental studies carried out on Advanced Gas handlers (Poseidon Pump) are for multi stage pumps with no information on individual stage impeller and diffuser performance. Multi-phase CFD simulations on the Poseidon pump presented in the literature deviate to a great extent from actual measurements.

In the current study, a Poseidon pump that follows the design of a 4-stage advanced gas handler is tested for different operating conditions. The pump is instrumented to obtain each stage impeller and diffuser performance along with vibration monitoring of the pump. Stage by stage performance measurements are used to study the head degradation of the pump under two phase flow conditions for different stages.

To better understand the two phase flow behavior inside of the Poseidon pump, a full scale single stage Poseidon pump was designed and manufactured using clear material. Flow visualization is carried out using a high speed camera to obtain the two phase flow pattern and bubble size distributions for different operating conditions.

Bubble size measurements are an important input for performing multi-phase CFD simulations.

To obtain a complete study on flow through the pump and to find the parameters effecting pressure rise and efficiency, single and two phase 3-D transient simulations are carried out on two stages of the 4-stage pump using the commercial software ANSYS-Fluent. The CFD model is validated using experimental data for different operating conditions. The validated model is then used to study the head degradation caused by the pump under two phase flow conditions at higher GVF.

3 METHODOLOGY

3.1 Experimental Set up

In this sub section experimental set up of the 4-stage pump for performance measurement and single stage pump for flow visualization is discussed.

3.1.1 Test Rig

Figure 3-1 shows the P&ID diagram of the experimental setup that was used for testing the 4-stage pump and single stage clear pump. The experimental facility is located at the Turbo machinery Laboratory, Texas A&M University. The closed loop test facility setup consists of a 1500 gallon stainless steel tank/separator which has a maximum pressure limit of 450 psig as shown in Figure 3-29(a). Three major pipe lines are connected to this tank, water line, air line and mixture line. Water is supplied to the pump using a water line which has a 6 inch diameter pipe connected to the bottom of the tank. Air is supplied to the pump using a 3 inch pipe connected to the top of the tank.

Flow from the outlet of the pump is directed back in to the tank using a 6 inch diameter outlet line. The air and water line flow rates are controlled using electro-pneumatic fisher valves as shown in Figure 3-29(b). In the outlet line, the back pressure is controlled using an electro-pneumatic fisher valve.

After the electro pneumatic valves, tee's are placed on all of the three major lines as shown in Figure 3-29(c) with butterfly valves on both sides of the tee. One side

of the tee is used for connecting pipe lines to the 4-Stage pump. The other side of Tee is used for connecting pipe lines to the single stage clear pump. Both the pumps cannot be run simultaneously.

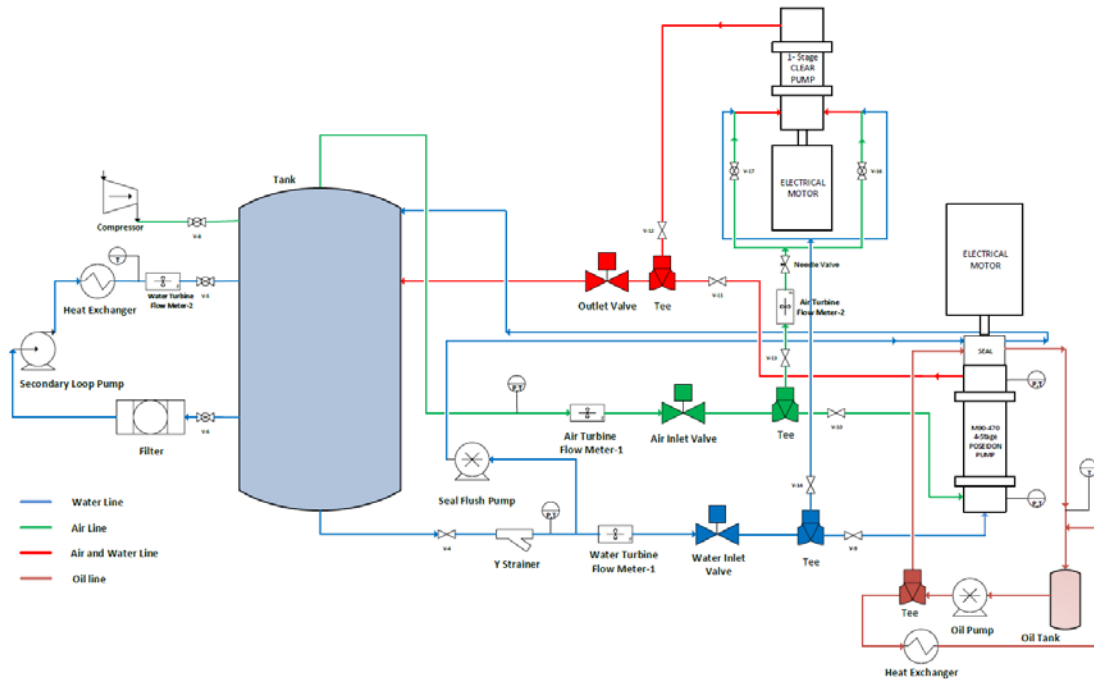


Figure 3-1: P&ID diagram of the Experimental Setup

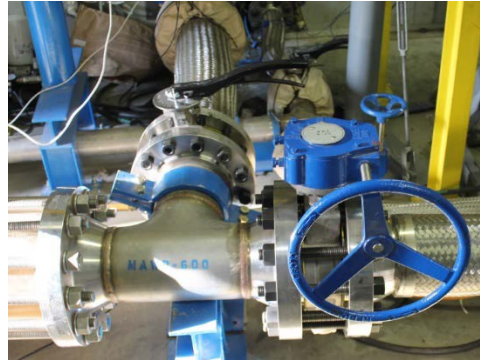
For the 4-Stage pump auxiliary equipment is required, which consist of a face seal and a thrust bearing. For the face seal a water flush is required. A reciprocating pump is used to supply water to the seal as shown in Figure 3-3(a). The thrust bearing counteracts the total axial thrust of the pump since there is no hydraulic balancing of forces of the forces on the impeller. Oil is supplied to the thrust bearing to remove the heat and to lubricate them. A small water cooled heat exchanger is used to remove heat from the oil. Figure 3-3(b) shows the oil pump, tank and heat exchanger.



(a)



(b)



(c)

Figure 3-2: a. Picture of Stainless Steel Tank b. Picture of Fischer valve c. Picture of Tee's



(a)



(b)

Figure 3-3: a. Reciprocating Pump b. Oil Pump and Heat Exchanger

Transparent windows are placed in the air and water line as shown in Figure 3-4. In the water line the purpose is to visually inspect the presence of air flow at high liquid flow rates. In the air line a window is used to detect the presence of water in the flow caused by back flow from the inlet at low air flow rates.

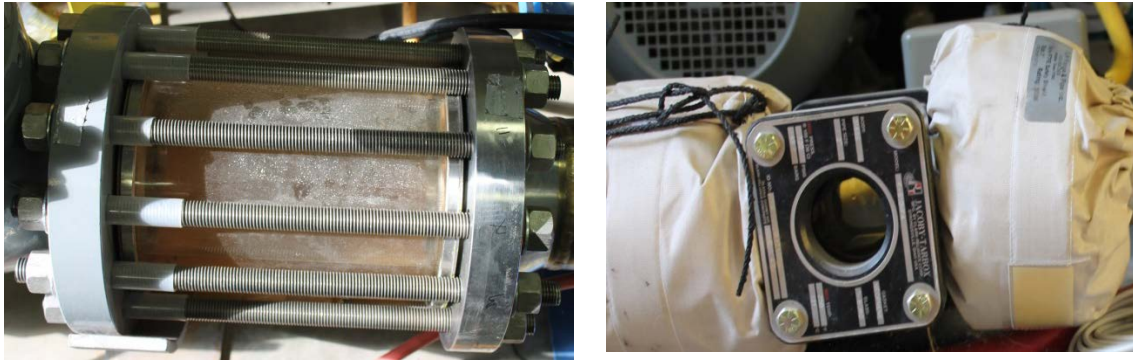


Figure 3-4: Transparent Window in a. Water Line b. Air Line

A 250 hp AC Electrical motor is used for performing tests on the 4-Stage pump. The motor is controlled using a Variable Frequency Drive (VFD) with the maximum frequency limited to 60 Hz (3600 RPM). Similarly for the single stage clear pump, a 100 hp AC Electrical motor was used. It was controlled using a VFD with a maximum frequency of 60 Hz.



Figure 3-5: Secondary Loop with Pump, filter and Heat exchanger

The materials of the transparent windows in the pipes limit the maximum working temperature range to 110 F. This limitation required a secondary loop to be connected to the tank which has a centrifugal pump, filter and heat exchanger to maintain the water in the desired temperature range. A picture of this system is shown in Figure 3-5 .

The 4-Stage pump that was tested is a helicon-axial Pump which is also known as the Poseidon pump manufactured by Schlumberger. The pump stages are exactly the same as the pump that would be used in oil wells for pumping crude oil. There are three blades on the impeller that follow the profile of an Archimedes screw as shown in Figure 3-6. The diffuser has nine blades with minimal change in the blade angle from inlet to outlet in comparison with the mixed flow pump diffuser as shown in Figure 3-7. Both the impeller and diffuser are manufactured using Ni-Resist Cast Iron. Since the impeller blades are unshrouded, a casing is provided on the impeller with a radial tip clearance of 20 mils.

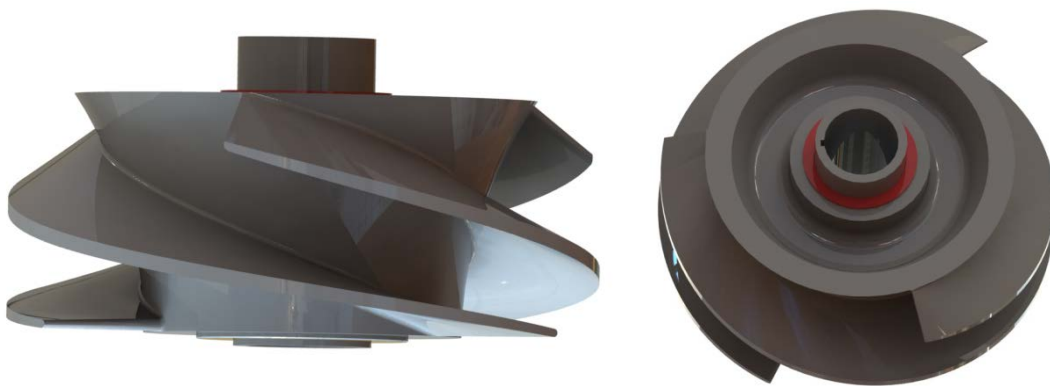


Figure 3-6: 3-D model of Impeller, Different Views

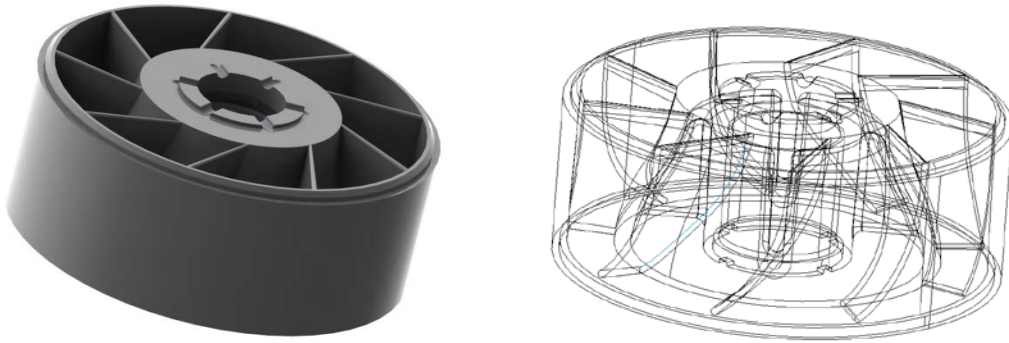


Figure 3-7: 3-D model of Diffuser

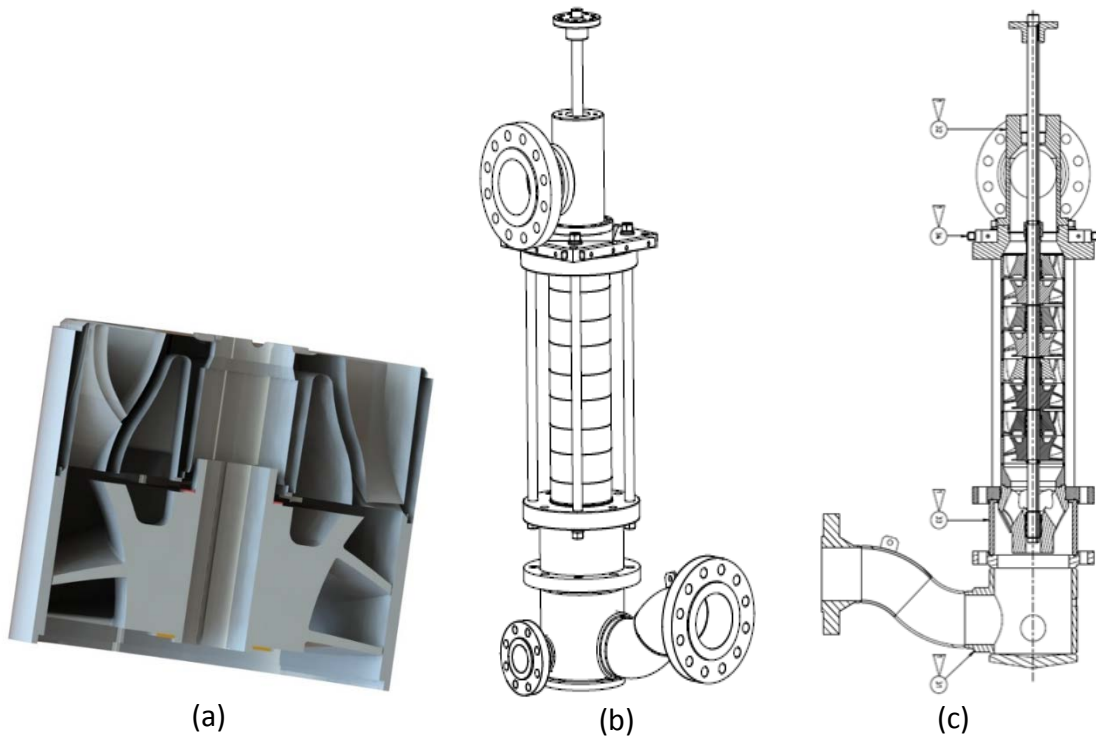


Figure 3-8: a. Single Stage pump b. 4-Stage Pump Assembly c. Cross Sectional View of 4-Stage Pump

Figure 3-8(a) shows the cross sectional view of the single stage pump. Figure 3-8(b) shows the 3-D model of the pump assembly with the inlet mixture body and outlet. The inlet mixer body has two inlets, one for air and another for water. The cross

sectional view is shown in Figure 3-8(c).The pump assembly was assembled in to the test rig as shown in Figure 3-9.



Figure 3-9: Test rig Picture with pump

Based on the 3-D models of the impeller and the diffuser, a transparent stage of the pump was designed and manufactured so that the flow path matched the Poseidon pump. The impeller and diffuser were manufactured using “Somos water clear XC 10122” material by using Stereolithography (SLA) process, which is essentially a 3-D printing technology. Since the impeller and diffuser are made of plastic type material, the blades had to be thickened so that the stresses are within the acceptable limit and deflection is minimized. The thickness of the impeller blades had been increased by 50%, the diffuser blades by 10% in comparison with actual pump. The pictures of the

actual impeller and diffuser parts are shown in Figure 3-10 and Figure 3-11. The impeller and diffuser are enclosed in a casing (or Pump Body) which was designed for a MWP of 400 psig and manufactured using polycarbonate.

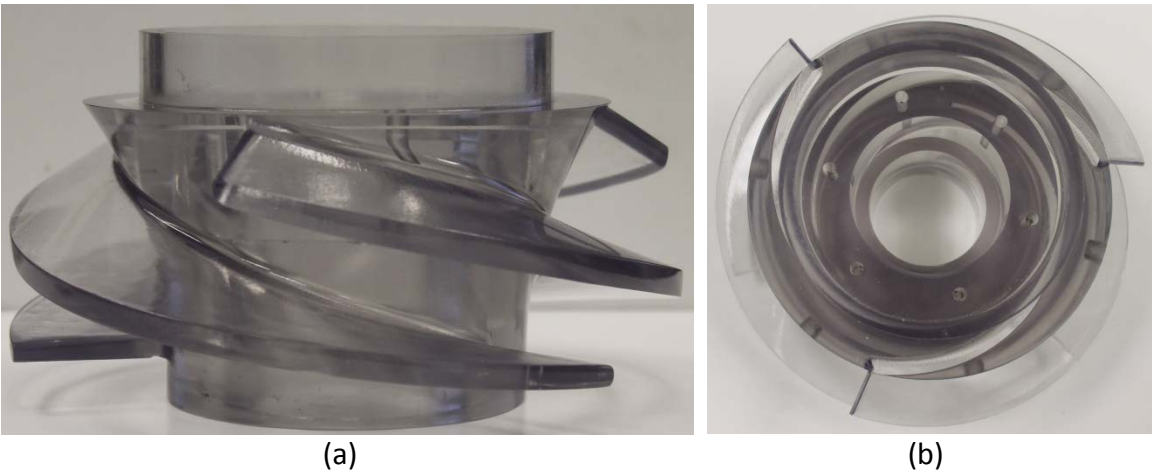


Figure 3-10: Picture of Clear Pump Impeller a. Front View B. Top View

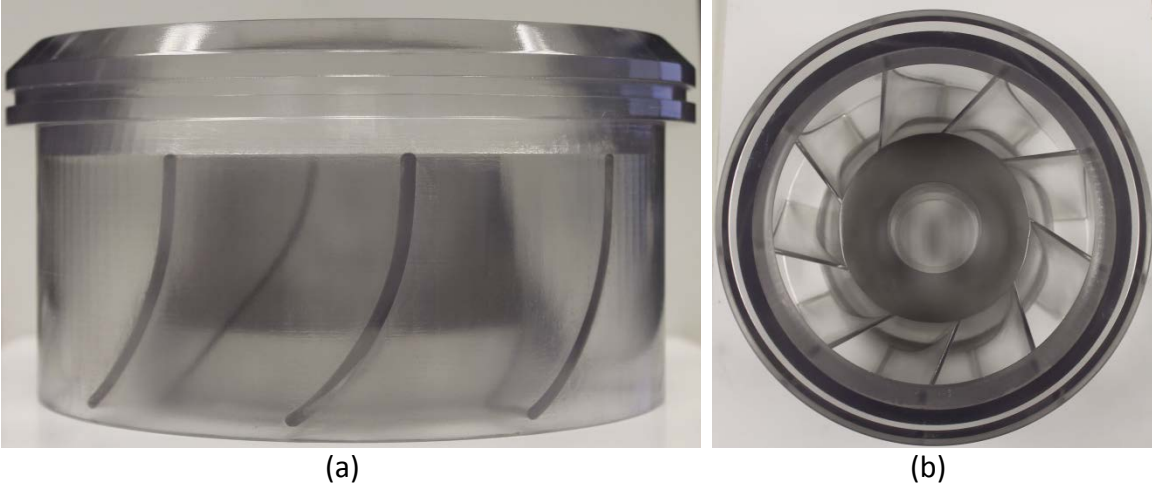


Figure 3-11: Picture of Clear Pump Diffuser a. Front View B. Top View

Figure 3-12(a) shows the impeller and diffuser assembled inside the pump body. Figure 3-12(b) shows the picture of the clear pump test rig. The electric motor is at the

bottom, flow inlet to the pump occurs from both sides of the pump and single outlet at the top of the pump.

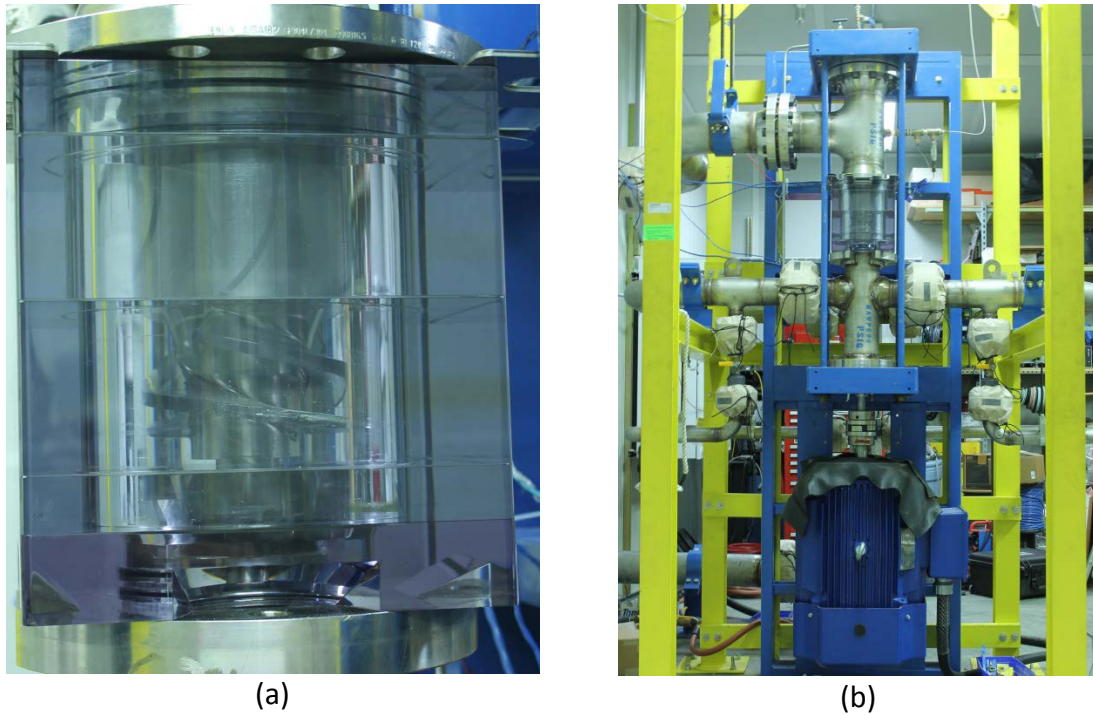


Figure 3-12: Picture of Clear Pump a. Impeller-Diffuser with Casing b. Test rig

3.1.2 Instrumentation

For measuring flow rate of the water and air, four turbine flow meters were used. One turbine flow meter was used for measuring the flow rate of water supplied to the pump. It was assembled on the water line as shown in Figure 3-1. Two air turbine flow meters were used for measuring flow rate of air, for different ranges. One flow meter was used for measuring the flow rate of air supplied to the 4- stage pump and another one of lower capacity was used for measuring flow rate of air supplied to the

clear pump as shown in Figure 3-1. For the secondary flow loop, one turbine flow meter was used to make sure that enough water was supplied through the heat exchanger. Table 3-1 shows the list of different flow meters used. Frequency signal conditioner (DRN-FP) module were used to convert the frequency of the AC signal from flow meter to current output which is supplied to the DAQ for reading and recording data.

Flow Meter	Model No	End Connection	Range	Accuracy
Water	Turbines Inc- WM0600x6	6" Wafer Style	250-2500 GPM	±1%
Air	Omega-FTB-938	1½" MNPT	8-130 ACFM	±1%
Water	Omega-FTB-1431	1½" MNPT	15-180 GPM	±1%
Air	Omega-FTB-933	1/2" MNPT	1-10 ACFM	±1%

Table 3-1: List of different Flow meters

The main purpose of testing the 4-Stage pump is to evaluate the performance of the pump for different operating conditions. Figure 3-13 shows the line diagram of the pump with different instruments. Static pressure taps are located at the inlet and outlet of the pump and on four stages of the diffuser. In order to measure the variation of pressure in the diffuser, static pressure taps were located along the length of the diffuser in the meridional plane of one diffuser blade flow path. On the first stage of the diffuser pressure taps are located on the suction side, pressure side and meridional plane on one blade flow path.

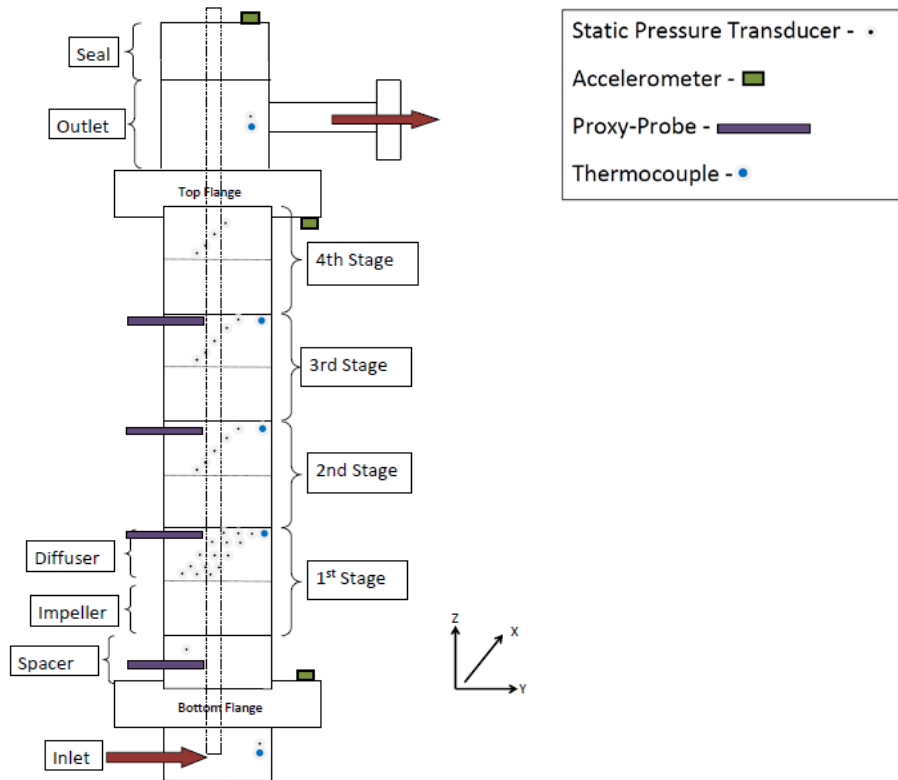


Figure 3-13: Line diagram of the pump with different instruments

The pressure taps are 1/16" diameter, flush mounted in the diffuser as shown in Figure 3-14. Table 3-2 shows the list of different pressure transducers used and their specifications. For the clear pump, two pressure transducers were used with pressure taps located at the inlet and outlet of the pump.

In order to measure the variation of temperature as the flow passes through the pump, thermocouples were mounted at various locations in the pump as shown in Figure 3-13. Table 3-3 shows the list of thermocouple used. For the clear pump temperature was measured at inlet and outlet of the pump using two thermocouples.



Figure 3-14: Static Pressure Taps on Diffuser

Transducer Type	Range (psi)	Output	Accuracy
Omega-PX 429-750GI	0-750	4-20 mA	±0.08%
Omega-PX 429-500GI	0-500	4-20 mA	±0.08%
Omega-PX481A-1000G5V	0-1000	1-5 Vdc	0.3%
Omega-PX481A-500G5V	0-1000	1-5 Vdc	0.3%

Table 3-2: List of Pressure Transducers and Specifications

For vibration monitoring of the pump, accelerometers and proximity probes were used. Three tri-axial accelerometers were mounted at various locations on the pump as shown in Figure 3-13. It is important to measure the orbit of the shaft to make sure the pump is running smoothly. Two Proximity probes were located in the xy-plane at 4-different locations as shown in Figure 3-13.

Thermocouple	Range	Diameter	Accuracy
Omega -T-Type	328-663 (°F)	1/16"	1 (°C)
Omega -T-Type	328-663 (°F)	1/8"	1 (°C)

Table 3-3: List of Thermocouples and Specifications

For vibration monitoring of the pump, accelerometers and proximity probes were used. Three tri-axial accelerometers were mounted at various locations on the pump as shown in Figure 3-13. It is important to measure the orbit of the shaft to make sure the pump is running smoothly. Two Proximity probes were located in the xy-plane at 4-different locations as shown in Figure 3-13.

Transducer	Type	Range	Resolution	Sensitivity
Accelerometer	PCB-356A17	±10g pk	0.00006 g	500 mV/g
Proximity Probe	Bently Nevada-3300 XL NSv	10 – 70 mils		205 mV/mil

Table 3-4: Details of Accelerometer and Proximity Probes

The power supplied to the electric motor was obtained from the VFD. The efficiency of the electric motor is assumed to be 98% for calculating power supplied to the pump.

3.1.3 Flow Visualization

For performing two phase flow visualization on the single stage clear pump, a high speed camera and two different light sources were used. A Phantom V 711 high

speed camera (Figure 3-15) was used for flow visualization. Specifications of the camera are listed in Table 3-5.

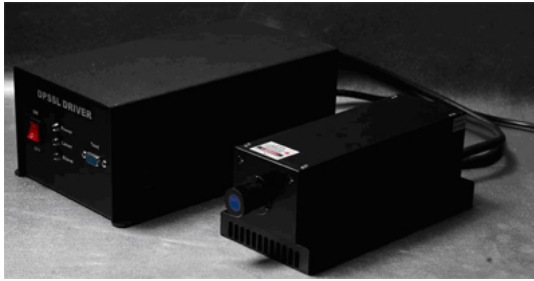


Figure 3-15: Phantom V711 High Speed Camera

Camera	Maximum Speed	Resolution at Maximum Speed	Pixel Size	Maximum Resolution	Speed at Maximum resolution
Phantom V711	1,400,000 FPS	128 x 8	20 μm	1280 x 800	7530 FPS

Table 3-5: Specifications of Phantom V711 High Speed Camera.

Bubble diameter was measured using a 1 watt, 532 nm continuous beam solid state laser. The laser is shown in Figure 3-16(a). A 180 watt, high intensity fiber light source was used to visualize the bulk flow as shown in Figure 3-16(b).



(a)



(b)

Figure 3-16: a. LSR 532H-1W laser b. High Intensity Fiber light source.

Module	Quantity	Range	Function
NI 9205	3	± 10 V	Analog Input Module
NI-9265	1	0 to 20 mA	Analog Output Module
NI-9213	1	T-Type	Thermocouple Input Module
NI-9215	6	± 10 V	Simultaneous Analog Input Module

Table 3-6: List of Different Modules used for DAS

3.1.4 Data Acquisition System

For recording and monitoring data, controlling different valves, high speed computer data acquisition system (DAS) was used. Two NI cRIO-9074 chassis having 8-slots each, 400 MHz controller and 2M gate FPGA with different modules (Table 3-6) were used. The data from the chassis was obtained using LabVIEW software. For obtaining pressure, temperature, flow rate, and electric motor VFD data, the chassis was operated in the scan interface mode at a frequency of 1 kHz. Figure 3-17 shows the front panel of the Lab view program which was operated in scan interface mode. Valve

positions were adjusted using PID controllers, where water valve was adjusted according to a set water flow rate value, air valve using a set GVF value and outlet valve using a set inlet pressure.

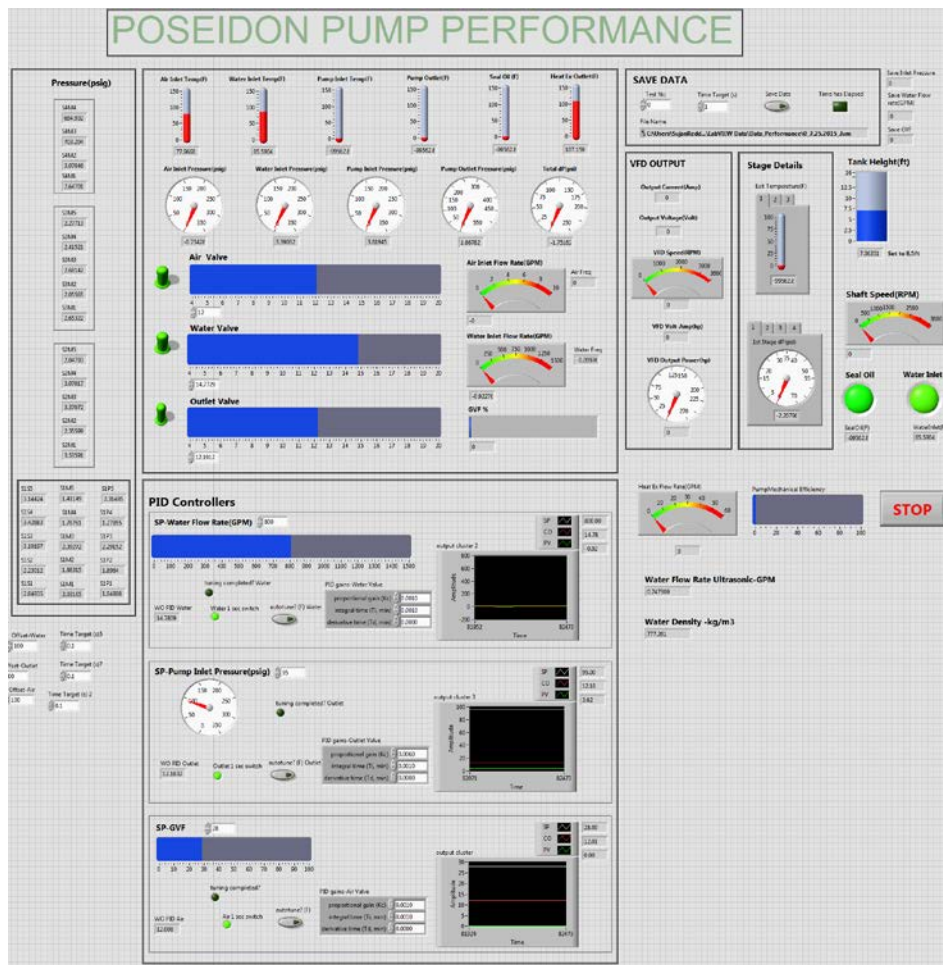


Figure 3-17: Screen Shot of Front Panel Window of Performance VI in LabVIEW

For vibration monitoring of the pump, a second chassis was used, it was operated in FPGA mode with simultaneous data stored at a frequency of 25 kHz for a

time period of 1 second using NI-9215 Modules. Figure 3-18 shows the front panel of Lab view Program for the chassis which is operated in FPGA mode.

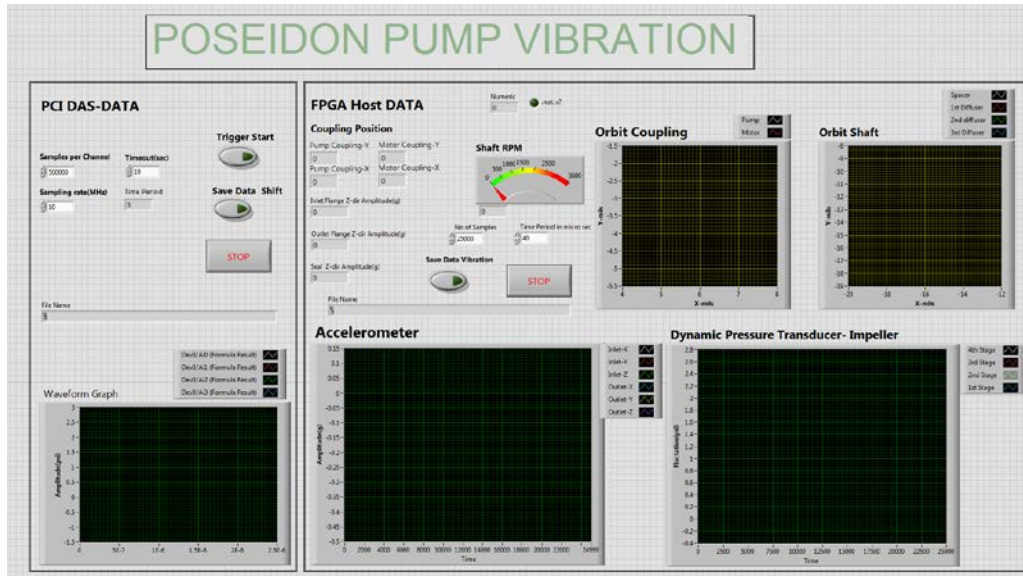


Figure 3-18: Screen Shot of Front Panel Window of Vibration Monitoring VI in LabVIEW

3.1.5 Test Matrix

In order to obtain the performance map of the 4-stage pump, the pump was operated for different conditions which are listed in Table 3-7.

Inlet Pressure(psig)	Rotational Speed(RPM)	Water Flow Rate(BPD)	GVF (%)	
40	3600	10000 (291 GPM)	0	5
100	3000	15000 (437 GPM)	10	15
200		20000 (583 GPM)	20	25
300		25000 (729 GPM)	30	35
		30000 (875 GPM)	40	45
		35000 (1021 GPM)	50	55
		40000 (1167 GPM)	60	65
		45000 (1313 GPM)	70	

Table 3-7: Test Matrix for 4-Stage Pump

The Single stage Clear Pump was tested to obtain bubble diameter and bulk flow motion in the pump. The test conditions are listed in Table 3-8

Inlet Pressure(psig)	Rotational Speed(RPM)	Water Flow Rate(BPD)	GVF (%)	
50	1800	11428 (250 GPM)	0	2
		13714 (300 GPM)	4	6
		16000 (350 GPM)	8	
		18285 (400 GPM)		

Table 3-8: Test Matrix for Single Stage Clear Pump

3.2 Numerical Methodology

Numerical simulations were performed on the 4-Stage pump that was tested. Simulations were carried out stage by stage for the first two stages. Simulations were carried out for single phase and two phase fluid using the commercial software ANSYS-Fluent. The flow paths were obtained by using impeller and diffuser 3-D model from Solid works as shown in Figure 3-19. Since the impeller is unshrouded, the tip clearance was modeled.

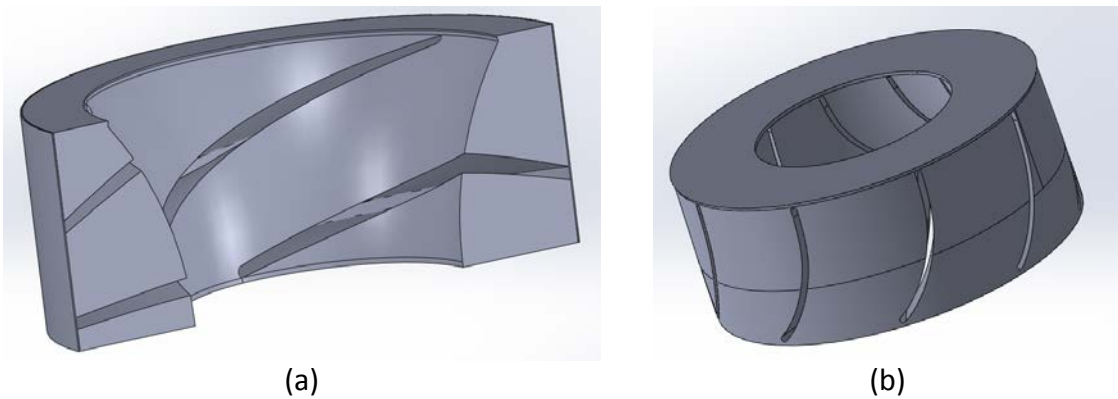


Figure 3-19: Flow path a. Impeller b. Diffuser

The flow paths were then exported to Gambit/ ICEM CFD for the purpose of meshing. The impeller was meshed in Gambit and the diffuser was meshed in ICEM CFD. Complete hexahedral elements were used for meshing with a total of 5.21 million elements for the single stage pump.

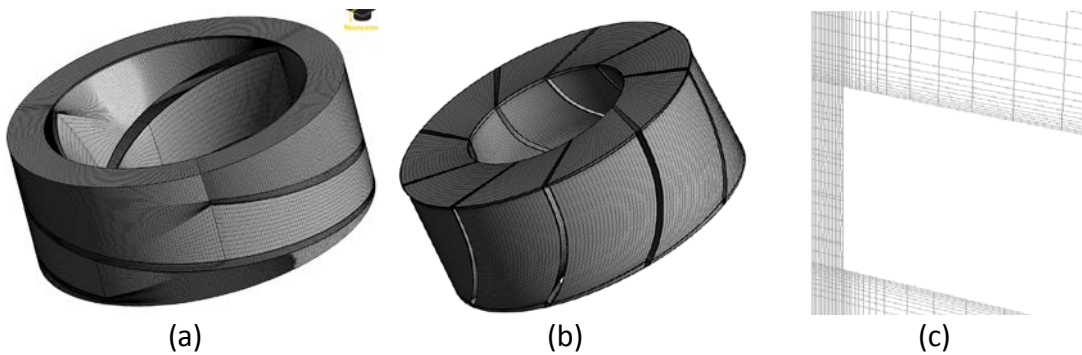


Figure 3-20: Mesh a. Impeller b. Diffuser c. Impeller tip clearance

Figure 3-20 shows the mesh of different fluid zones for a single stage pump. The mesh was then exported to Fluent 15.0 to solve for the flow field.

3.2.1 Single Phase Simulations

The single stage pump flow domain was solved using Reynolds Averaged Navier Stokes Equations (RANS). The RANS equations are

$$\frac{\partial \rho}{\partial t} + \frac{\partial}{\partial x_i} (\rho \bar{u}_i) = 0 \quad 3-1$$

$$\frac{\partial}{\partial t} (\rho \bar{u}_i) + \frac{\partial}{\partial x_j} (\bar{u}_i \bar{u}_j) = -\frac{\partial \bar{p}}{\partial x_i} + \frac{\partial}{\partial x_j} \left[\mu \left(\frac{\partial u_i}{\partial x_j} + \frac{\partial u_j}{\partial x_i} - \frac{2}{3} \delta_{ij} \frac{\partial u_l}{\partial x_l} \right) \right] + \frac{\partial}{\partial x_j} (-\rho \overline{u'_i u'_j}) \quad 3-2$$

The above equations are similar to Navier-Stokes equations with the velocity represented by time averaged velocity and an extra term in the momentum equation

3-2. The extra terms are called Reynolds stresses. According to the Boussinesq hypothesis, Reynolds stresses are related to the mean velocity gradients using the equation:

$$-\overline{\rho u'_i u'_j} = \mu_t \left(\frac{\partial u_i}{\partial x_j} + \frac{\partial u_j}{\partial x_i} \right) - \frac{2}{3} \left(\rho k + \mu_t \frac{\partial u_k}{\partial x_k} \right) \delta_{ij} \quad 3-3$$

Where μ_t is turbulent viscosity, that can be modeled using one equation or two equation model. For the present problem, μ_t was modeled using Realizable k- ϵ model where two additional transport equations were modeled for turbulent kinetic energy, k and turbulent dissipation rate, ϵ which are listed below

$$\frac{\partial}{\partial t}(\rho k) + \frac{\partial}{\partial x_j}(\rho k u_j) = \frac{\partial}{\partial x_j} \left[\left(\mu + \frac{\mu_t}{\sigma_k} \right) \frac{\partial k}{\partial x_j} \right] + P_k + P_b - \rho \epsilon - Y_M + S_k \quad 3-4$$

$$\frac{\partial}{\partial t}(\rho \epsilon) + \frac{\partial}{\partial x_j}(\rho \epsilon u_j) \quad 3-5$$

$$= \frac{\partial}{\partial x_j} \left[\left(\mu + \frac{\mu_t}{\sigma_\epsilon} \right) \frac{\partial \epsilon}{\partial x_j} \right] + \rho C_1 S_\epsilon - \rho C_2 \frac{\epsilon^2}{k + \sqrt{V \epsilon}} + C_{1\epsilon} \frac{\epsilon}{k} C_{3\epsilon} P_b + S_\epsilon$$

Where

$$C_1 = \max \left[0.43, \frac{\eta}{\eta + 5} \right], \quad \eta = S \frac{k}{\epsilon}, \quad S = \sqrt{2 S_{ij} S_{ij}} \quad 3-6$$

In the above equations G_k represents the generation of turbulence kinetic energy due to mean velocity gradient, G_b is the generation of turbulent kinetic energy due to buoyancy, Y_M is the contribution of the fluctuating dilatation in compressible turbulence to the overall dissipation rate. σ_k and σ_ϵ are turbulent Prandtl numbers for k and ϵ . S_k and S_ϵ are user defined source terms for k and ϵ . $C_{1\epsilon}$ and C_2 are the constants.

Turbulent viscosity μ_t is a function of k and ε and is computed using the equation

$$\mu_t = \rho C_\mu \frac{k^2}{\varepsilon} \quad 3-7$$

Where C_μ is computed using the equation

$$C_\mu = \frac{1}{A_0 + A_s \frac{kU^*}{\varepsilon}} \quad 3-8$$

A_0 and A_s are model constants which are given by

$$A_0 = 4.04, \quad A_s = \sqrt{6} \cos \phi$$

$$\phi = \frac{1}{3} \cos^{-1}(\sqrt{6} W), \quad W = \frac{S_{ij}S_{jk}S_{ki}}{\tilde{S}^3}, \quad \tilde{S} = \sqrt{S_{ij}S_{ij}}, \quad S_{ij} = \frac{1}{2} \left(\frac{\partial u_j}{\partial x_i} + \frac{\partial u_i}{\partial x_j} \right) \quad 3-9$$

Where U^* is computed using the equation

$$U^* = \sqrt{S_{ij}S_{ij} + \tilde{\Omega}_{ij}\tilde{\Omega}_{ij}} \quad 3-10$$

$$\tilde{\Omega}_{ij} = \Omega_{ij} - 2\varepsilon_{ij}\omega_k, \quad \tilde{\Omega}_{ij} = \Omega_{ij} - 2\varepsilon_{ijk}\omega_k, \quad \Omega_{ij} = \bar{\Omega}_{ij} - 2\varepsilon_{ijk}\omega_k$$

The modal constants for the k - ε model are

$$C_{2\varepsilon} = 1.9, C_{2\varepsilon} = 1.3, \sigma_k = 1.0, \sigma_\varepsilon = 1.2$$

Reynolds stresses were modeled using the Realizable K-epsilon model with standard wall functions. The law of the wall for mean velocity for momentum equation is given by the equation

$$U^* = \frac{1}{\kappa} \ln(Ey^*) \quad 3-11$$

Where $U^* \equiv \frac{U_P C_\mu^{1/4} K_P^{1/2}}{\tau_w / \rho}$ and $y^* \equiv \frac{\rho C_\mu^{1/4} k_P^{1/2} y_P}{\mu}$

κ is the von Karman constant(0.4187), E is empirical constant(9.793), U_P is the mean velocity at near wall node P, k_P is the turbulent kinetic energy at near wall node P, y_P is the distance from point P to wall and μ is dynamic viscosity of fluid.

In ANSYS FLUENT Log law is used when $Y^* > 11$. When $Y^* < 11$ ANSYS FLUENT uses laminar stress strain relationship which is given by

$$U^* = y^* \tag{3-12}$$

3.2.1.1 Boundary Conditions

Stages by stage transient simulations were performed on the 4-Stage Pump which has been tested. A single stage pump domain is a combination of two different fluid domains namely impeller and diffuser. Non-conformal interface was specified between different fluid domains where flow is transferred from one domain to another. The impeller flow domain and its surfaces were specified with constant angular velocity to simulate the rotational effects of impeller. For the first stage simulation, mass flow rate was specified at the impeller inlet and constant pressure was specified at the diffuser outlet as boundary conditions, the remaining surfaces were specified with wall boundary condition. Transient effects of the impeller fluid domain were simulated by using the moving mesh option.

For simulating the second stage two different boundary conditions are used. In the first type, a single stage pump domain is taken and instead of specifying velocity

inlet and pressure outlet as boundary conditions, the inlet and outlet are specified as periodic boundary conditions. In the periodic boundary condition, mass flow rate is specified. Using this boundary condition, similar velocity profile at the inlet and outlet are obtained, it is a necessary condition for simulating multi stage pumps. The other boundary conditions are similar to first stage simulations. The only disadvantage of periodic boundary conditions is, it can be used only for incompressible single phase flows.

In the second type, the first stage diffuser was combined with the second stage impeller and diffuser. Diffuser-Impeller-Diffuser fluid domain was used since it properly captures the flow field instead of simulating Impeller- Diffuser for second stage since the impeller blades are very close to the inlet. For the Diffuser-Impeller- Diffuser domain, the velocity was specified at the diffuser inlet (1st Stage) as a boundary condition. This velocity was obtained from the first stage simulation and the exact profile of velocity at the diffuser inlet is transferred to second stage simulation as a boundary condition. Pressure was specified at the diffuser outlet (2nd Stage) as a boundary condition. Non- conformal interface was specified between different fluid domains, and the remaining surfaces are specified as walls.

3.2.2 Two Phase Simulations

Stage by stage two phase simulations were carried out for the 4-stage pump which was tested using water and air as fluids. The Eulerian multiphase model in ANSYS

FLUENT was used for modeling separate, yet interacting phases. In this model, the momentum and continuity equations were solved for each phase with single pressure shared by all phases and phase volume fraction α_q was used to identify the space occupied by each phase.

The volume of phase q, V_q is defined by

$$V_q = \int_V \alpha_q dV \quad 3-13$$

Where

$$\sum_{q=1}^n \alpha_q = 1$$

n is the number of phases, n=2 for this problem

The continuity equation for each phase is given by

$$\frac{\partial}{\partial t} (\alpha_q \rho_q) + \nabla \cdot (\alpha_q \rho_q \vec{v}_q) = \sum_{p=1}^n (\dot{m}_{pq} - \dot{m}_{qp}) + S_q \quad 3-14$$

Where \vec{v}_q the velocity of phase q, ρ_q the density of phase q, \dot{m}_{pq} represents the mass transfer from pth to qth phase and S_q is the source term.

The momentum equation for each phase is given by the equation

$$\frac{\partial}{\partial t}(a_q \rho_q \vec{v}_q) + \nabla \cdot (a_q \rho_q \vec{v}_q \vec{v}_q)$$

3-15

$$= -a_q \nabla p + \nabla \cdot \bar{\tau}_q + a_q \rho_q \vec{g} + \sum_{p=1}^n (\vec{R}_{pq} + \dot{m}_{pq} \vec{v}_{pq} - \dot{m}_{qp} \vec{v}_{qp})$$

$$+ (\vec{F}_q + \vec{F}_{lift,q} + \vec{F}_{wl,q} + \vec{F}_{vm,q} + \vec{F}_{td,q})$$

Where \vec{F}_q is external body force, $\vec{F}_{lift,q}$ is lift force, $\vec{F}_{wl,q}$ is wall lubrication force, $\vec{F}_{vm,q}$ is virtual mass force, and $\vec{F}_{td,q}$ is turbulent dispersion force. p is the pressure shared by all phases.

\vec{R}_{pq} is the interaction forces between phases which depends on friction, cohesion, pressure, and other effects and is related by $\vec{R}_{pq} = -\vec{R}_{qp}$ and $\vec{R}_{pp} = 0$. In ANSYS fluent it is given by the equation

$$\sum_{p=1}^n \vec{R}_{pq} = \sum_{p=1}^n K_{pq} (\vec{v}_p - \vec{v}_q)$$

3-16

Where v_p and v_q are phase velocities and K_{pq} is interphase momentum exchange coefficient

As the flow passed through the pump, there was a variation of pressure in the flow field which translated to variation in density. In Water–Air simulations water is treated as incompressible fluid, air as compressible fluid. The density of air was calculated using Ideal gas law. In order to account for the temperature in ideal gas law, the energy equation must be solved when using compressible fluid. The energy equation for each phase is given by the equation

$$\begin{aligned}
& \frac{\partial}{\partial t} (a_q \rho_q h_q) + \nabla \cdot (a_q \rho_q \vec{u}_q h_q) & 3-17 \\
& = a_q \frac{\partial \rho_q}{\partial t} + \bar{\tau}_q \cdot \nabla \vec{u}_q - \nabla \cdot \vec{q}_q + S_q \\
& + \sum_{p=1}^n (Q_{pq} + \dot{m}_{pq} h_{pq} - \dot{m}_{qp} h_{qp})
\end{aligned}$$

Where h_q is the specific enthalpy of q^{th} phase, \vec{q}_q is the heat flux, h_{pq} is the interphase enthalpy, and S_q is the source term.

For liquid – gas flows secondary phase is assumed to be in the form of droplets or bubbles. The exchange coefficient for these flows is calculated using the equation

$$K_{pq} = \frac{\rho_p f}{6\tau_p} d_p A_i \quad 3-18$$

Where A_i is the interfacial area, d_p is the diameter of bubble or droplets, f is the drag function and τ_p is the particle relaxation time which is given by

$$\tau_p = \frac{\rho_p d_p^2}{18\mu_q} \quad 3-19$$

Similar to single phase flows for multi-phase turbulence closure, per phase Realizable k - ϵ turbulence model is used with standard wall functions. In this model k , ϵ transport equations were solved separately for each phase. Since air and water were used as test fluids, where the density ratio is greater than 1, the mixture turbulence model or dispersed turbulence model does not accurately capture important features of turbulent flow.

3.2.2.1 Boundary Conditions

For two phase simulations water and air were used as test fluids. These fluids were not homogenized before entering the first stage impeller since water and air entered from different inlets as shown in Figure 3-21(a). In order to simulate for the exact test conditions, the flow domain prior to first stage impeller (Inlet body) as shown in Figure 3-21(a) was simulated to obtain the approximate mass distribution of air and water at the inlet of impeller. Boundary conditions for this domain were constant mass flow rate at two inlets and constant pressure at the Outlet.

Fluent does not have the capability to transfer the mass profile of air and water from the boundary surfaces. The outlet of the inlet body flow domain and the first stage impeller inlet are divided in to 16 zones so that the average mass flow rate can be used to simulate the first stage flow domain as shown in Figure 3-21.

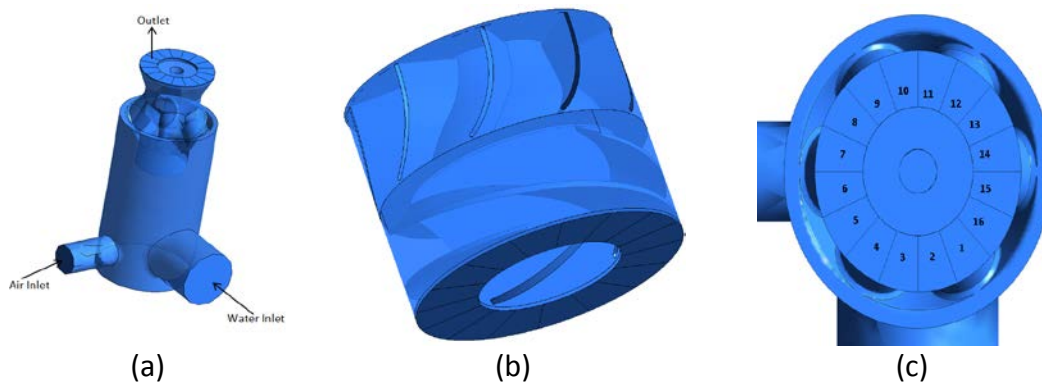


Figure 3-21 a. Inlet Body Flow Domain b. Pump First Stage Flow Domain c. Zone numbers on mixer body outlet

Similar to single phase simulations, the boundary conditions for two phase simulations were constant mass flow rate of air and water at the impeller inlet, constant pressure is specified at outlet of the diffuser and remaining surfaces are specified as wall. Non conformal interface was used between impeller outlet and diffuser inlet surfaces. For the impeller fluid domain and its surfaces constant angular velocity was specified to simulate the rotational effects of the impeller. Transient simulations with a time step of 1degree were used to simulate the impeller diffuser interaction.

For simulating the second stage, similar to second type single phase simulation, diffuser-impeller- diffuser flow domain is considered. Homogenous mass flow was specified at the diffuser inlet (1st Stage) and constant pressure was specified at diffuser outlet (2nd Stage) as boundary conditions. The remaining surfaces were treated similar to single phase simulations.

3.2.3 Simulation Matrix

Single Phase CFD simulations were carried out for liquid flow rates from 15 kBPD to 40 kBPD at 3600 RPM. Two phase simulations were performed for liquid flow rates ranging from 25 kBPD to 35 kBPD with varying GVF of 10 to 50 % at 3600 RPM and 200 psig Inlet pressure.

3.3 Theory

Affinity laws for pumps are used to predict the performance for changes in operating conditions or pump dimensions. They are obtained using dimensionless analysis. The three basic equations are given by

$$K_1 = \frac{Q}{ND^3} \quad 3-20$$

$$K_2 = \frac{\Delta p}{\rho_{mix} N^2 D^3} \quad 3-21$$

$$K_3 = \frac{P}{\rho_{mix} N^3 D^5} \quad 3-22$$

Where Q is liquid flow rate, N is rotational speed, D is impeller diameter, Δp is pressure rise in pump, ρ_{mix} is incompressible fluid density, P is the power consumed and K_i is constant.

The above laws are valid for homogenous incompressible fluids, with no inlet flow effects.

For two phase flows, the general description of the flow is based on volume flow rates and not on mass flow rates. Since the density of gas phase is very low, higher volumetric flow rates of gas phase tend to be very small or negligible when viewed in mass flow rate domain. The gas volume fraction (GVF) equation is used to define the ratio of volume occupied by two phases, it is given by

$$GVF = \frac{Q_g}{Q_l + Q_g} \quad 3-23$$

Where Q_l is liquid flow rate and Q_g is gas flow rate.

The density of mixture (ρ_{mix}) in a two phase flow is calculated using the equation

$$\rho_{mix} = \rho_l(1 - GVF) + \rho_g GVF \quad 3-24$$

Where ρ_l is density of liquid phase and ρ_g is density of gas phase.

The head rise in the pump is calculated using the equation

$$h = \frac{\Delta p}{\rho_{mix} g} \quad 3-25$$

Where Δp is the pressure rise per stage or total pump, ρ_{mix} is the stage inlet density and g is gravity constant.

The efficiency of the pump is calculated using the equation

$$\eta = \frac{P_{fluid}}{P_{Motor}} \quad 3-26$$

Where P_{fluid} is the energy consumed by the fluid and P_{Motor} is the energy consumed by the electric motor.

For two phase flow the energy consumed by the fluid is given by

$$P_{fluid} = P_{liquid} + P_{gas} \quad 3-27$$

Where P_{liquid} is the energy consumed by the liquid phase and P_{gas} is the energy consumed by the gas phase.

Since the liquid is incompressible, the energy consumed by the liquid phase is given by the equation

$$P_{liquid} = Q_l(\Delta p) \quad 3-28$$

As the flow passes through the pump, there is a pressure rise in the pump and the volume occupied by the gas phase reduces. The energy consumed by the gas phase is given by the equation

$$P_{gas} = \int Q_g dp \quad 3-29$$

Assuming that there is no change in temperature of gas from inlet to outlet of the pump i.e the process is isothermal. The energy consumed is given by the equation

$$P_{gas} = p_{inlet} Q_{inlet} \ln \frac{p_{outlet}}{p_{inlet}} \quad 3-30$$

Where Q_{inlet} is the volume of gas at inlet, p_{inlet} is pressure at inlet and p_{outlet} is pressure at outlet.

Since power consumed by the electric motor is measured using a Variable Frequency Drive (VFD), the power consumed by the motor is given by

$$P_{motor} = 0.98 * P_{VFD} \quad 3-31$$

Where P_{VFD} is power reading obtained from VFD and assuming electrical efficiency to be 98 %.

4 RESULTS AND DISCUSSION

This chapter is divided in to three sections covering experimental data, flow visualization and CFD simulations.

4.1 Experimental Results

The performance of the 4-stage helico-axial pump is discussed in this section. Steady state, stage by stage, experimental measurements are obtained for the operating conditions listed in Table 3-7.

4.1.1 Pump Performance

Figure 4-1 shows the performance map of the 4-stage pump at 100 psig inlet pressure, 3600 RPM for different pump inlet GVF. Figure 4-1(a) shows the pressure rise in the 4-stage pump for different flow rate and GVF. The total flow rate is obtained by summing the liquid and gas flow rates at the pump inlet pressure. From this figure, pressure rise decreases as flow rate increases for any fixed GVF.

The lower limit for the total flow rate is not based on surging, it was due to limitation of minimum liquid flow rate of 10 kBPD. Since this test loop is closed, surging conditions were not noticed. However, at lower inlet pressure of 40 psi, for 10 kBPD liquid flowrate the pump was unstable when gas is added. The maximum flow rate is limited by the pump ability to circulate the fluid. Figure 4-2 shows the system curve of the test rig, from this figure at maximum rotational speed of 3600 RPM, the pump can handle 45 kBPD with a pressure rise of 55 psi. At the maximum rotational speed, as the

flow rate increases the pressure drop in the system increases and the pressure rise generated by the pump decreases which limits the maximum flow rate to 45 kBPD.

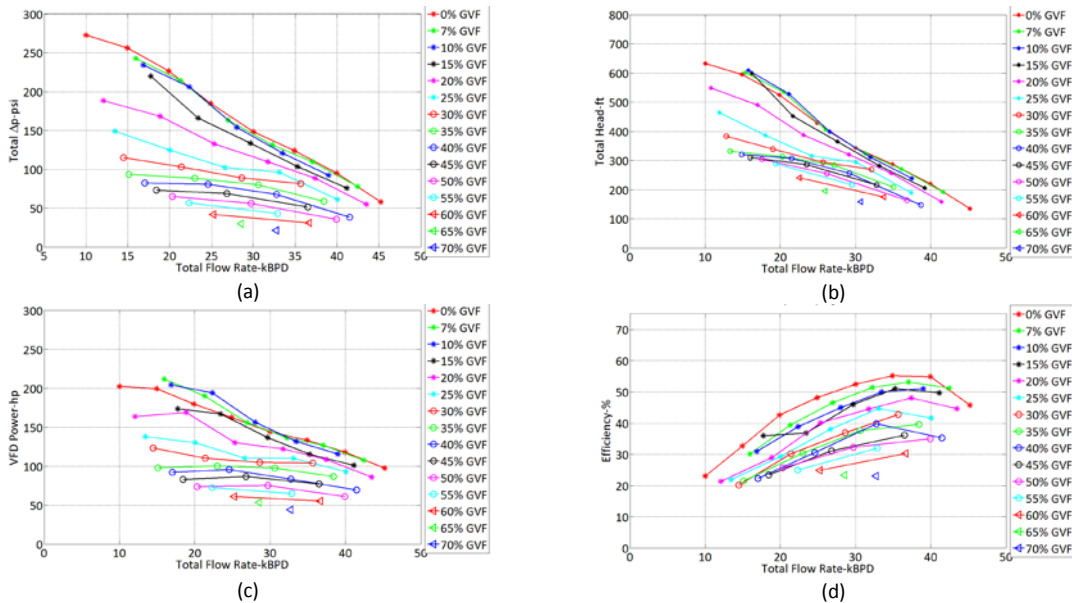


Figure 4-1: Performance map of the 4-stage pump at 100 psig inlet pressure, 3600 RPM (a) Total dP (b) Total head (c) Power (d) Efficiency

Figure 4-1(b) shows the head rise in the 4-stage pump for different flow rates and GVF at 100 psig inlet pressure and 3600 RPM. For low GVF conditions (< 15%) the head rise in the pump is similar to pure liquid flow conditions. As air is added to the system, head degradation occurs due to compressing air, at low GVF conditions it has been negated by the reduced friction losses in the pump. As GVF increases, the head degradation due to compressing air increases and also there is a slip between the two phases which increases the hydraulic losses in the system. Because of slip between the phases, gas bubbles tend to move slower and accumulate on the pressure side of the

diffuser blade, which increases the flow losses. From Figure 4-1(b) for $GVF > 15\%$ the head drops with increase in GVF for any fixed total flow rate.

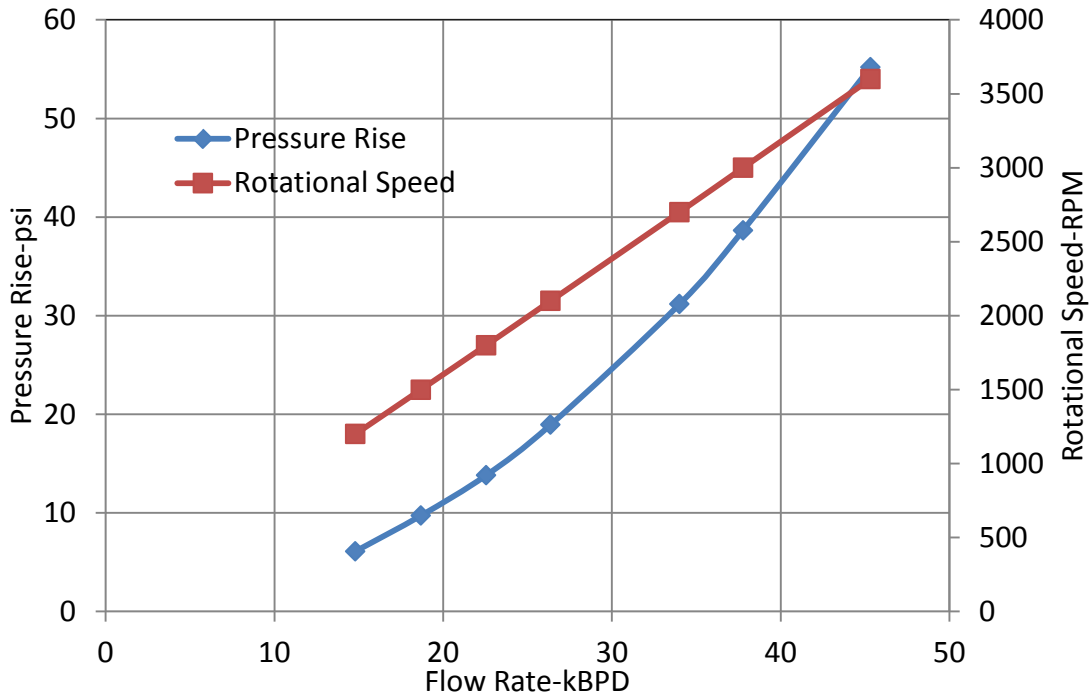


Figure 4-2: System Curve of the test rig

Figure 4-1(c) shows the power consumed by the electric motor of the 4-stage pump for different flow conditions at 100 psig inlet pressure and 3600 RPM. Since the pump design is a hybrid of an axial flow compressor and a centrifugal pump, the power consumed by the pump decreases with increase in flowrate. With increase in GVF , the power consumed by the pump decreases, because of reduced head generated by the pump.

Figure 4-1(d) shows the variation in mechanical efficiency of the 4-stage pump for different flow conditions at 100 psig Inlet pressure and 3600 RPM. The BEP of the pump is around 35 kBPD at 0% GVF. The maximum efficiency of this pump is limited to 55% which is less than a standard mixed flow pump. With increase in GVF the efficiency drops due to increase in hydraulic losses. The BEP shifts to lower flow rates with increase in GVF.

4.1.2 Effect of Inlet Pressure

Figure 4-3 shows the performance comparison of the pump for two different inlet pressures 40 psig and 300 psig at 3600 RPM. For incompressible fluid there should be no change in pump performance since density is constant. From Figure 4-3(a), at 0% GVF the pressure rise for 40 psig and 300 psig inlet pressure are almost the same. The difference between the two curves is within the standard deviation of the measurements. With increase in GVF there is no change in pressure rise until GVF=20%, after which the pressure rise is higher for higher inlet pressure. The same can be inferred from affinity laws Equation 3-21 even though they are not defined for two phase flows. With increase in inlet pressure the compressibility of gas decreases and the bubbles at the inlet of the pump are smaller in diameter. Due to this, for a high GVF flow condition at lower inlet pressure, head degradation is higher as shown in Figure 4-3(b).

Figure 4-3(c) shows the power consumption of the pump for different inlet pressures. Since the head rise is not affected by inlet pressure for $GVF \leq 20\%$, there is no change in power consumed by the pump. For $GVF > 20\%$, since the head rise increases the power consumed also increases. The increase in power can be related to the affinity law equation 3-22.

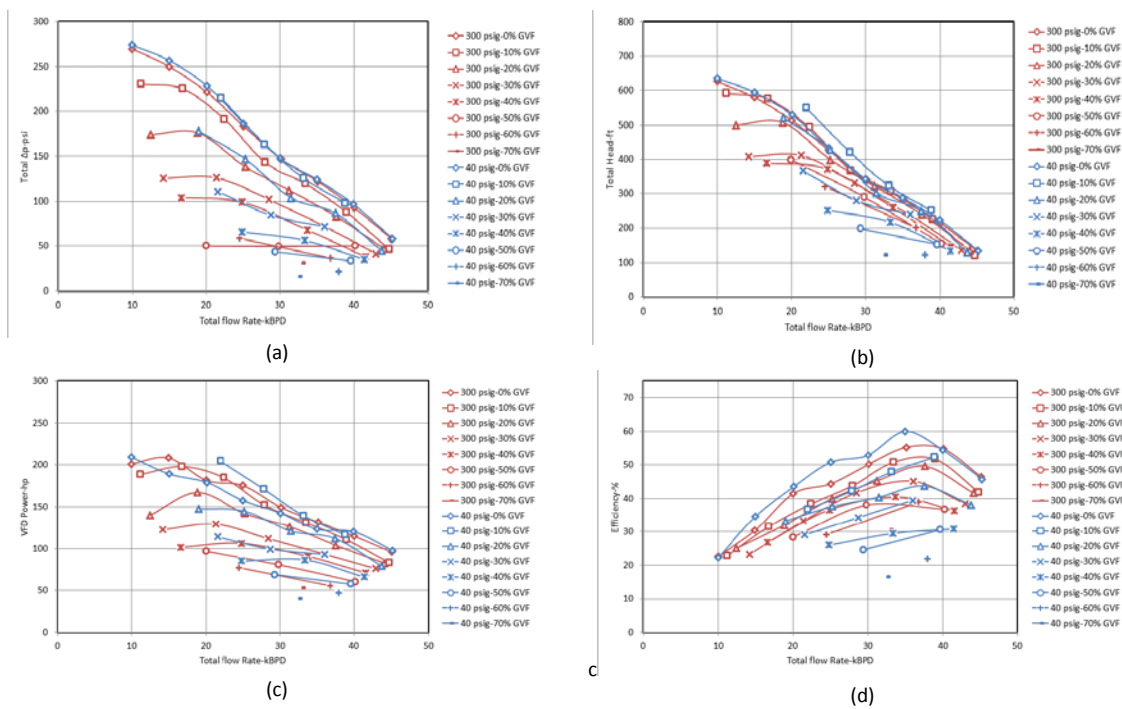


Figure 4-3: Performance map comparison of the 4-stage pump at 300 psig and 40 psig Inlet Pressure, 3600 RPM (a) Total dP (b) Total head (c) Power (d) Efficiency

Figure 4-3(d) shows the efficiency comparison of the pump for different inlet pressures. Similar to pressure rise, the efficiency is higher for higher inlet pressure when $GVF > 20\%$ because of lower head degradation.

4.1.3 Effect of Rotating Speed

Figure 4-4 shows the performance comparison of the pump for two different rotating speeds at 100 psig inlet pressure for different flow conditions. Since the pump has partly radial and axial behavior, rotating speed affects the pump performance because of an increase in the centrifugal forces.

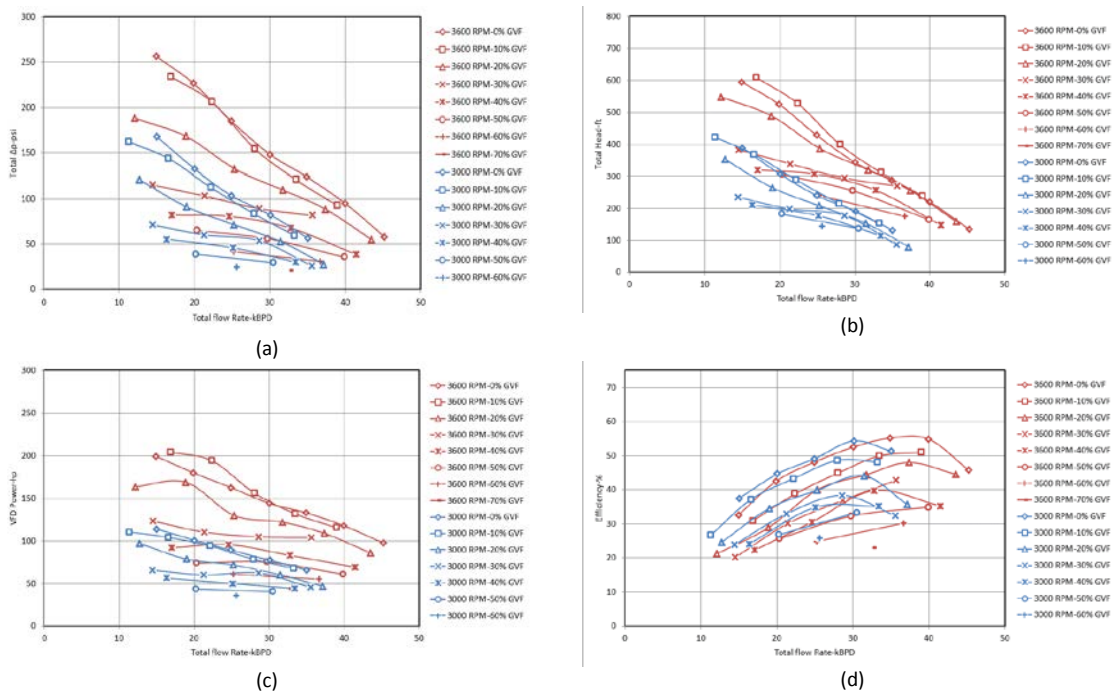


Figure 4-4: Performance map comparison of the 4-stage pump at 100 psig inlet pressure, 3600 RPM and 3000 RPM (a) Total dP (b) Total head (c) Power (d) Efficiency

Figure 4-4(a) shows the effect of rotating speed on pressure rise for different flow conditions. With increase in RPM the pressure rise is larger and the operating zone of the pump is extended to higher flow rates. As the RPM increases higher GVF's are possible because the bubbles in the impeller are chopped in to finer size which reduces

the head degradation in the pump. The head versus flow rate behavior of the pump is shown in Figure 4-4(b).

Because of higher pressure rise or head, the power consumption is higher with increase in RPM as shown in Figure 4-4(c). The efficiency of the pump is not a strong function of RPM. Only for flowrates higher than BEP it is advisable to run the pump at higher rotating speeds for maximizing the efficiency.

Conventional way of obtaining the performance of the pump at different rotating speeds, for an incompressible fluid is through affinity laws and with experimental data at any rotating speed. From Equation 3-21, the pressure rise in the pump is directly proportional to square of rotating speed. Figure 4-5 shows a comparison between the affinity laws and experimental data for 3600 RPM. The affinity laws data for 3600 RPM was obtained from 3300 RPM experimental data. From Equation 3-22, the power consumed by the pump is directly proportional to cube of rotating speed. Figure 4-6 shows the power comparison between the affinity laws and experimental data for 3600 RPM.

From both the figures, the affinity laws tend to over predict in comparison with experimental data. The difference between them increases as flow rate increases because affinity laws are generally defined for centrifugal pumps, in a helico-axial pump, the flow is partly radial and partly axial and axial forces increase as flow rate increases.

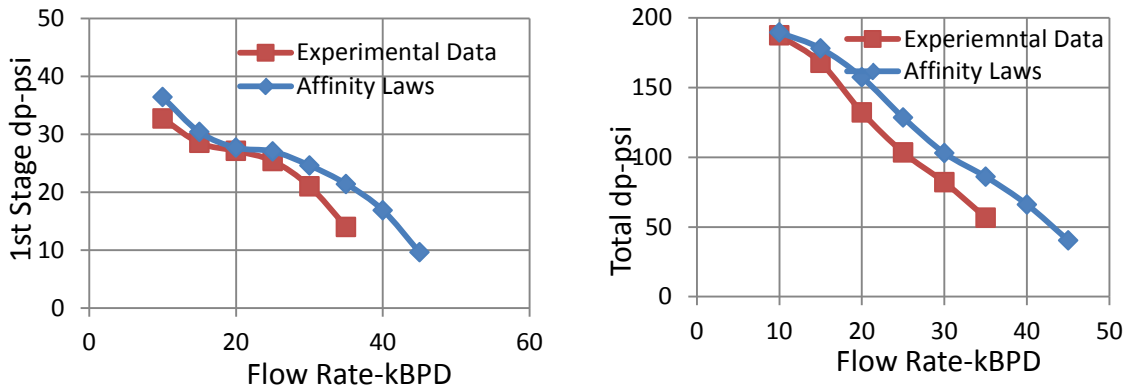


Figure 4-5: Comparison of pressure rise from affinity laws and experimental data for 3600 RPM. (a) 1st Stage (b) Total dp

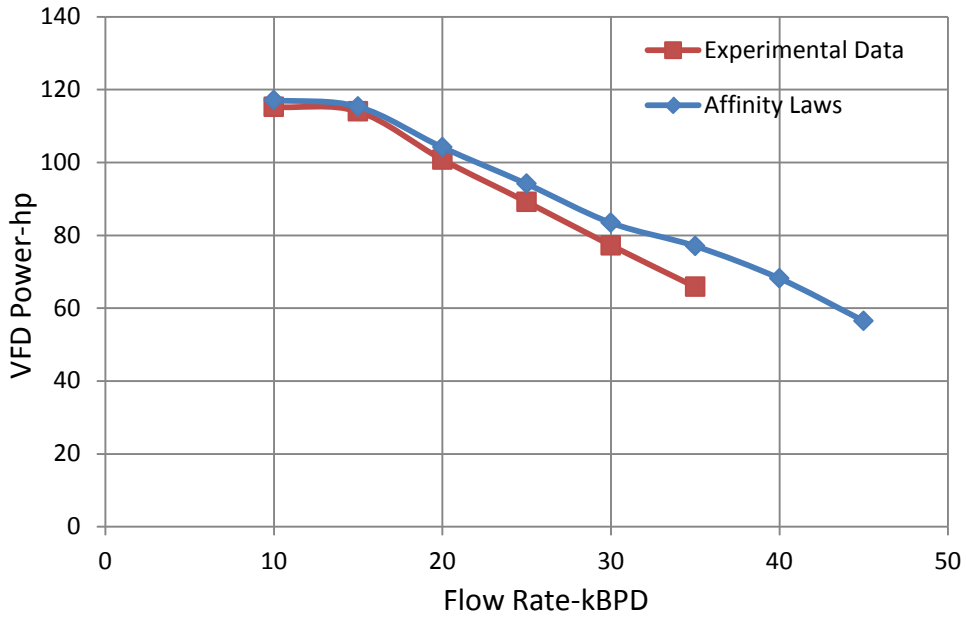


Figure 4-6: Comparison of VFD power from affinity laws and experimental data for 3600 RPM.

4.1.4 Stage By Stage Performance

As the flow traverses through the multi stage pump, the performance behavior of the multi-phase pump will not be the same from each stage because of the change in inlet flow conditions. When a compressible fluid is used, the volume of the fluid

decreases with increase in pressure in the pump. In the current scenario, the total volume at the 4th stage will be less than the 1st stage. Figure 4-7 shows the stage by stage head vs stage inlet total flow rate comparison at 200 psig inlet pressure, 3600 RPM for different pump inlet GVF conditions.

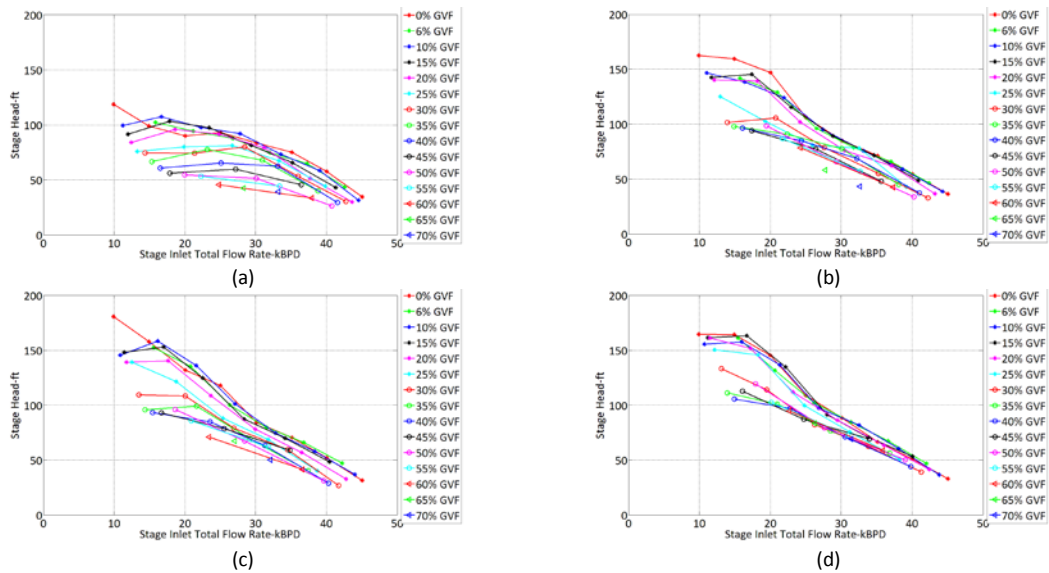


Figure 4-7: Stage by stage head versus stage inlet total flow rate comparison at 200 psig inlet pressure, 3600 RPM (a) 1st Stage (b) 2nd Stage (c) 3rd Stage (d) 4th Stage

Figure 4-7(a) shows the head versus flowrate performance curve for stage 1, the head rise is smaller in comparison with other stages because of inlet flow effects and non-homogenous inlet for the two phase flow. Due to non-homogenous inlet conditions with addition of gas, the 1st stage was close to its surging point at lower flow rates. Due to this with decrease in flow rate beyond certain range the stage head either remains constant or it decreases.

For GVF = 0%, there is no considerable change in head rise for stages 2, 3 and 4 because the flow conditions are similar. Even with slight addition of gas the flow conditions will be different at every stage because as the flow passes through the pump there will be pressure rise which reduces the GVF and total flow rate. Figure 4-8 shows the variation in the GVF at different stages of the pump as the flow passes through the pump for different inlet conditions. From Figure 4-7(b), (c) and (d) for different pump inlet GVF conditions, as flow passes through the pump the head rise per stage is increased because the GVF and total flow rate decreases as the flow traverses and bubbles are chopped into finer sizes in the impeller. The smaller the bubble diameter, head degradation is reduced.

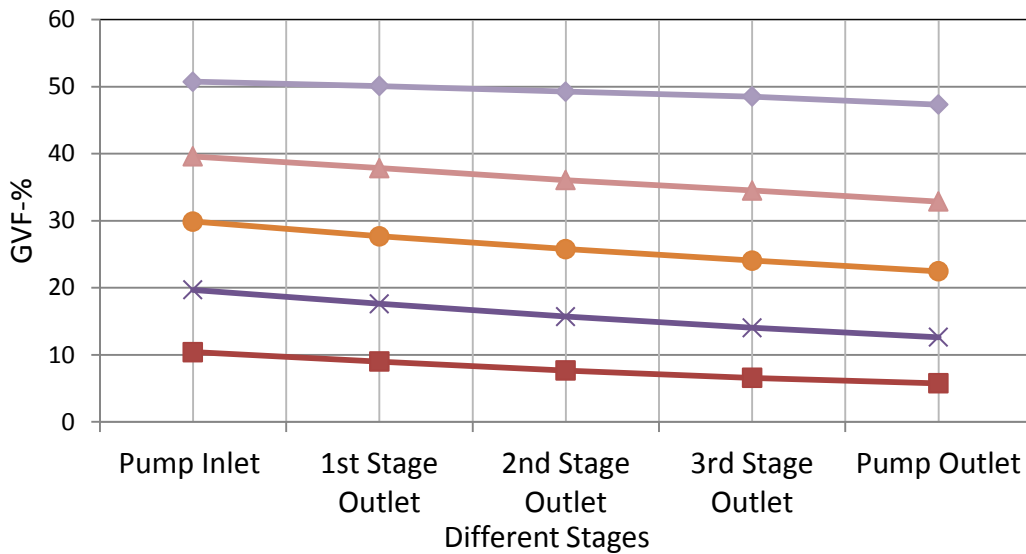


Figure 4-8: GVF variation in the pump for different inlet GVF at 200 psig inlet pressure, 20 kBPD liquid flow rate, 3600 RPM

Figure 4-9 shows the variation in temperature as the flow passes through the pump for different GVF at 20 kBPD liquid flow rate, 3600 RPM. From this graph, the variation in temperature from inlet to outlet of pump is very minimal. Equation 3-30 assumed isothermal compression for calculating the power consumed in compressing air, an assumption corroborated from this graph.

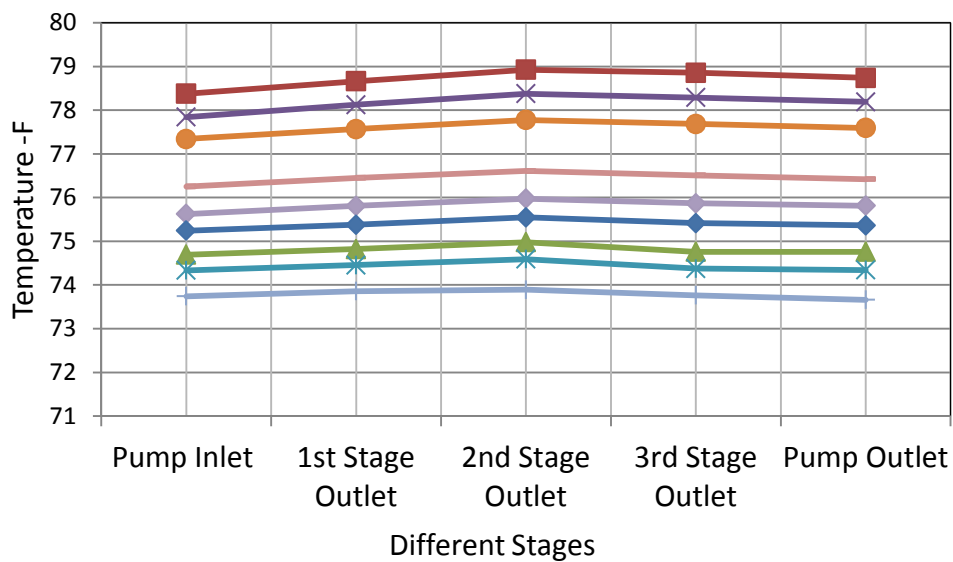


Figure 4-9: Temperature variation in the pump for different inlet GVF at 200 psig inlet pressure, 20 kBPD liquid flow rate, 3600 RPM

4.1.5 Diffuser Performance

The purpose of a diffuser in a multi stage pump is to convert kinetic energy of the fluid into pressure energy and to direct the fluid into the next stage impeller. In the current 4-stage pump, static pressure transducers are located on the meridional plane of each stage diffuser as shown in Figure 3-13. Figure 4-10 shows the variation in the

static pressure from inlet to outlet of the pump at 100 psig inlet pressure and 3600 RPM. Figure 4-10(a) shows the variation in pressure for different liquid flow rates at 0% GVF. From this graph, there is no pressure rise in the diffuser for all the four stages. However in the 4th stage diffuser for lower liquid flow rates there is a minimal variation in pressure which might be due to back flow effects. Figure 4-10(b) shows the variation in pressure for different liquid flow rates at 20% GVF, the diffuser behavior is similar to the pure liquid case.

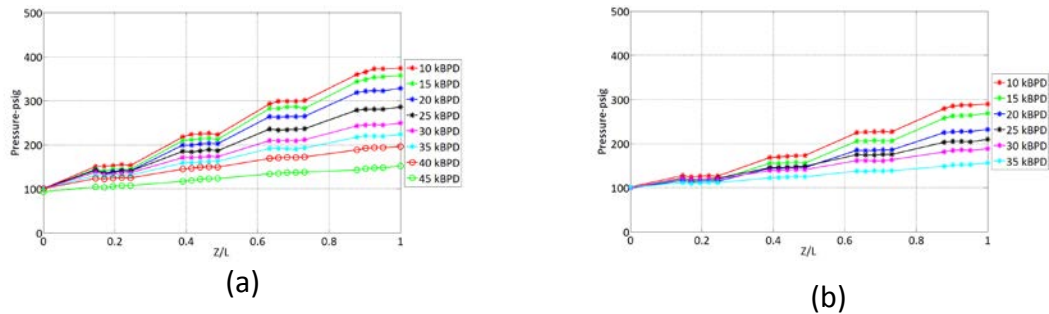


Figure 4-10: Pressure variation in the pump for different liquid flow rates at 100 psig inlet pressure, 3600 RPM (a) 0% GVF (b) 20% GVF

In order to fully understand the diffuser performance, on the 1st stage diffuser static pressure transducers are mounted on the suction, pressure and meridional planes as shown in Figure 3-13. Figure 4-11 shows the variation in the static pressure across three planes for different liquid flow rates at 100 psig inlet pressure and 3600 RPM. In an ideal diffuser, the pressure on the pressure side should be higher than the meridional plane and the meridional plane should be higher than the suction side. Also, the pressure should increase from inlet to outlet of diffuser.

Figure 4-11(a) shows the variation in pressure for 10 kBPD liquid flow rate. For this flow condition the static pressure on the suction plane is higher than the meridonal plane which suggests the existence of strong recirculation zones in the diffuser. Because of recirculation zones the diffuser effective flow area is reduced which increases the velocity of the fluid going into the next stage impeller. Due to this, the efficiency of the pump for this flow condition will be reduced. From the efficiency curve as shown in Figure 4-1(d), for this flow condition the efficiency of the pump is very low.

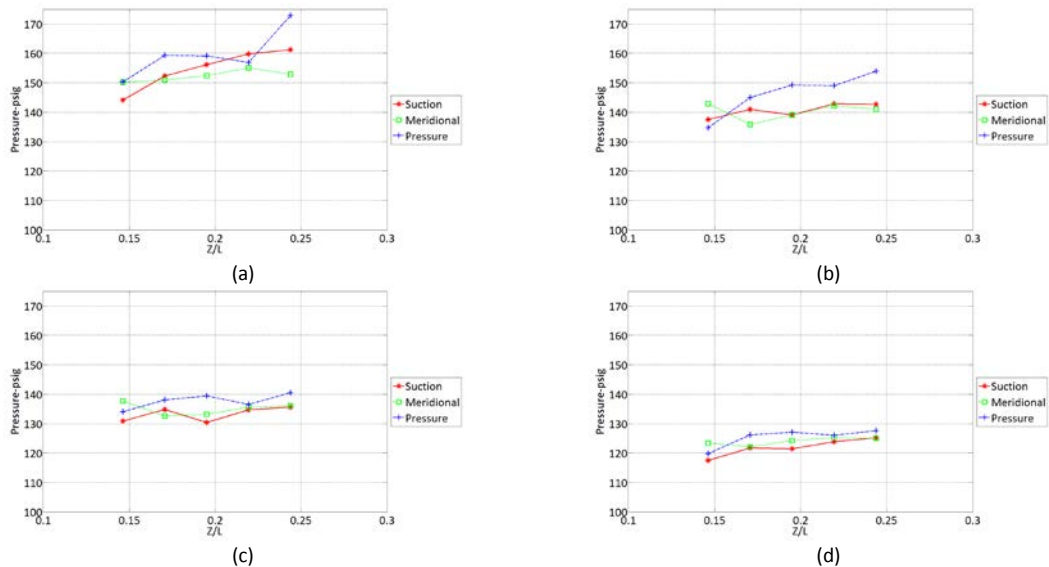


Figure 4-11: Pressure variation in 1st stage diffuser across different planes at 100 psig Inlet pressure, 3600 RPM, 0%GVF (a) 10 kBPD liquid flow rate (b) 20 kBPD liquid flow rate (c) 30 kBPD liquid flow rate (d) 40 kBPD liquid flow rate

Figure 4-11(b), (c) and (d) show the variation in pressure for liquid flow rates of 20, 30 and 40 kBPD. As the flow rate increases, the pressure on the suction plane is less than the meridonal plane. For 40 kBPD liquid flow rate, the pressure on the three

planes is closer to the ideal diffuser. This flow rate is closer to the BEP of the pump as shown in Figure 4-1(d).

4.1.6 Head Ratio

The efficiency of advanced gas handlers (AGH) is low in comparison to standard mixed flow pump because of its gas handling capabilities. For optimum use AGH are installed prior to a standard mixed flow pump in a multi stage pump so the purpose of AGH is to homogenize the flow. Head ratio (Pirouzpanah (2016)) is used to compare the stage by stage performance of similar or different multiphase pumps. It is defined as

$$\text{Head ratio} = \frac{h}{h_{homo}} \quad 4-1$$

Where h is the head obtained from experimental data and h_{homo} is the homogenous head obtained from pure liquid experimental data. Head ratio varies from 0 to 1, where 1 is close to pure liquid condition and zero is when no head is developed.

Figure 4-12(a) shows the stage-1 variation in head ratio versus stage inlet GVF for different liquid flow rates. At low GVF, the head ratio is close to 1 which suggests the flow is homogenous or head loss in compressing air is nullified by the reduced friction in the flow. With increase in GVF the head ratio decreases due to slip between phases which causes accumulation of gas pockets in the flow field. At higher GVF, the head drops by 80% in comparison to the pure liquid case.

Figure 4-12(b), (c) and (d) shows the variation for other stages. At each stage, stage inlet GVF is calculated based on static pressure at the inlet. From stage 1 to 2,

there is a considerable change in the head ratio plot. For stages 2, 3 and 4 the plots are similar, this suggests that much of the mixing happens in the first two stages of the pump. For optimum use, 2 stages of AGH would be sufficient to homogenize the flow.

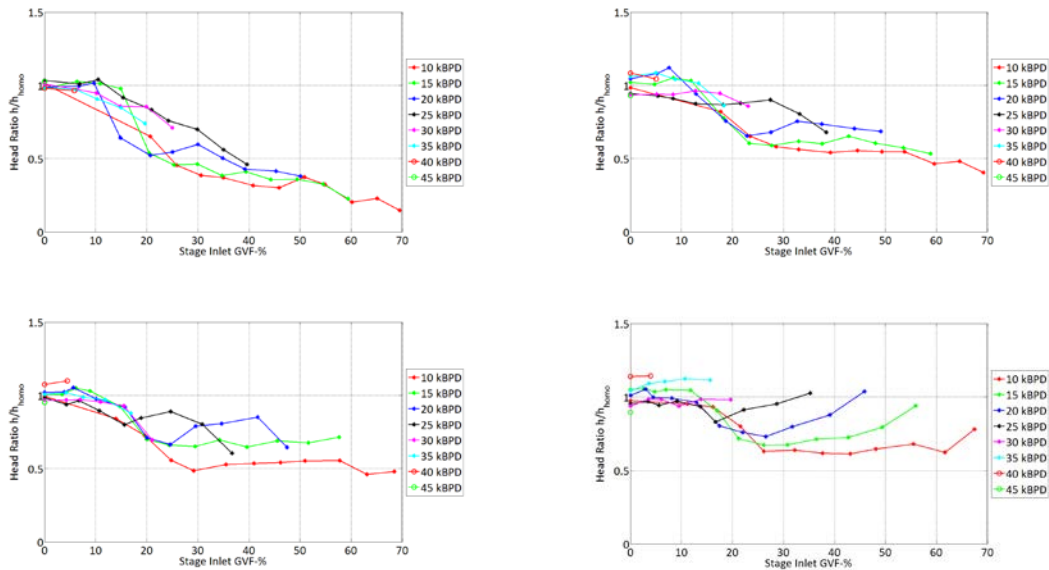


Figure 4-12: Stage by stage head ratio versus stage inlet GVF comparison at 100psig inlet pressure, 3600 RPM (a) 1st stage (b) 2nd stage (c) 3rd stage (d) 4th stage

4.1.7 Empirical Model

Empirical models available in the literature for predicting pump head under two phase flow are developed for radial and mixed flow pumps. The GVF handled by these pumps is limited and these models are pump specific. The current pump is neither a mixed flow nor a radial flow pump. The affinity laws are also not applicable for these pumps. Based on the experimental data for the test matrix shown in Table 3-7, a new empirical model is developed to predict the head developed per each stage under two

phase flow conditions. Equation 4-2 is used to predict the stage head for different flow conditions.

$$h_s = A + (B * Q_l * N) + (C * N^2 * \alpha_i * \rho_{mix}^D) \quad 4-2$$

Where h_s is the stage head in feet, Q_l is liquid flow rate in GPM, N is rotating speed in RPM, α_i is GVF at stage inlet, ρ_{mix} is mixture density in kg/m^3 , A is shut off head which is a function of rotating speed and B, C, D are constants.

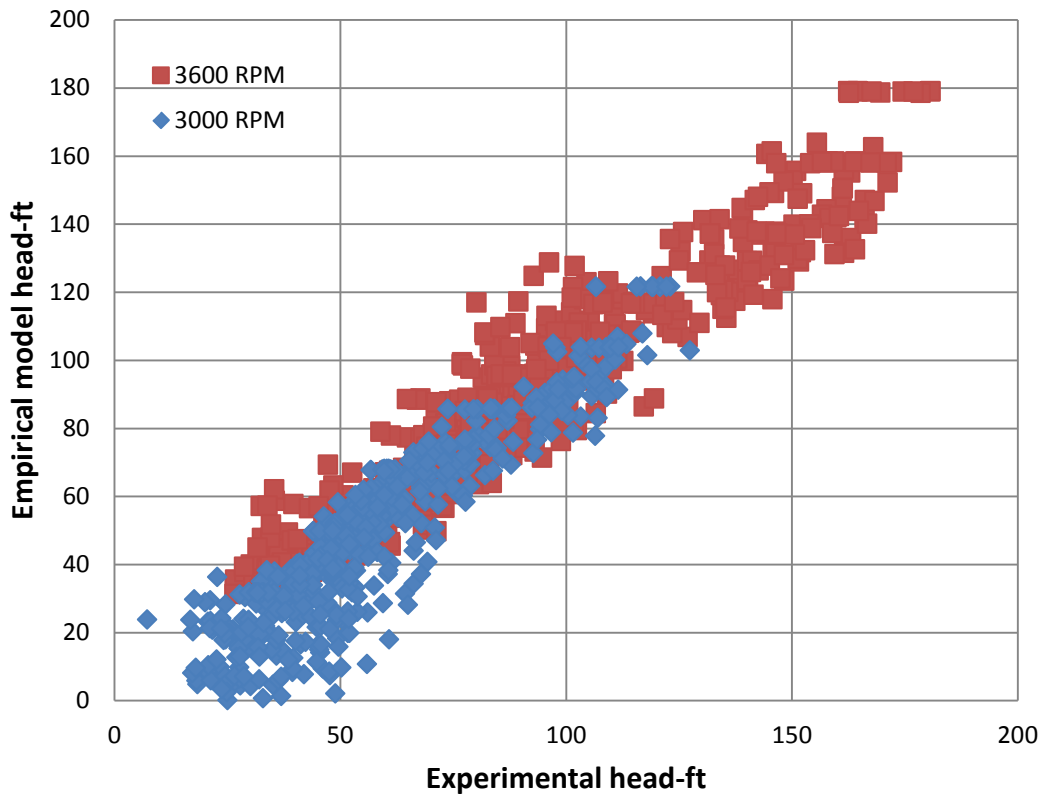


Figure 4-13: Comparison of experimental head and empirical model head for different rotating speeds

While developing the empirical model, the 1st stage is not considered because of entrance effects and non-uniform flow conditions. From the experimental data of

the 2nd, 3rd and 4th stages the constants for equation 4-2 are $A(3000)=155.12$, $A(3600)=220.19$, $B=-3.9472e-5$, $C=-3.4168e-8$ and $D=0.25$. The linear regression for the above equation is 0.94 with a RMSE of 8.95.

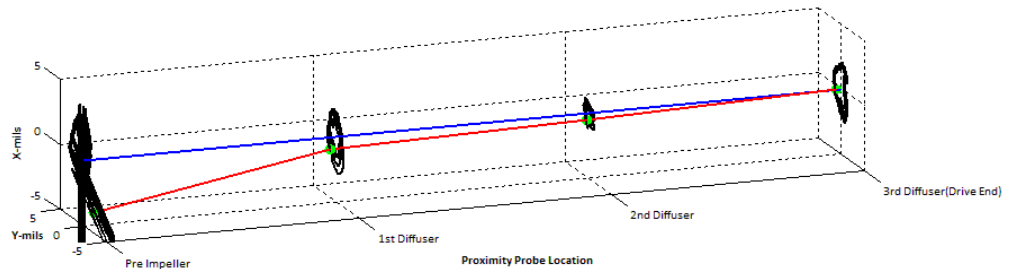
Figure 4-13 shows the comparison of experimental head and empirical model head for different rotating speeds for the 2nd, 3rd and 4th stage of the pump for different flow conditions. There is a considerable spread of points, but this equation will be useful in estimating the head developed by the pump by an operator working in the field with reasonable accuracy.

4.1.8 Vibration Analysis

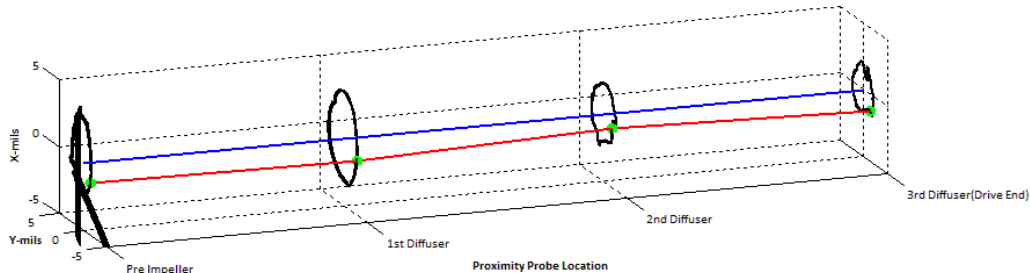
Proximity probes are installed in three diffuser stages and at the inlet of the pump to record the shaft motion for different flow conditions for a uniform bearing clearance. Figure 4-14 shows the orbit plot for the shaft at different bearing locations, for flow conditions of 200 psig inlet pressure, 3600 RPM, 10 kBPD liquid flow rate for different GVF. With increase in GVF the orbits gets bigger because the stiffness of the bearing decreases under presence of gas.

Figure 4-15 shows the variation in peak to peak amplitude at 60 Hz for one proximity probe for different flow conditions at 200 psig inlet pressure and 3600 RPM. From the graph for any flow condition with increase in GVF, the amplitude increases until it reaches the clearance of the bearings. Sixty Hz is chosen since it is the running frequency. Once the amplitude is equal to the clearance of the bearing, rubbing

between the bearing surfaces occurs during which the bearing is not lubricated which is not an optimum condition to operate the pump. Continuous rubbing might cause the bearing to crack and damage the pump since the bearing materials are usually brittle in nature.



(a)



(b)

Figure 4-14: Orbit plots of the shaft for flow conditions of 200psig inlet pressure, 3600 RPM, 10 kBPD liquid flow rate a) 0% GVF b) 70% GVF

The accelerometers installed on the two flanges of the pump don't show the behavior similar to a proximity probe. Figure 4-16 show the peak to peak amplitude at 60 Hz for inlet flange accelerometer along pump spiral axis for flow conditions of 200 psig inlet pressure and 3600 RPM. With increase in flow rate and GVF the amplitude is constant, the reason might be damping due to gas in the flow field even though there is

rubbing in the bearing surfaces and the accelerometer is placed away from the center of the shaft.

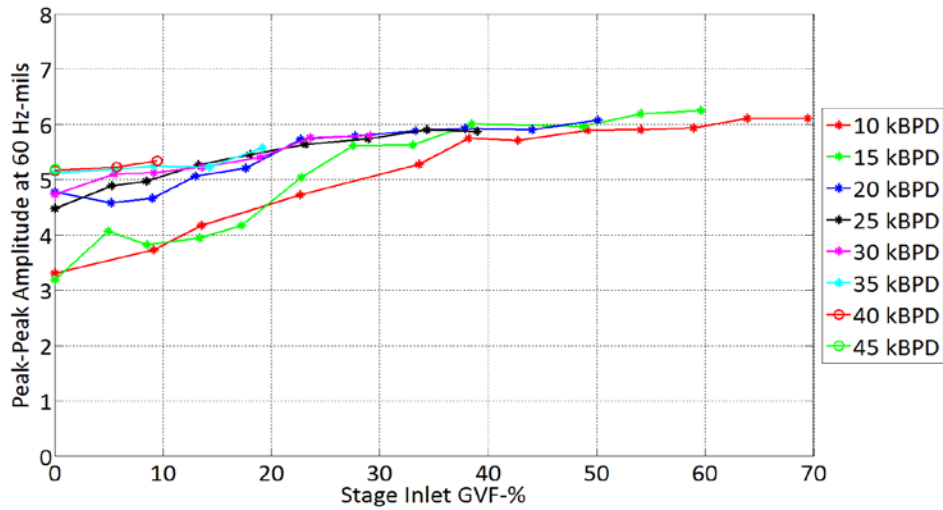


Figure 4-15: Peak to peak amplitude of the shaft at 60 Hz for 1st stage diffuser X-direction proximity probe at 200 psig inlet pressure and 3600 RPM.

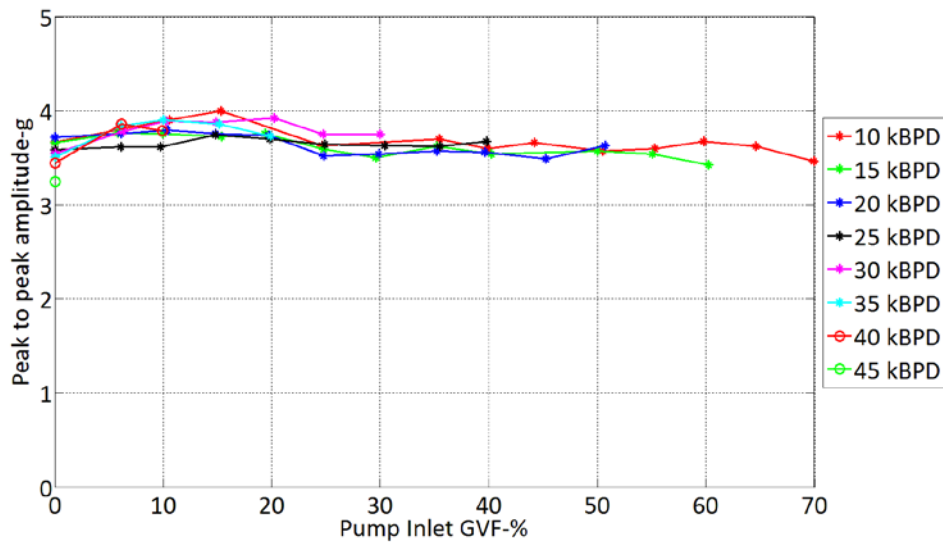


Figure 4-16: Peak to peak amplitude at 60 Hz for inlet flange spiral axis accelerometer data at 200 psig inlet pressure and 3600 RPM

4.2 Flow Visualization

In this section results of flow visualization carried out on the single stage helico-axial pump are discussed.

4.2.1 Pump Performance

Since the pump is made of plastic material, the test matrix is different than the 4-stage pump. Figure 4-17 shows the head versus total flow rate curves of the single stage pump at 50 psig inlet pressure and 1800 RPM for different GVF. Similar to the 4-stage pump, with minimal amount of air, the head rise in the pump increases. Further increase of air reduces the head in the pump due to increase of losses in the system.

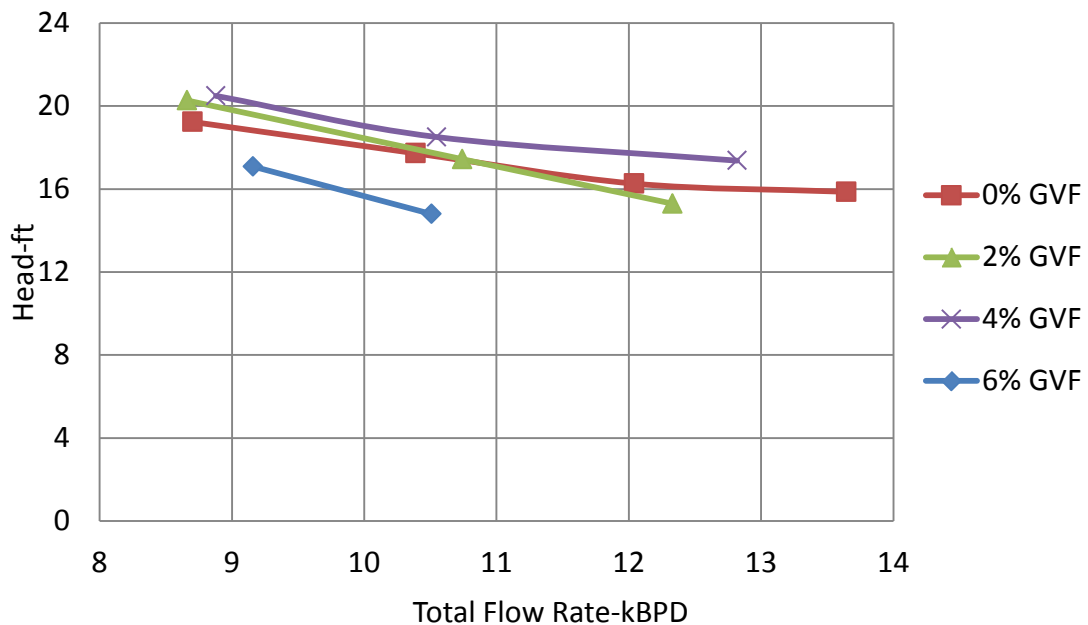


Figure 4-17: Performance map of the single stage pump at 50 psig inlet pressure, 1800 RPM

4.2.2 Bubble Diameter

Video imaging is used for measurement of bubble diameter in the two phase flow under study. For ideal measurement of bubble diameter, the projection method should be used where light source is placed behind the system and the camera in the front of the system.

In the present system, because of pump shaft, considerable thickness of the plastic material and process fluid, projection method is not applicable since the light intensity is not sufficient for high speed imaging.

For extremely low GVF (trace amount of air) measurements the light source was placed on the side so that intensity lost from reflection and refraction is minimized. A schematic of the arrangement is shown in Figure 4-18, with Z-axis being axis of the shaft.

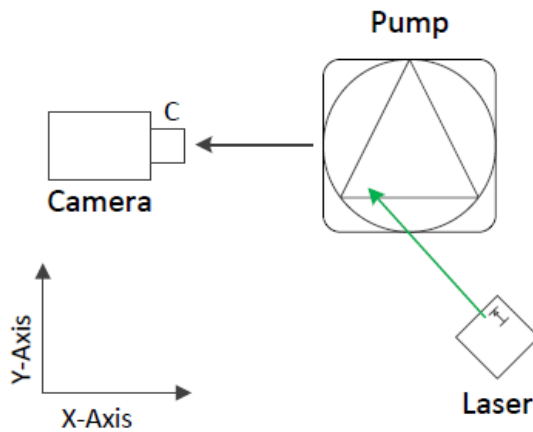


Figure 4-18: Schematic of the laser and camera

Using the above setup, flow visualization is carried for different liquid flowrates with trace amount of air. Figure 4-19(a) shows the captured image in the impeller flow domain at 8.7 kBPD liquid flow rate, 50 psig inlet pressure and 1800 RPM. In this figure black spots represent the bubbles, since bubbles are illuminated from the side with camera in the front, the shadow of the bubbles is recorded in the camera. The above image is processed further into a binary format so that the bubble diameter can be measured using INSIGHT 4G software (Size-Shape-Analysis Module). A sample of the processed image is shown in Figure 4-19(b).

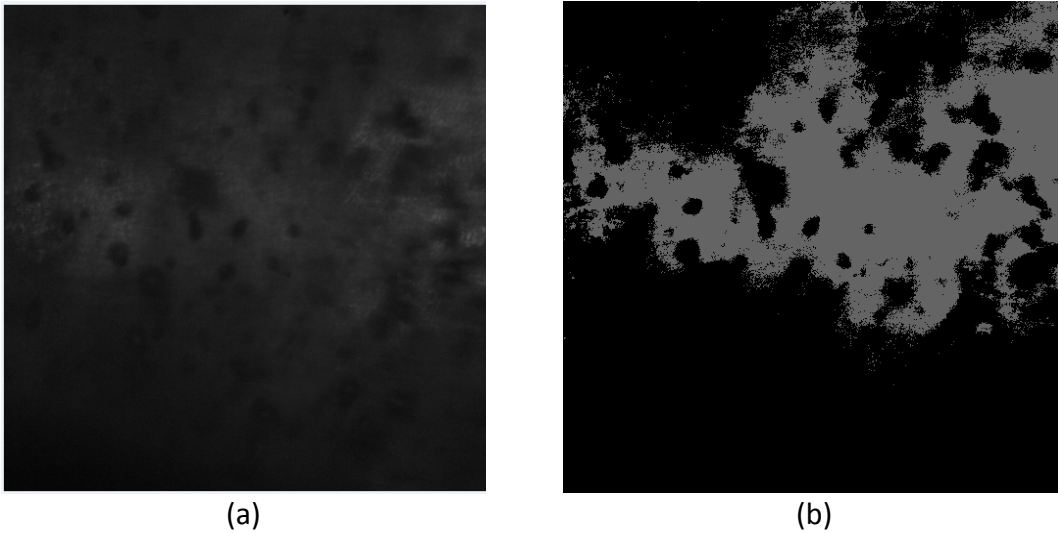


Figure 4-19: a. Captured image b Processed Image of impeller at 8.7 kBPD liquid flow rate, 50 psig inlet pressure and 1800 RPM

A continuous set of processed images are used in measuring bubble diameter and bubble velocity. Figure 4-20 shows the output from the INSIGHT 4G module. Figure 4-20(a) shows the histogram of the bubble diameter for the set of images which are analyzed. Figure 4-20(b) shows the average bubble diameter for the different images.

Based on two consecutive images the bubble velocity is calculated. Figure 4-20(c) shows the histogram of the bubble velocity and Figure 4-20(d) shows the average bubble velocity for different frames.

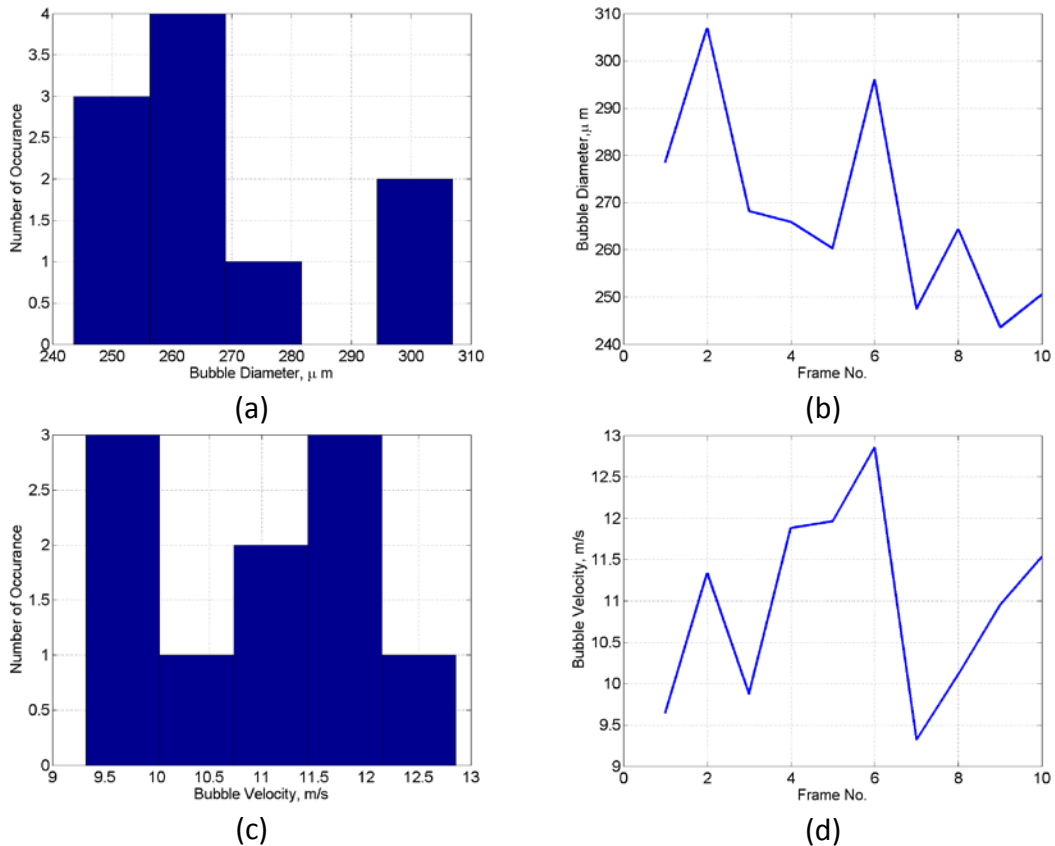


Figure 4-20: Output of processed Images from INSIGHT 4G software for flow conditions of 1800 RPM, 50psig inlet pressure and 8.7 kBPD liquid flow rate a. Bubble diameter histogram b. Average bubble diameter per frame c. Bubble velocity histogram d. Average bubble velocity per frame

Using the above method bubble diameter measurement was possible for trace amounts of air. Even with slight increase of GVF to 2%, bubbles tend to be closer and their existence in the flow is not planar. Due to this, the light emitted from the laser is not transmitted to the viewing plane and it is either reflected or refracted. To

overcome this problem for $GVF \geq 2\%$ flow bubble diameter measurements are measured in the tip clearance of the impeller where the leakage flow occurs from pressure side to suction side of the blade. Since the measurements are carried out in the tip clearance, bubbles are fewer in number. For measuring the bubble diameter in the tip clearance, the laser is directed on the impeller blade tip and the reflected light wave from the tip is sufficient to illuminate the clearance flow field. A schematic of the setup is shown in Figure 4-21.

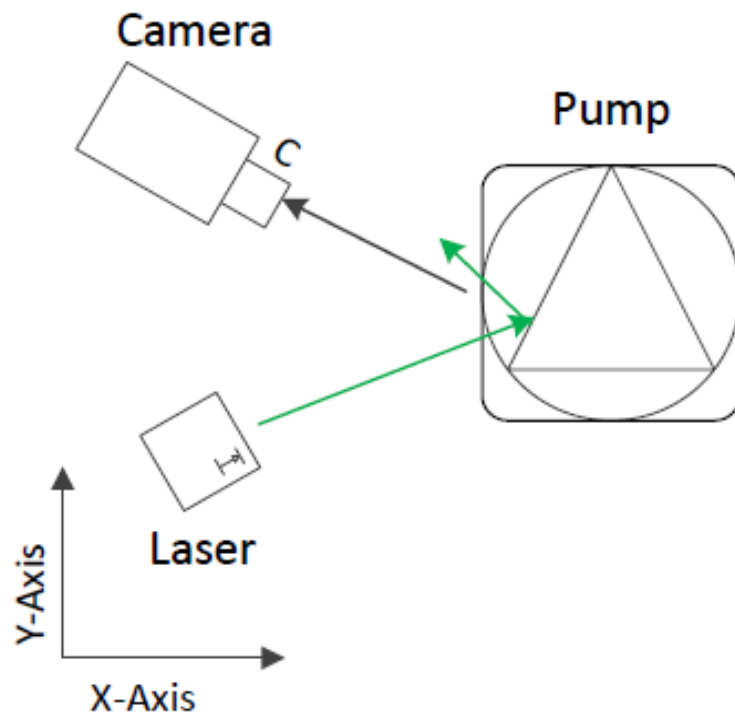


Figure 4-21: Schematic of the laser and camera for high GVF flow

Figure 4-22 shows the captured image at 8.7 kBPD liquid flow rate, 6% GVF, 50 psig inlet pressure and 1800 RPM. The black dots in the image represent the bubbles.

Since the bubbles are fewer in number in comparison with Figure 4-19, INSIGHT 4G software cannot be used to measure bubble parameters. The bubble diameter is obtained by measuring the length of the major and minor axes of each bubble individually and then averaging across 10 different frames. The equivalent diameter of the bubble is obtained using the equation

$$d_e = \frac{\pi ab^2}{\frac{\pi b^2}{2} + \frac{\pi}{2} \frac{ab}{\sqrt{1 - \frac{b^2}{a^2}}} \sin^{-1} \left(\sqrt{1 - \frac{b^2}{a^2}} \right)} \quad 4-3$$

Where a is the major axis length, b is the minor axis length



Figure 4-22: Captured image in Impeller at 8.7 kBPD liquid flow rate, 6% GVF, 50 psig inlet pressure and 1800 RPM

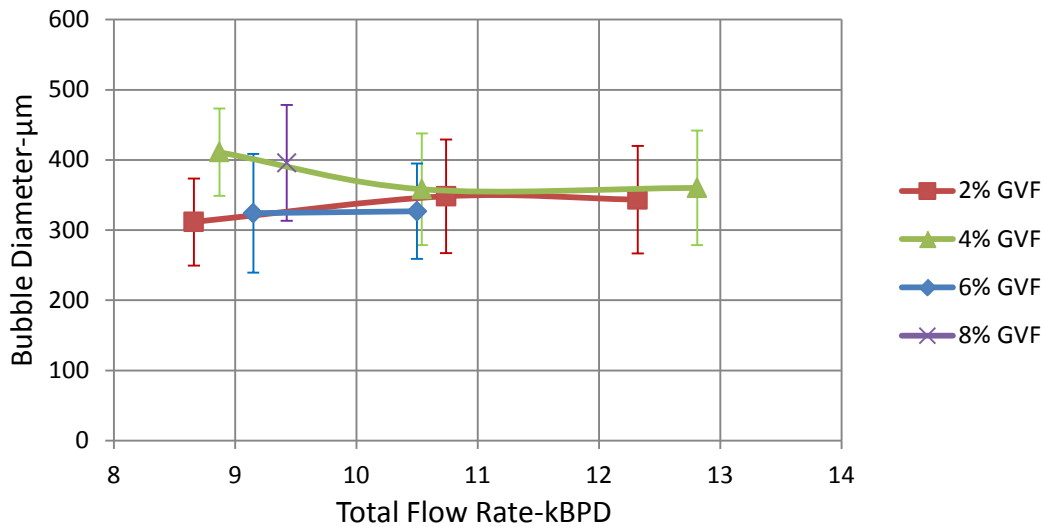


Figure 4-23: Variation of bubble diameter versus total flowrate at 50 psig inlet pressure, 1800 RPM

Figure 4-23 shows the variation of bubble diameter versus total flowrate for different GVF at 50 psig inlet pressure, 1800 RPM. Since the test matrix size is small, clear trends with increasing GVF and flowrate are not observed. In general the average bubble diameter for different flow conditions is around 350 µm with a standard deviation of 75µm.

4.2.3 Bulk Flow Visualization

Bulk flow visualization is carried out on the impeller and diffuser to detect the flow irregularities as the two phase flow traverses through the pump. Flow visualization is carried out using a high speed camera, halogen lamp is used for illuminating the flow field. A picture of the arrangement is shown in Figure 4-24.

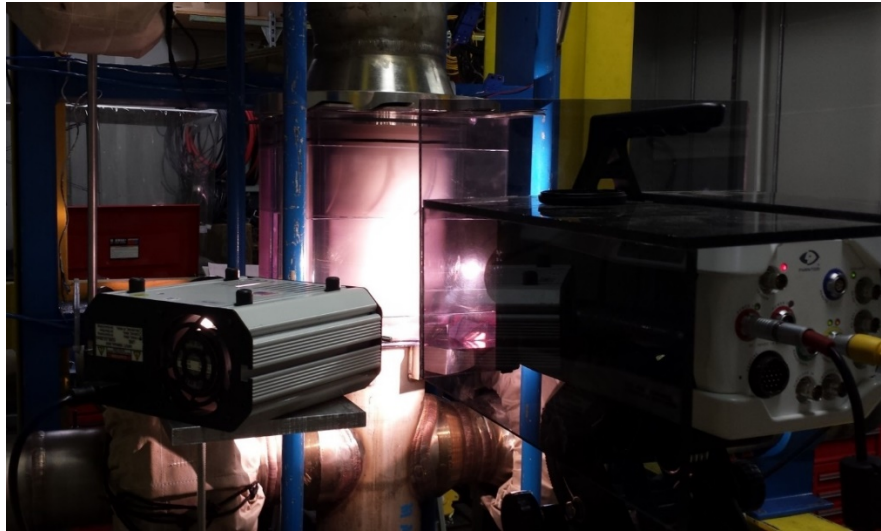


Figure 4-24: Picture and halogen lamp and camera

4.2.3.1 Impeller Bulk Flow

The impeller flow field is visualized for the test matrix shown in Table 3-8. The resolution of the image is 1024 x 512 pixels, captured with a sampling rate of 14000 fps and an exposure time of 71.43 μ s. Since the impeller behavior is partly axial and partly centrifugal, a considerable amount of air leakage is observed from the tip clearance even with centrifugal forces pushing water radially outwards. From the flow conditions evaluated, the bulk flow does not have any major separation zones or air accumulation as flow passes through the impeller.

Figure 4-25 and Figure 4-26 shows the bulk flow field in the impeller for two different air flow conditions, 2% GVF and 8% GVF, other parameters were 1800 RPM, 50 psig inlet pressure and 8.7 kBPD liquid flow rate. For 8% GVF considerable leakage of air is observed from the impeller blade in comparison with 2% GVF.

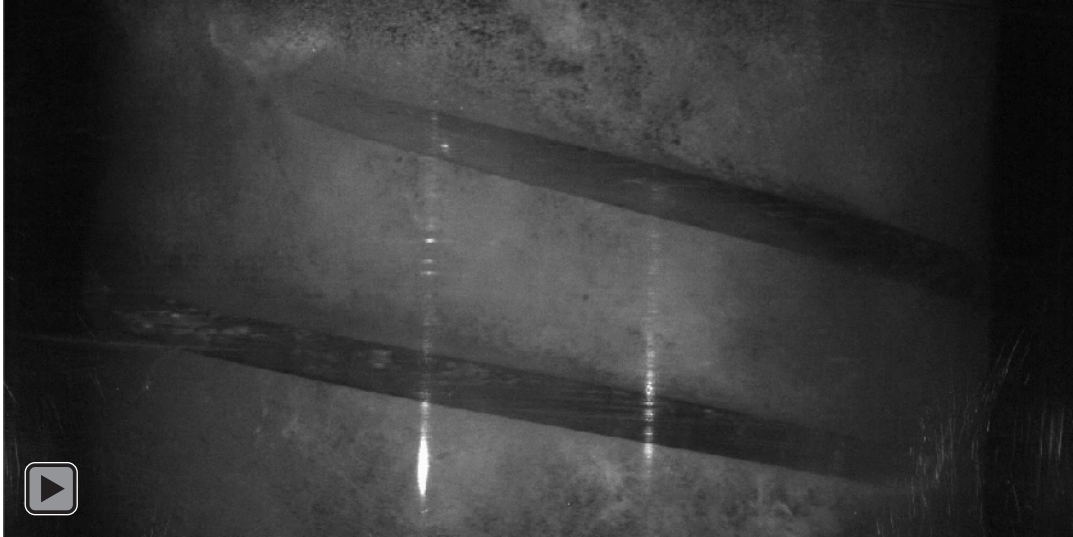


Figure 4-25: Video of the impeller flow field at 1800 RPM, 50 psig inlet pressure, 8.7 kBPD liquid flow rate and 2% GVF

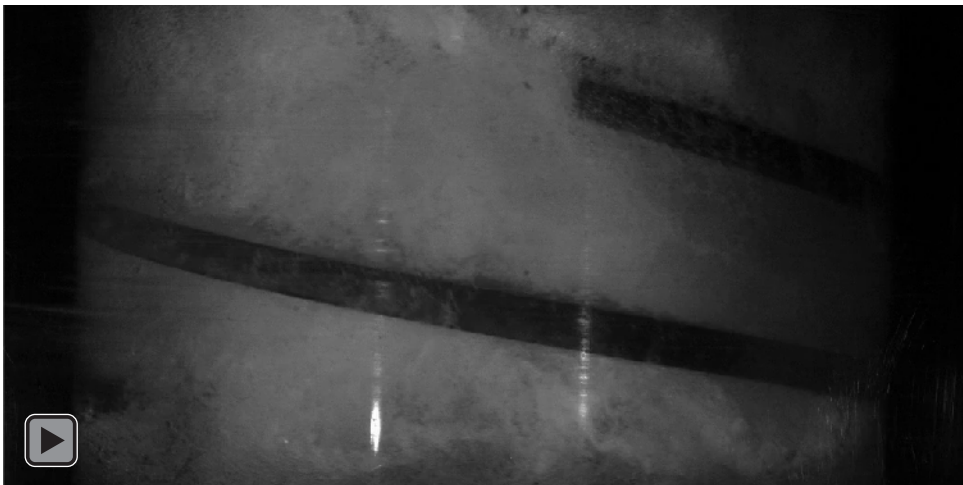


Figure 4-26: Video of the impeller flow field at 1800 RPM, 50 psig inlet pressure, 8.7 kBPD liquid flow rate and 8% GVF

4.2.3.2 Diffuser Bulk Flow

Similar to the impeller, the bulk flow in the diffuser is visualized for different flow conditions with the same image parameters and camera settings. At the inlet to the diffuser the flow is aligned with the diffuser blade. As the flow traverses through the diffuser, a recirculation zone is observed on the suction side of the blade. The recirculation zone is due to back flow at the outlet of the diffuser. The back flow is due to fluid flow from pressure side to suction side of the blade, a schematic of the fluid flow in shown in Figure 4-27.

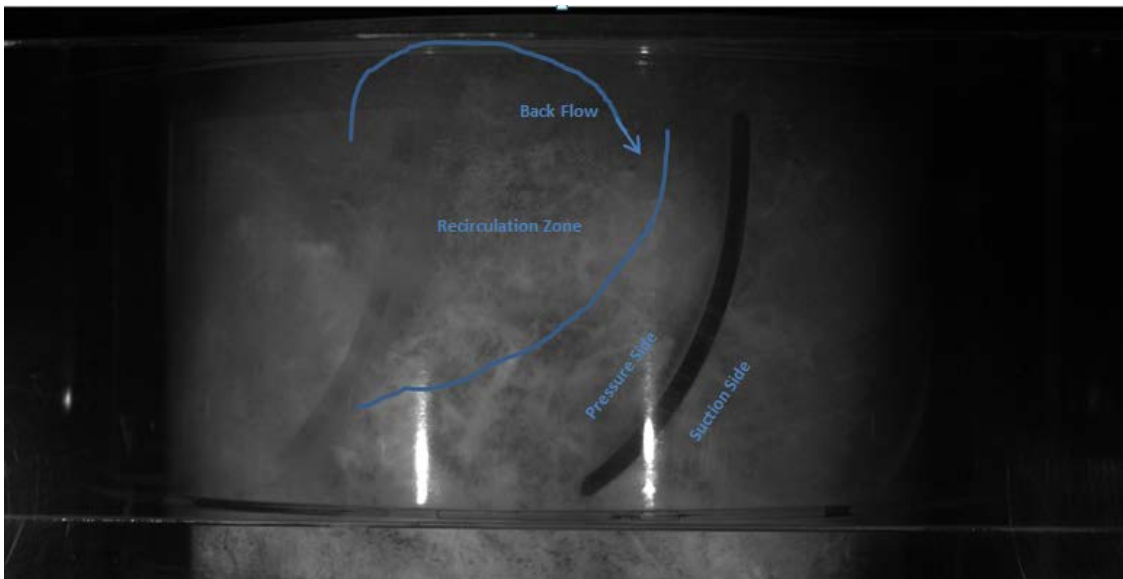


Figure 4-27: Schematic of the flow



Figure 4-28: Video of the diffuser flow field at 1800 RPM, 50 psig inlet pressure, 8.7 kBPD liquid flow rate and 2% GVF

The back flow occupies more than 50% of the diffuser flow area and it varies based on flow conditions. With increase in flow rate, the occupied area reduces because of reduced intensity of recirculation zone or pressure difference across both sides of the blade. Figure 4-28 and Figure 4-29 show the videos of bulk flow field in the diffuser for two different liquid flow rates, 8.7 kBPD and 12 kBPD, other parameters were 1800 RPM, 50 psig inlet pressure and 2% GVF.



Figure 4-29: Video of the diffuser flow field at 1800 RPM, 50 psig inlet pressure, 12 kBPD liquid flow rate and 2% GVF

4.3 Simulation Results

In this section stage by stage, single phase and two phase transient numerical simulation results for the first two stages of the pump are discussed. The first stage is simulated to study the inlet flow effects on the performance of the pump, second stage to study the multi stage performance. Water and air were used as process fluids

4.3.1 Grid Independence Study

Flow field calculations are performed for the flow path shown in Figure 3-19. Three different models are chosen for evaluating the grid independence study, the details are shown in Table 4-1. Hexahedral elements are used to mesh the impeller and

diffuser fluid domain. In these models, the number of elements and first layer height in the boundary layer are varied.

Model	No of Elements(Million)
Model-1	5.52
Model-2	4.64
Model-3	2.96

Table 4-1: Mesh sizes for different Models

Figure 4-30 shows the effect of grid size on percentage change in pressure rise at 30 kBPD liquid flow rate and 3600 RPM using water as process fluid. From the figure the maximum variation in dP is 3% with reduced mesh size. Since the model needs to be evaluated for different flow conditions, Model-2 with 4.64 million elements is used for further calculations.

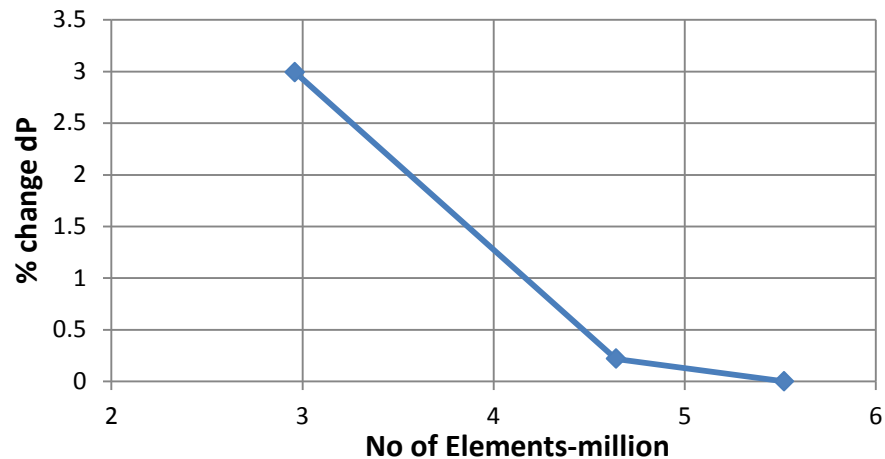


Figure 4-30: Effect of Number of elements Vs Percentage change in dP for flow conditions of 30 kBPD liquid flow rate and 3600 RPM

4.3.2 Single Phase Simulations

For the single phase simulations, water is used as the process fluid. The Reynolds averaged Navier Stokes equations coupled with the Realizable k- ϵ model for turbulent closure were used for solving the flow field. Since there is no considerable change in the fluid temperature, the energy equation is not solved. Momentum, k and ϵ equations are discretized using a 1st order upwind scheme, gradients using least squares cell based scheme. Since the equations are marching with time, first order implicit scheme is used for discretizing time step. The SIMPLE algorithm is used to solve the equations. The under relaxation factors are pressure =0.3, body forces = 0.7 and momentum=0.4, for turbulent kinetic energy, dissipation rate and viscosity it is equal to 0.6. A time step size of 0.5 degree is used with a maximum of 80 iterations per time step. Convergence criterion of 1E-4 is used for all the residuals.

Figure 4-31 shows the comparison of experimental and simulation results for the 1st stage pump. Calculations are performed for flow rates ranging from 15 to 40 kBPD at a running speed of 3600 RPM. The maximum difference in performance is less than 10%, with an absolute pressure difference of 3.6 psi. The error bars on the experimental data indicate the standard deviation of the measured data. Even with constant mass flow rate at the inlet, because of interaction between the stator and rotor, the pressure rise across the single stage for every time step is not constant. Figure 4-32 shows the variation in pressure rise for different time steps at 35 kBPD

liquid flow rate and 3600 RPM. The error bars on the simulation curve indicate the standard deviation of the calculated transient data.

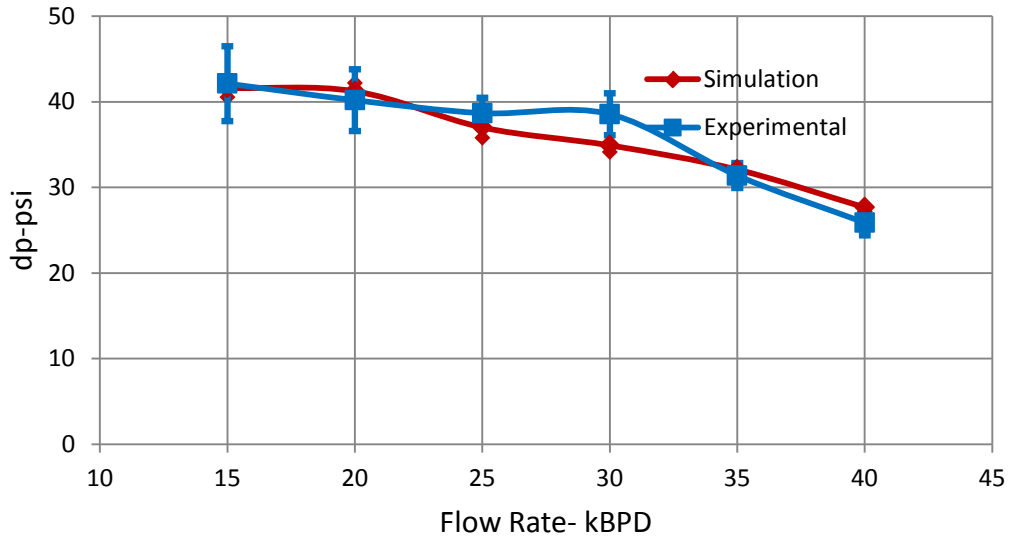


Figure 4-31: Performance comparison of simulation and experimental results for 1st stage

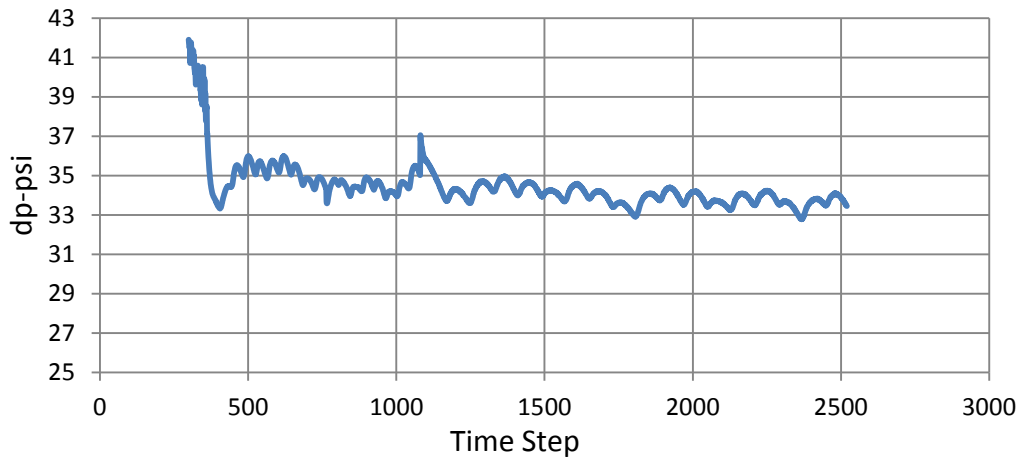


Figure 4-32: Pressure rise versus time step at 35 kBPD liquid flow rate, 3600 RPM

For simulating the second stage performance, two different boundary conditions are evaluated. Figure 4-33 shows the pressure gradient comparison between experimental data and simulations for different liquid flow rates at 3600 RPM using a periodic boundary condition. The pressure gradient calculated from the simulations is higher than the measured data since secondary flow paths are not considered in the fluid model. From the data, the maximum difference between measurements and simulation is less than 15%. If the standard deviation of the experimental and simulation data is accounted for, the difference is considerably reduced.

Figure 4-34 shows the performance comparison for 2nd stage using velocity inlet and pressure outlet as boundary conditions. In this set up Diffuser1-Impeller2-Diffuser2 combination has been simulated. Velocity inlet boundary condition at diffuser1 inlet is obtained from first stage simulation for different flow rates. The dp plotted in Figure 4-34 is the pressure rise across Impeller2-Diffuser2. From the graph the maximum deviation between experimental data and simulation data is less than 14% with an absolute pressure difference of 6.8 psi. The deviation in the 1st stage is lesser due to lower pressure rise which reduces the back flow from the secondary flow path.

From the second stage simulation results shown in Figure 4-33 and Figure 4-34, the pressure rise across the pump calculated using two different boundary conditions doesn't show any difference. Since periodic boundary conditions cannot be used for multi-phase flows, other boundary condition will be used for calculating the flow field.

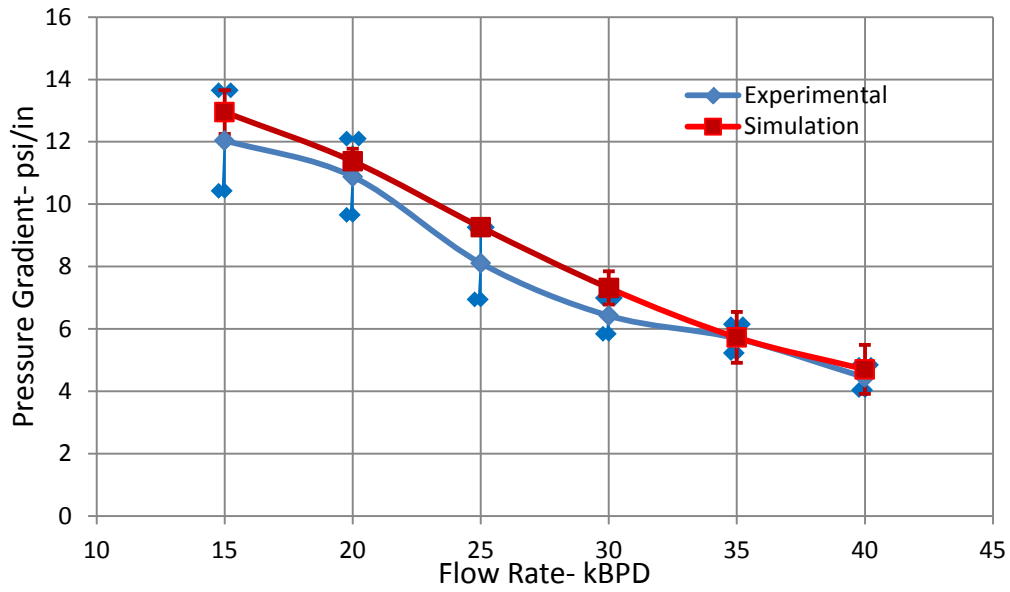


Figure 4-33: Performance comparison of simulation and experimental results for 2nd stage using periodic boundary conditions

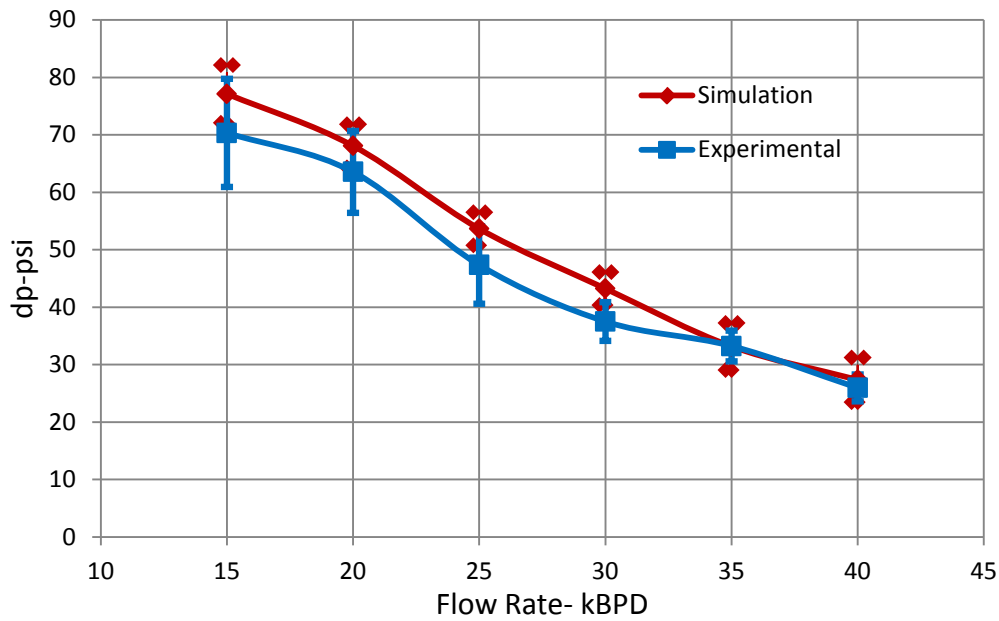


Figure 4-34: Performance comparison of simulation and experimental results for 2nd stage using velocity inlet and pressure outlet as boundary condition

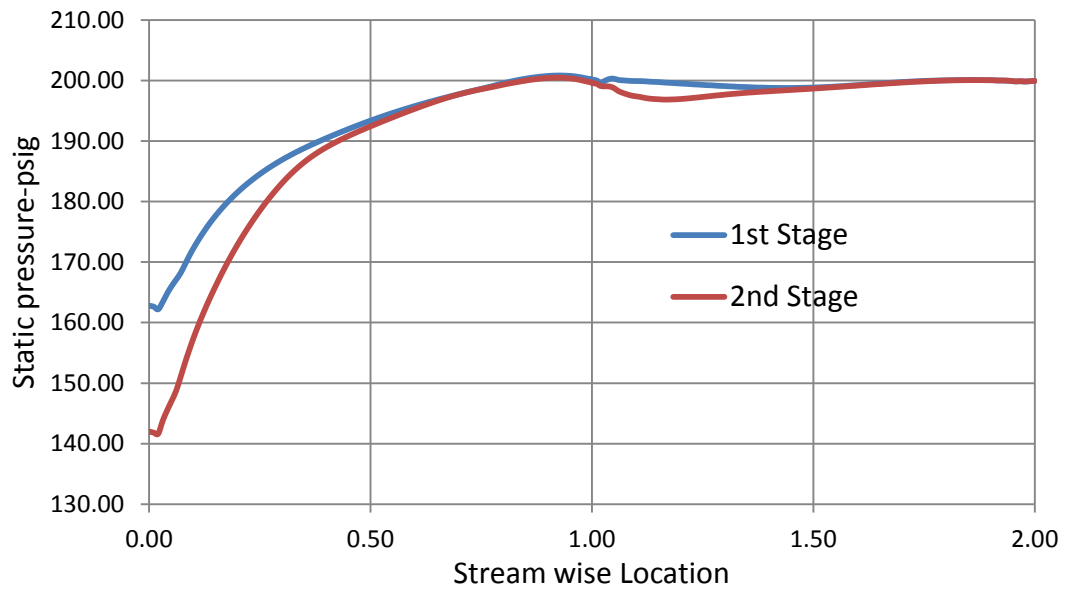


Figure 4-35: Static pressure variation along the stream wise location in a single stage pump for the flow conditions of 25 kBDP liquid flow rate, 3600 RPM

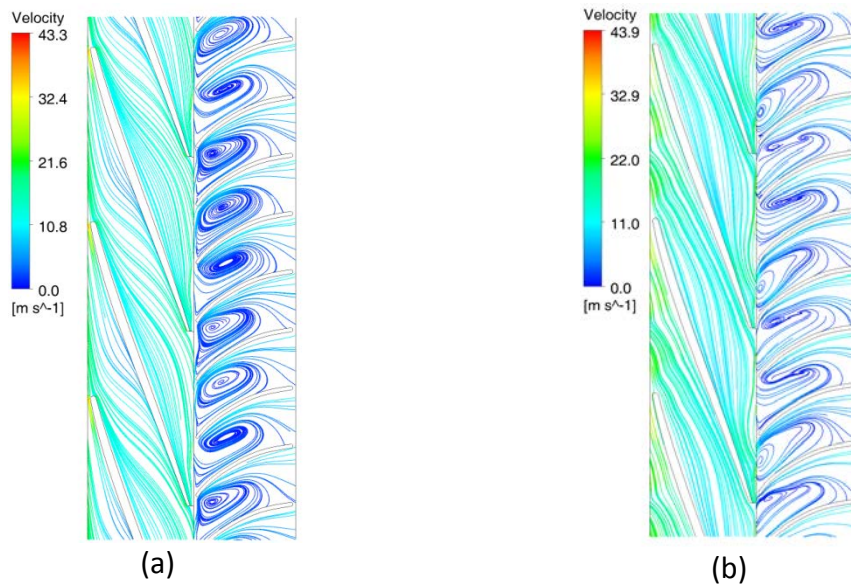


Figure 4-36: Stream lines for the flow conditions of 25 kBDP liquid flow rate, 3600 RPM at span=0.1 (a) 1st Stage (b) Second Stage

Figure 4-35 shows the comparison of static pressure variation along the stream wise location in a single stage pump. The comparison is between 1st and 2nd stage for flow conditions of 25 kBPD liquid flow rate and 3600 RPM. From the figure the pressure rise in the second stage is higher due to inlet flow effects which is shown in Figure 4-35

Figure 4-36 shows the streamlines of stage 1 and stage 2 at a span of 0.1 for the flow conditions of 25 kBPD liquid flowrate, 3600 RPM. A span of 0 represents hub, 1 represents shroud. From the figure for the 1st stage at the impeller inlet, the stream lines are directed toward the pressure side of the impeller blade, as the flow traverses the stream lines don't follow the impeller blade profile this is due to no flow conditioning at the first stage inlet. For the second stage from Figure 4-36(b), the stream lines at the impeller inlet are oriented along the blade profile and they follow the blade profile as flow is traversed in the impeller this is due to first stage diffuser which acts as guide vane for the second stage inlet.

Figure 4-37 shows the variation of static pressure on different sides of the impeller blade for flow conditions of 25 kBPD liquid flow rate, 3600 RPM at span = 0.98. From the graph the circumferential variation of pressure exists because of the effect of Coriolis acceleration in the impeller. The pressure gradient is higher at the inlet and it reduces as the flow exits the impeller.

Figure 4-38 shows the velocity vectors at stream wise locations of 0.13 and 0.65 in the impeller, for flow conditions of 25 kBPD liquid flow rate and 3600 RPM. In this figure, the inlet is at the bottom and the outlet is at the top. Figure 4-38(a) shows the

velocity vectors at stream wise location of 0.13, in the central flow domain vectors are oriented along the blade direction. For the flow closer to the shroud or tip the velocity vectors are pointed in the direction countering the main flow and also along circumferential direction. Vectors countering the main flow are occurring due to pressure variation on suction and pressure side of the impeller blade as shown in Figure 4-37. Figure 4-38(b) shows the velocity vectors at stream wise location of 0.65, at this condition the vectors opposing the main flow are fewer in number because of reduced pressure difference between pressure and suction side of the blade.

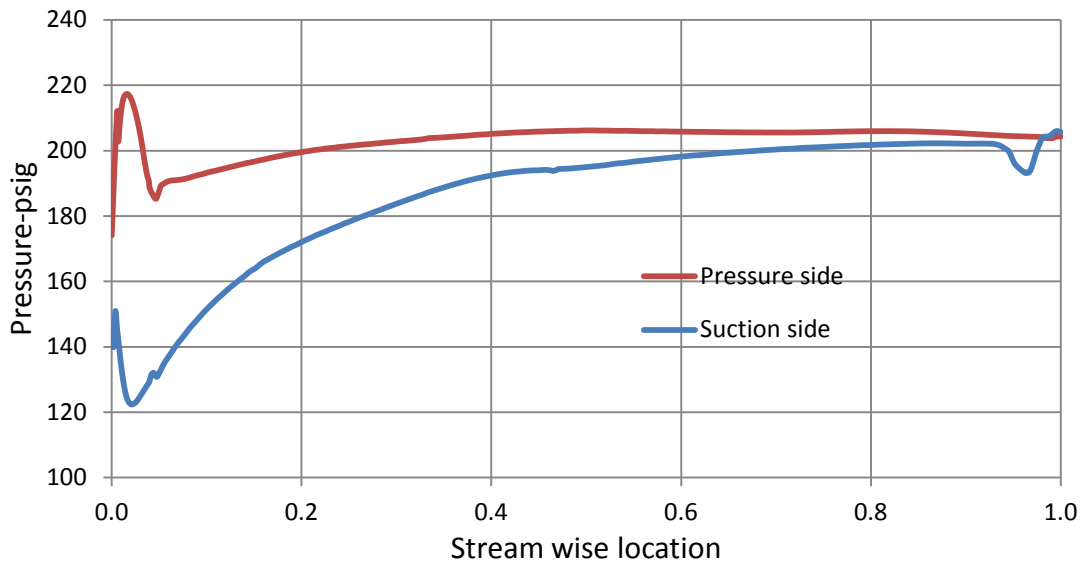


Figure 4-37: Pressure variation on 1st stage impeller blade for flow conditions of 25 kBPD liquid flow rate, 3600 RPM at span = 0.98

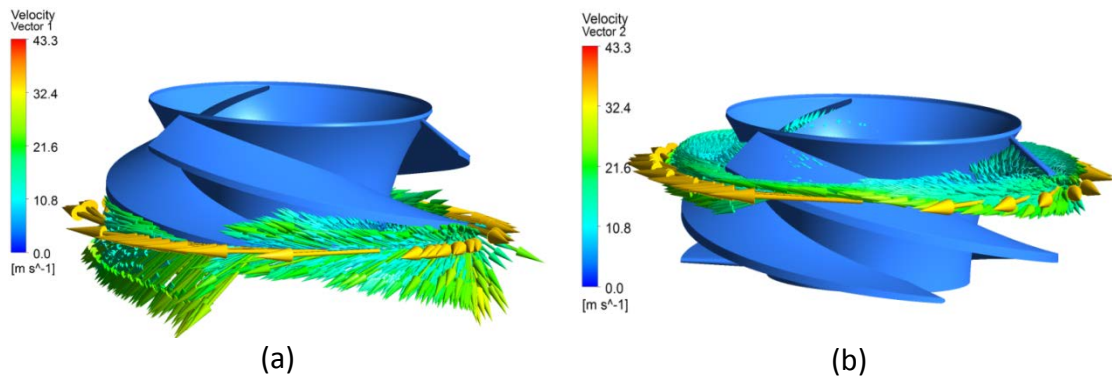


Figure 4-38: Velocity vectors at different stream wise locations for flow conditions of 25 kBPD liquid flow rate, 3600 RPM. (a) 0.13 stream wise location (b) 0.65 stream wise location

Figure 4-39 and Figure 4-40 shows the stream lines for the 2nd stage fluid domain for flow conditions of 15 kBPD and 35 kBPD liquid flow rate and 3600 RPM, obtained using the periodic boundary conditions. The BEP of the pump is 35 kBPD. In the fluid domain, the shroud diameter is constant and hub diameter changes from inlet to outlet in both impeller and diffuser. From Figure 4-40, for span = 0.9 the flow is aligned with the blade direction and it changes with decrease in span. Strong recirculation zones are observed in the diffuser near the hub region (span = 0.1) due to the sudden change in flow direction. The recirculation zone in the diffuser doesn't affect the flow in the impeller for different spans.

Similar behavior is not observed for the 15 kBPD liquid flow rate in Figure 4-39. For span = 0.1, the recirculation zone in the diffuser occurs near the inlet of the diffuser which affects the flow coming out from the impeller. For span = 0.9 near the outlet of diffuser, the flow is not uniform due to the next stage effects. The stream lines in the

impeller are not aligned in the blade direction because of variation in angle of incidence at lower flow rates. Due to this the efficiency at 15 kBPD, is less than 45 kBPD.

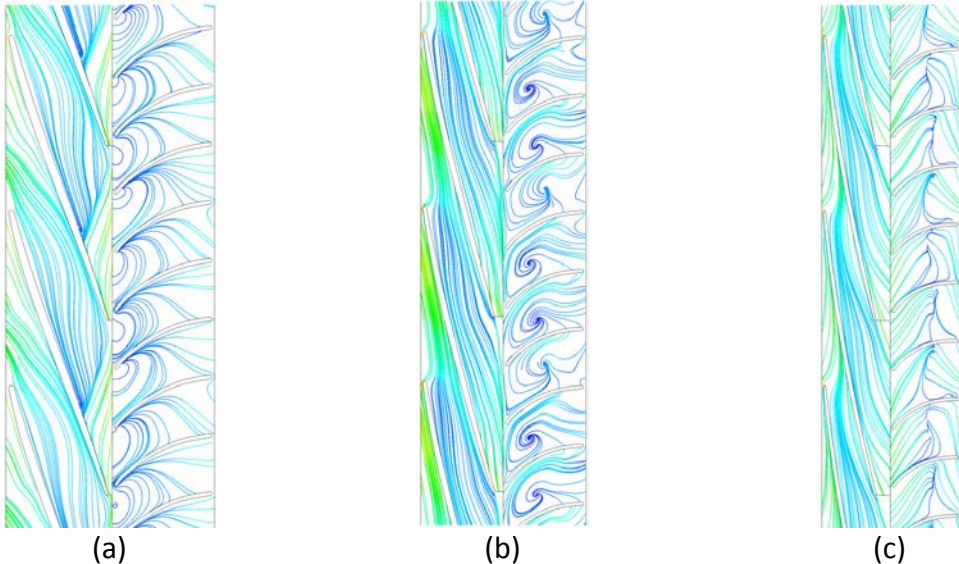


Figure 4-39: Stream lines of the 2nd Stage fluid domain for flow conditions of 15 kBPD liquid flow rate, 3600 RPM using Periodic Boundary Conditions (a) span = 0.1 (b) span = 0.5 (c) span = 0.9

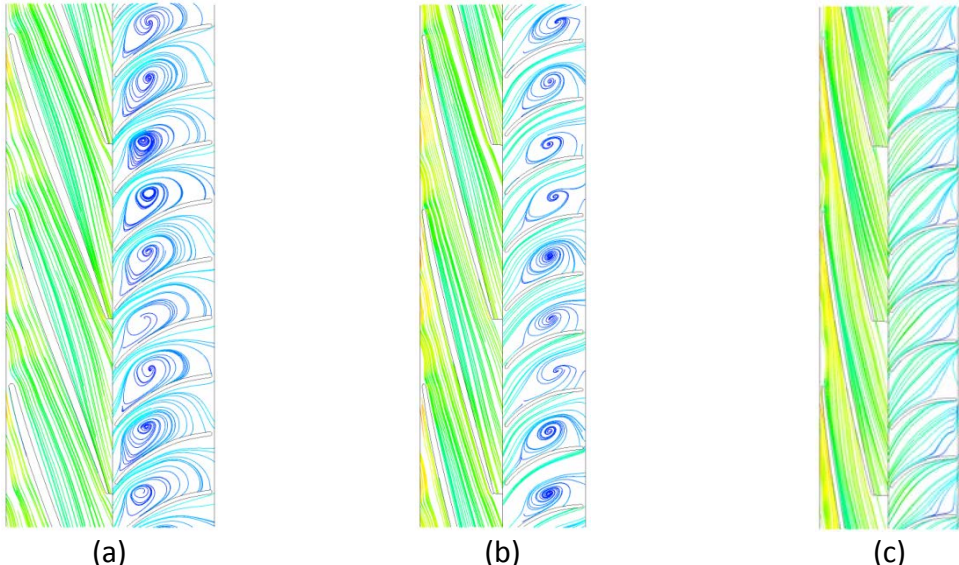


Figure 4-40: Stream lines of the 2nd stage fluid domain for flow conditions of 35 kBPD liquid flow rate, 3600 RPM using periodic boundary conditions (a) span = 0.1 (b) span = 0.5 (c) span = 0.9

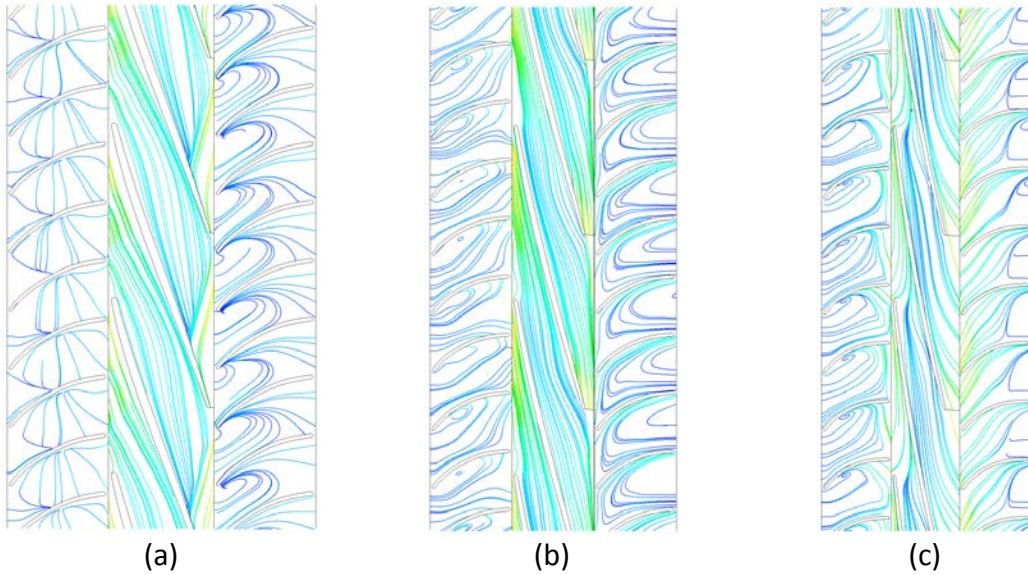


Figure 4-41: Stream lines of the 2nd stage fluid domain for flow conditions of 15 kBD liquid flow rate, 3600 RPM using velocity inlet and pressure outlet as boundary condition (a) span = 0.1 (b) span = 0.5 (c) span = 0.9

Figure 4-41 and Figure 4-42 shows the stream lines for the 2nd stage fluid domain for flow conditions of 15 kBD and 35 kBD liquid flow rate at 3600 RPM, obtained using velocity inlet and pressure outlet as boundary condition. Similar behavior as discussed for Figure 4-39 and Figure 4-40 is noticed expect for outflow effect near the 2nd stage diffuser outlet for 15 kBD liquid flow rate at span = 0.1(Figure 4-41 (c)). This is due to constant pressure at the outlet of the 2nd stage diffuser.

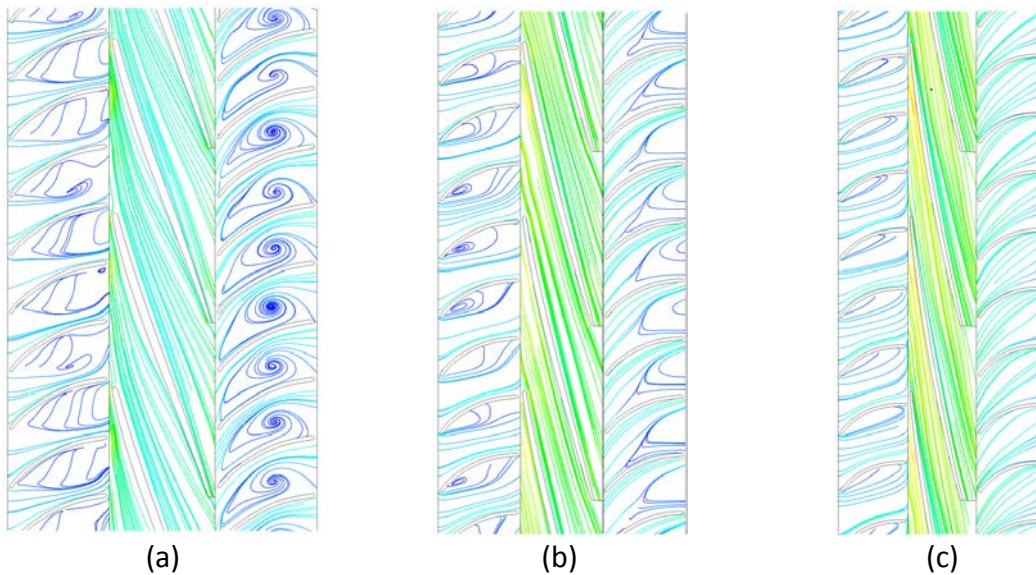


Figure 4-42: Stream lines of the 2nd stage fluid domain for flow conditions of 35 kBP liquid flow rate, 3600 RPM using velocity inlet and pressure outlet as boundary condition (a) span = 0.1 (b) span = 0.5 (c) span = 0.9

4.3.3 Two Phase Simulations

Two phase transient simulations are carried out using water and air as the process fluids for the flow domain shown in Figure 3-21. Since air is of lower density and is a compressible fluid, it significantly affects the performance of the pump. The Reynolds averaged Navier Stokes equations coupled with the Realizable k- ϵ model for turbulent closure were used for solving the flow field. Per phase turbulence model has been used due to the difference in density between two process fluids. Since air is compressible in nature, its density changes as the flow traverses through the pump. The ideal gas equation is used for calculation of density. The energy equation has to be solved to obtain the temperature of the fluid which is used for calculating the density.

The momentum equation is discretized using 2nd order upwind scheme, the density using first order upwind scheme, gradients using least squares cell based scheme, volume fraction using QUICK scheme. The K and ϵ equations are discretized using 2nd order upwind scheme with first order scheme for energy. Since the equations are marching with time, first order implicit scheme is used for discretizing the time step. A phase coupled SIMPLE algorithm is used to solve the equations. The under relaxation factors are pressure = 0.1, density = 0.3, body forces = 0.3 and momentum = 0.2, volume fraction = 0.15, turbulent viscosity for = 0.15, energy = 0.3 and turbulent kinetic energy and dissipation rate it is equal to 0.1. A time step size of 0.5 degree per revolution is used with a maximum of 80 iterations per time step. Convergence criterion of 1E-4 is used for all the residuals. In addition to the convergence criteria inlet pressure is also monitored for every time step to assure a constant value is obtained for 1E-4 residual criteria.

For solving inlet body flow domain which is prior to the 1st stage impeller inlet, the above stated solution methods and controls are used for solving steady stage equations using similar convergence criteria.

Figure 4-43 shows the air volume fraction contours on outer surfaces of the inlet body for the flow conditions of 20 kBPD liquid flow rate and 3600 RPM, for GVF of 10% and 50%. From the figures, the inlet body doesn't homogenize the flow, the mixture at the outlet is non-homogenous. Figure 4-44 shows the stream lines of air and water for the flow conditions of 20 kBPD liquid flow rate, 50% GVF and 3600 RPM.

From Figure 4-44 the velocity of air at the inlet is higher in comparison with water, higher air velocity doesn't provide sufficient momentum for mixing instead water stream lines are dominated inside the flow domain.

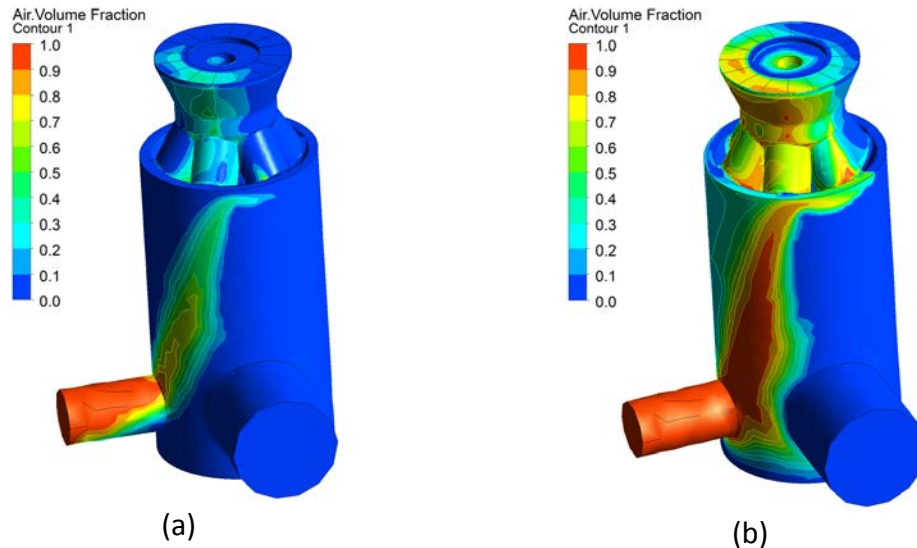


Figure 4-43: Inlet Body air volume fraction contours for the flow conditions of 20 kBPD liquid flow rate, 3600 RPM (a) 10% GVF (b) 50% GVF

Figure 4-45 shows the variation in average mass flow rate of air and water at different zones on the outlet of the inlet body. The increase in mass flow rate of air is offset by the decrease in the mass flow rate of water. The average mass flow rates are used as a boundary condition for simulating the first stage pump performance. The mass flow rate of air is very small in comparison to water but it occupies considerable area at the outlet, Figure 4-46 shows the variation in air volume fraction at the outlet of inlet body across different zones.

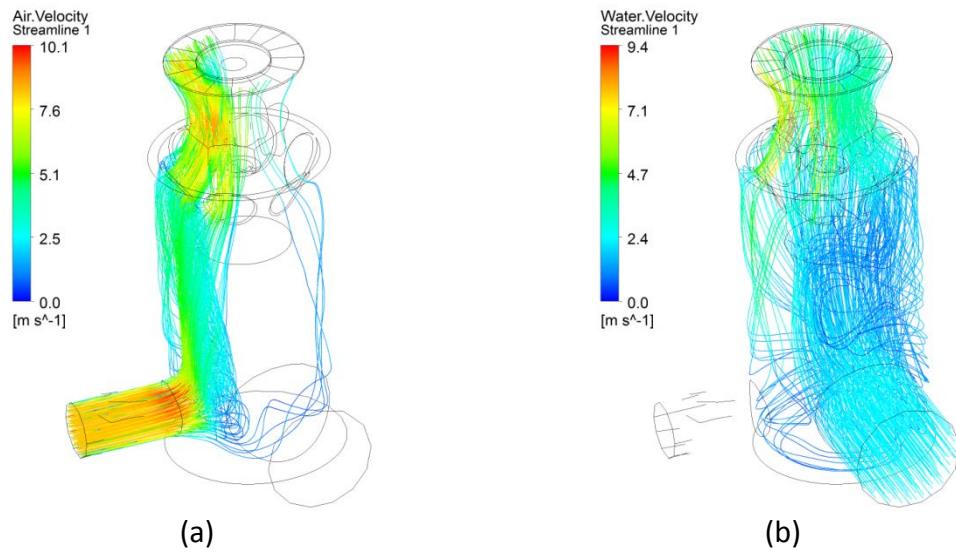


Figure 4-44: Inlet Body stream lines for the flow conditions of 20 kBPD liquid flow rate, 50% GVF and 3600 RPM. (a) Air (b) Water

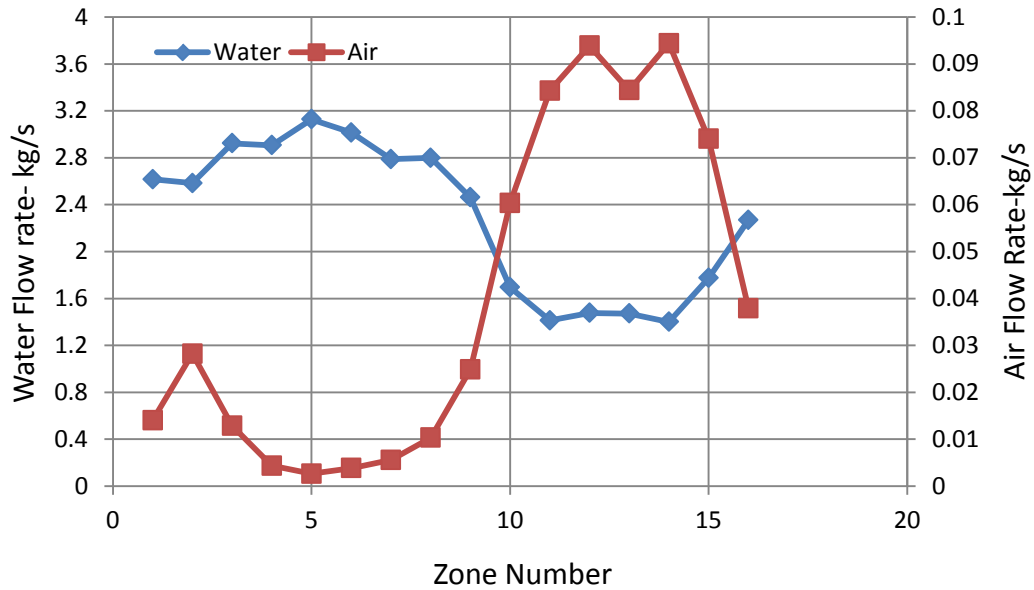


Figure 4-45: Zone wise mass flow rate variation at outlet of inlet body for the flow conditions of 20 kBPD liquid flow rate, 50% GVF and 3600 RPM

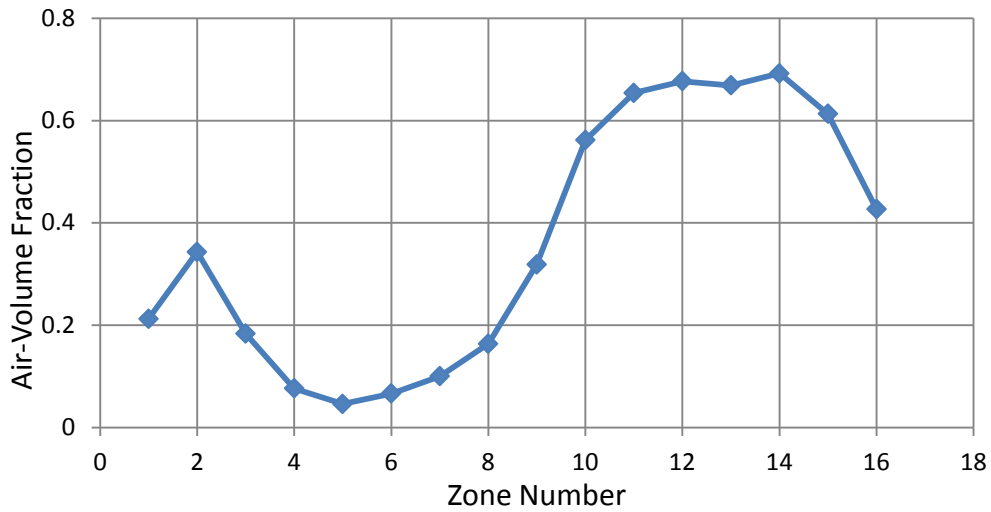


Figure 4-46: Zone wise variation of air volume fraction at outlet of inlet body for the flow conditions of 20 kBPD liquid flow rate, 50% GVF and 3600 RPM

Figure 4-47 shows the two phase performance comparison of experimental and simulation results for the 1st stage pump. Calculations are performed for liquid flow rates ranging from 20 to 30 kBPD, varying GVF from 10% to 50% at a running speed of 3600 RPM and pump inlet pressure of 200 psig. For these simulations stage inlet boundary conditions are obtained from simulating the inlet body. Since the simulations are carried out at different rotational speed in comparison with flow visualization data (4.2.2), bubble diameter is calculated using the relation from Murukami et al. (1974a), the equation is

$$d_m \propto N^{-3/4} \quad 4-4$$

Where d_m is the mean diameter and N is the rotational speed.

A constant bubble diameter is used for simulating the flow field. The diameter is varied for different flow conditions to obtain the experimental pressure rise. The range

of the bubble diameter for 1st stage is 100 to 250 microns. From Figure 4-47, simulation results agree well with the experimental data considering the standard deviation of the measurements. The difference for the mean between the two is due to specifying constant bubble diameter for the total flow field although there is a pressure change as the flow traverses through the pump and flow being non-homogenous at the inlet. Secondary flows from the bearing clearances are also neglected.

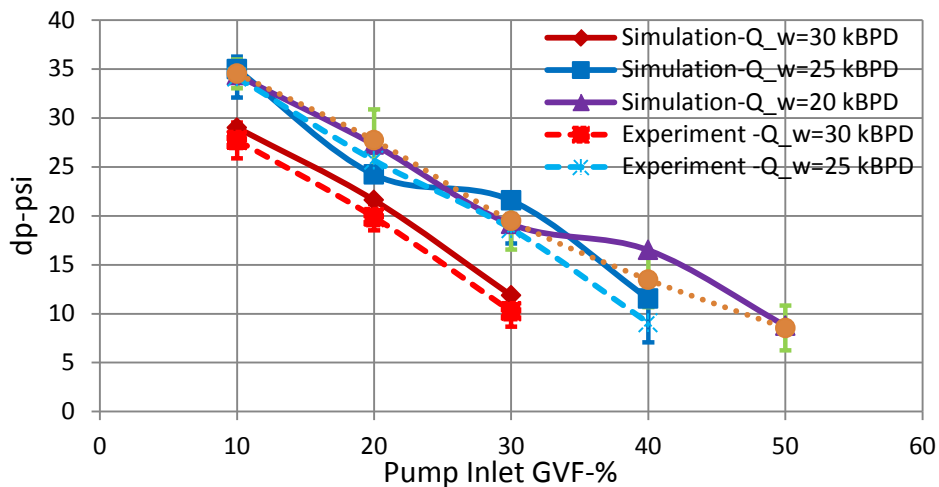


Figure 4-47: Two phase performance comparison of simulation and experimental results for 1st stage

Figure 4-48 shows the performance comparison of simulation and experimental results for the second stage. Simulations are carried out for diffuser1-impeller2-diffuser2 fluid domain with homogenous boundary conditions at the inlet of the diffuser1. Since the pressure is higher and GVF is lower in the second stage in comparison to the first stage, smaller bubble diameters are used. For the simulated flow conditions bubble diameter is varied from 10 to 150 microns. From the graph the simulation results agree well with the experimental data.

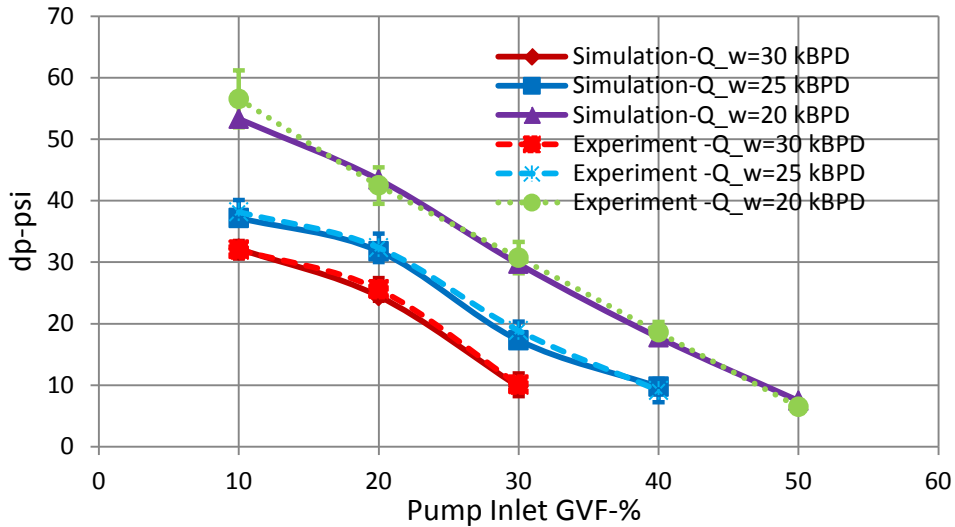


Figure 4-48: Two phase performance comparison of simulation and experimental results for 2nd stage

The purpose of a helico-axial pump in a two phase flow system is to homogenize the flow. Figure 4-49 shows the variation in GVF across three different planes as the flow traverses through the 1st stage pump. At the inlet to the pump as shown in Figure 4-49(a), the flow is non homogenous because of no premixing. As the flow passes through the pump, transfer of centrifugal forces generated by the impeller to the fluid causes partial mixing as shown in Figure 4-49(b). The diffuser is used to direct the flow and it doesn't provide any mixing of flow as shown in Figure 4-49(c). At the outlet of the diffuser due to the separation of the flow in the diffuser regions, only water is observed since in the separation zone any amount of air present is entrained by the main flow. Figure 4-50 shows the velocity vectors at the outlet of the diffuser for air and water. From the figure regions for 0% air volume fraction domain there are no outward normal vectors from the surface.

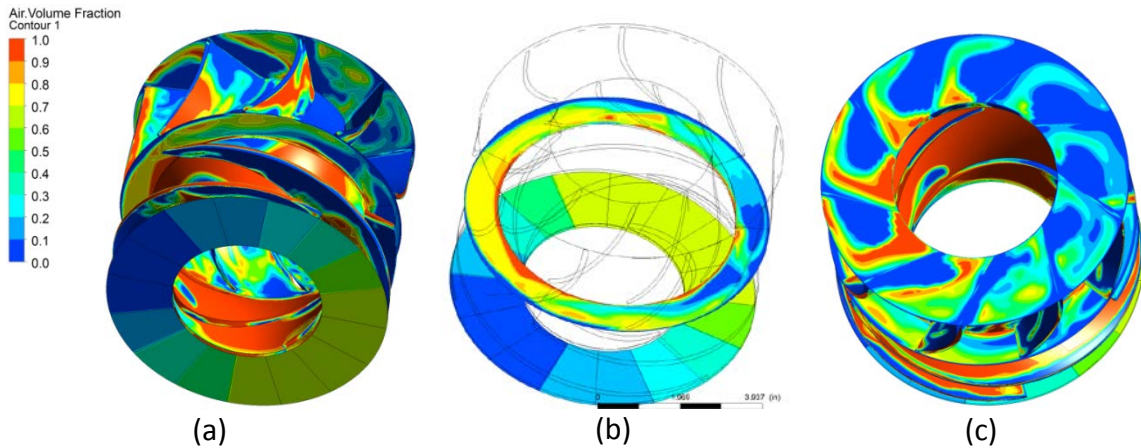


Figure 4-49: 1st stage air volume fraction contours for the flow conditions of 20 kBPd liquid flow rate, 50% GVF, 200 psig inlet pressure and 3600 RPM (a) Impeller Inlet (b) Impeller-Diffuser Interface (c) Diffuser Outlet

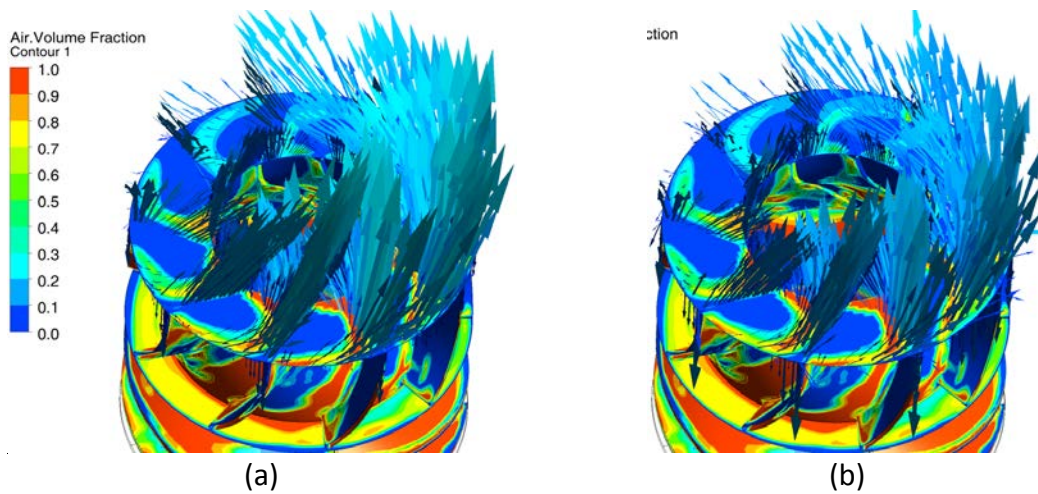


Figure 4-50: 1st stage velocity vectors at diffuser outlet for the flow conditions of 20 kBPd liquid flow rate, 50% GVF, 200 psig inlet pressure and 3600 RPM (a) Water velocity (b) Air velocity

Figure 4-51 shows the air volume fraction contours for the single stage cascade at different spans for the flow conditions of 20 kBPd liquid flow rate, 50% GVF, 200 psig inlet pressure and 3600 RPM. For regions closer to the hub (span=0.1), due to centrifugal forces in the region high concentration of air is observed. Observing the change from the hub to the shroud regions, higher concentrations of air are reduced.

Figure 4-52 shows the air velocity stream lines for the same flow conditions. Since the flow at the inlet is non uniform and the impeller is rotating, there is no accumulation of air in the impeller. Due to non-uniform inlet conditions, the pressure rise across each impeller blade flow path is different and the impeller blades are subject to oscillating pressure variations as shown in Figure 4-53. For the Blade-1 the pressure on the suction side of the blade is higher than the pressure side. The variation across the blade surfaces is different for all of them.

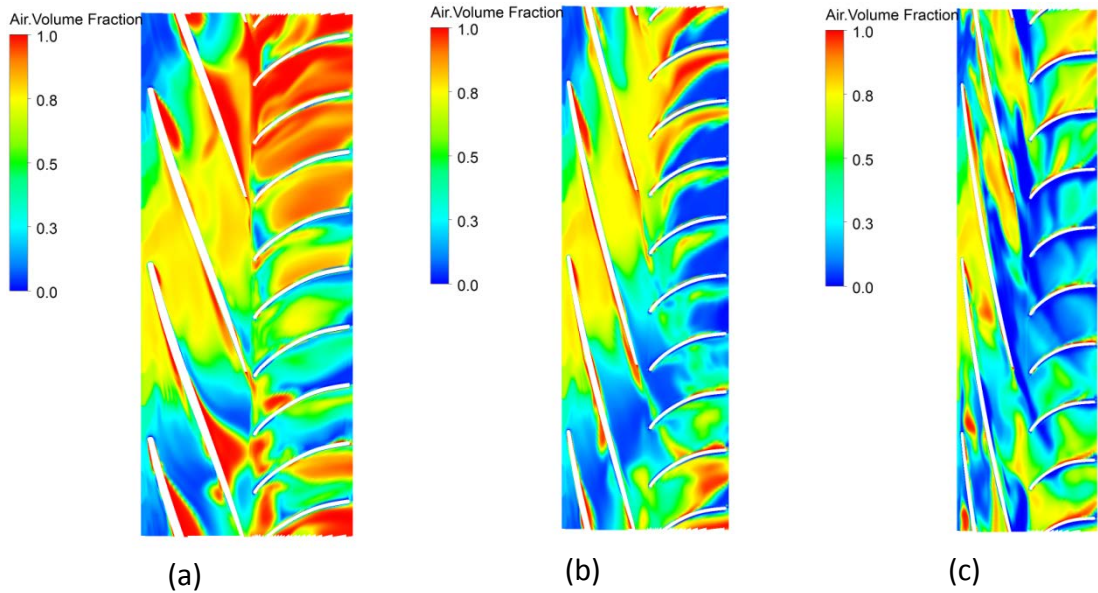


Figure 4-51: 1st stage cascade of air volume fraction contours for the flow conditions of 20 kBPD liquid flow rate, 50% GVF, 200 psig inlet pressure and 3600 RPM (a) Span = 0.1 (b) Span = 0.5 (c) Span = 0.9

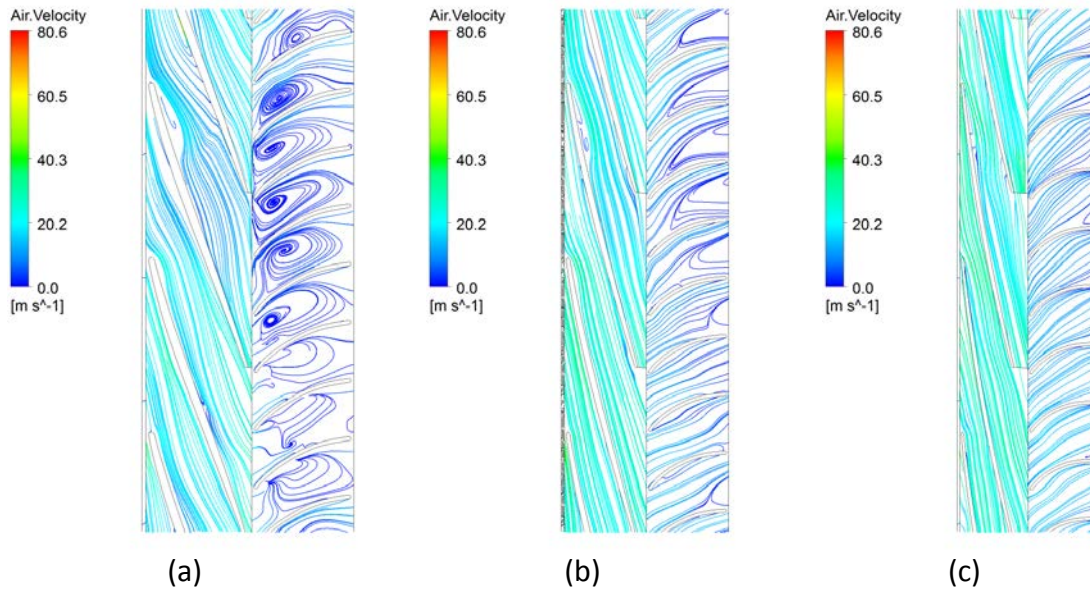


Figure 4-52: 1st stage cascade of air velocity stream lines for the flow conditions of 20 kBPD liquid flow rate, 50% GVF, 200 psig inlet pressure and 3600 RPM (a) Span = 0.1 (b) Span = 0.5 (c) Span = 0.9

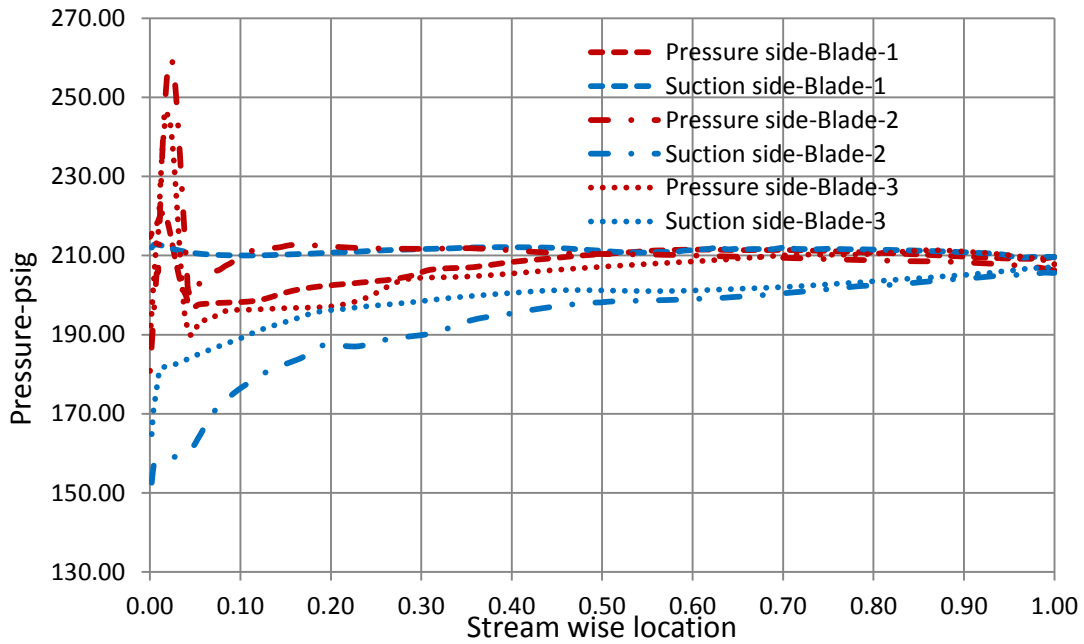


Figure 4-53: Pressure variation on 1st stage impeller blade for the flow conditions of 20 kBPD liquid flow rate, 50% GVF, 200 psig inlet pressure and 3600 RPM at span = 0.5

4.3.3.1 Effect of GVF on liquid flow rate

Figure 4-51 and Figure 4-52 shows the air volume fraction contours and air velocity stream lines for 50% GVF on the 1st stage cascade at different span for the flow conditions of 20 kBPD liquid flow rate, 200 psig inlet pressure and 3600 RPM. Similarly Figure 4-54 and Figure 4-55 shows the air volume fraction contours and air velocity stream lines for 10% GVF and with other flow conditions the same.

From the air volume fraction contours, for the 10% GVF condition, the concentration air is more at the hub of the impeller and it decreases as we move from hub to shroud with trace amount of air closer to the shroud. Similarly for the 50% condition it is more at the hub, as we move from hub to shroud the variation is minimal. For 10% GVF condition at span=0.1 high concentration of air (red zones) is observed in the impeller, as the fluid traverse from inlet to outlet due to pressure rise in the impeller, air gets compressed and the volume fraction of air in the diffuser is reduced. Similar phenomena is not observed for 50% GVF since pressure rise is low. From the air velocity stream lines at span = 0.1 for 10% GVF, the stream lines are not aligned in the impeller blade orientation due to lower amount of air where blob of air is entering the impeller blade path as it rotates. For the 50% GVF condition at span = 0.1, due to large amount of air velocity stream lines are aligned with the blade orientation with recirculation zones on the pressure side.

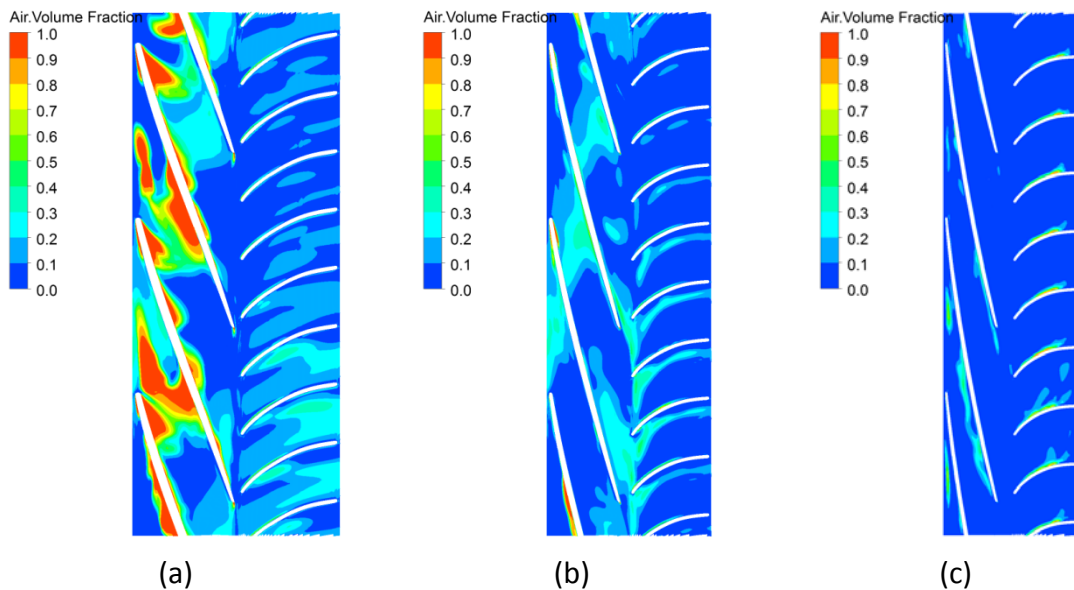


Figure 4-54: 1st stage cascade of air volume fraction contours for the flow conditions of 20 kBPD liquid flow rate, 10% GVF, 200 psig inlet pressure and 3600 RPM (a) Span = 0.1 (b) Span = 0.5 (c) Span = 0.9

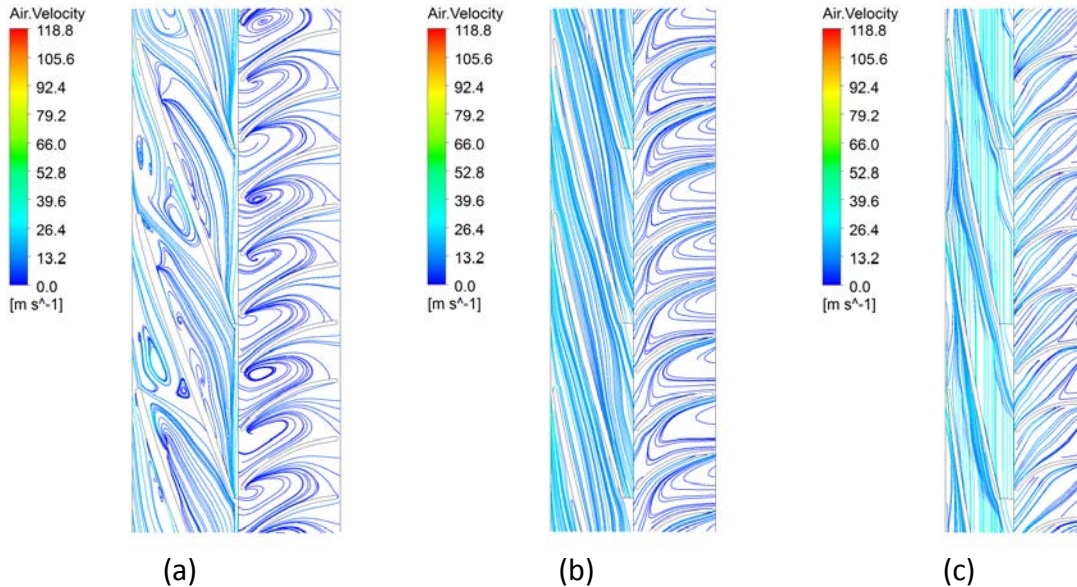


Figure 4-55: 1st stage cascade of air velocity stream lines for the flow conditions of 20 kBPD liquid flow rate, 10% GVF, 200 psig inlet pressure and 3600 RPM (a) Span = 0.1 (b) Span = 0.5 (c) Span = 0.9

4.3.3.2 Effect of GVF on total flow rate

Two different flow conditions with similar total flow rate are evaluated to study the effect of GVF. 20 kBPD liquid flow rate, 40% GVF and 30 kBPD liquid flow rate, 10% GVF have similar total flow rate of 33.3 kBPD.

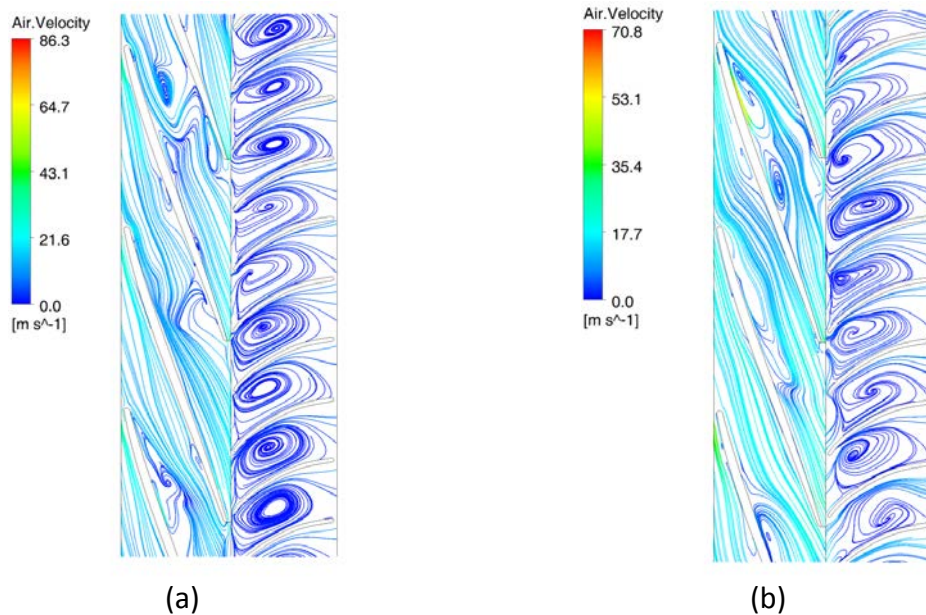


Figure 4-56: 1st stage cascade of air velocity stream lines for the flow conditions of 200 psig inlet pressure and 3600 RPM at span=0.1 for (a) 30 kBPD liquid flow rate, 10% GVF (b) 20 kBPD liquid flow rate, 40% GVF

Figure 4-56 shows the 1st stage cascade of air velocity stream lines at span=0.1 for similar total flow rates but different liquid and gas flow rates. Similarly Figure 4-57 shows the air volume fraction contours. From Figure 4-56(b) and Figure 4-57(b) for 40% GVF in the impeller flow path there are strong stationary gas pockets on the pressure side for the three impeller blades which reduces the effective flow area. For the low GVF condition stationary gas pocket is observed on the pressure side of the impeller

blade but the location varies on each impeller blade due to high velocity water moves the air pocket. Due to continuous stationary gas pockets and also the work loss in compressing gas, the head for high GVF condition is reduced by 50%. For reducing the head loss, impeller blade profiles have to be designed to minimize gas pockets formation.

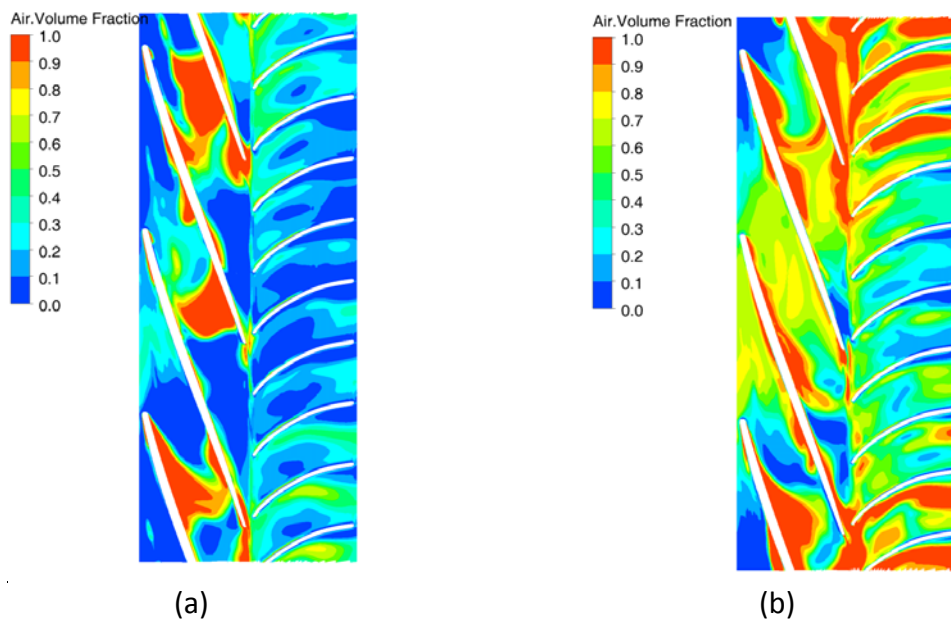


Figure 4-57: 1st stage cascade of air volume fraction contours for the flow conditions of 200 psig inlet pressure and 3600 RPM at span=0.1 for (a) 30 kBPD liquid flow rate, 10% GVF (b) 20 kBPD liquid flow rate, 40% GVF

4.3.3.3 Effect of Stage Number

Figure 4-58, Figure 4-59 and Figure 4-60 show the comparison of air velocity stream lines , air volume fraction and air velocity contours for 1st stage and 2nd stage cascade at span=0.1 for the pump inlet flow conditions of 25 kBPD liquid flow rate, 200 psig inlet pressure, 20% GVF and 3600 RPM. Due to pressure rise in the 1st stage the

actual GVF at the inlet of second stage is 18% and due to mixing in the first stage the flow is almost uniform at second stage inlet. Since the flow is uniform at the inlet of the second stage, air volume fraction contours (Figure 4-59(b)) and air velocity stream lines (Figure 4-58(b)) are uniform across the blade passages. From Figure 4-58(a) for the first stage because of non-uniform inlet conditions, air streams lines are not aligned in the blade orientation, from velocity contours in Figure 4-60(a) the flow is stationary and it occupies the whole gap between the blades. The region where the air velocity is zero, from Figure 4-59(b) it is completely filled with air. Due to this the head developed by the first stage is 35% lower than the second stage for this particular flow condition.

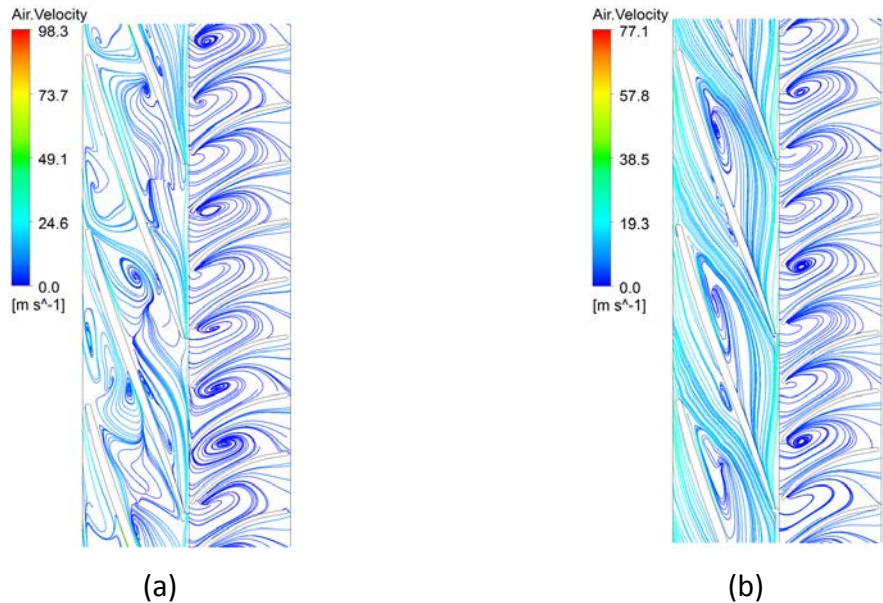


Figure 4-58: Cascade of air velocity stream lines at span=0.1 for the flow conditions of 25 kBP liquid flow rate, 20% GVF, 200 psig inlet pressure and 3600 RPM (a) 1st stage (b) 2nd stage

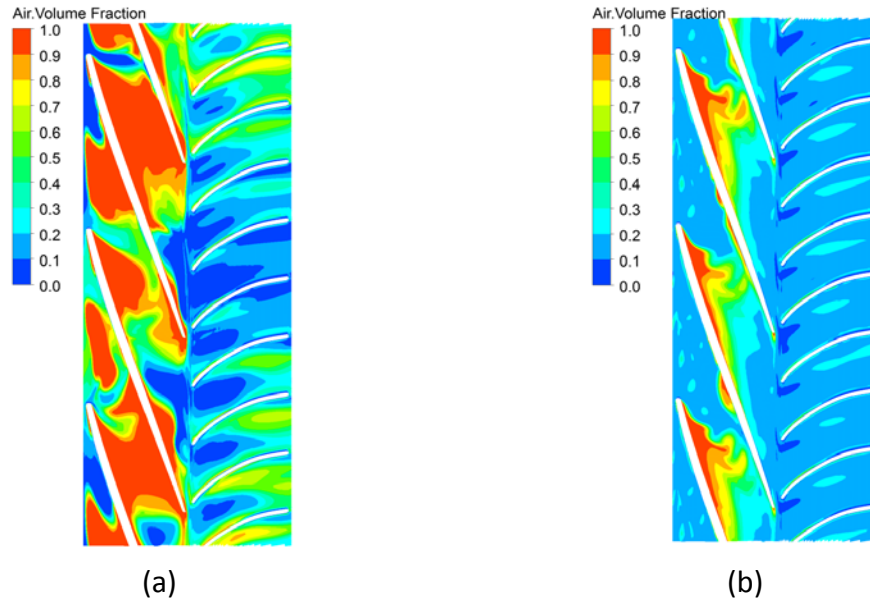


Figure 4-59: Cascade of air volume fraction contours at span=0.1 for the flow conditions of 25 kBPD liquid flow rate, 20% GVF, 200 psig inlet pressure and 3600 RPM (a) 1st stage (b) 2nd stage

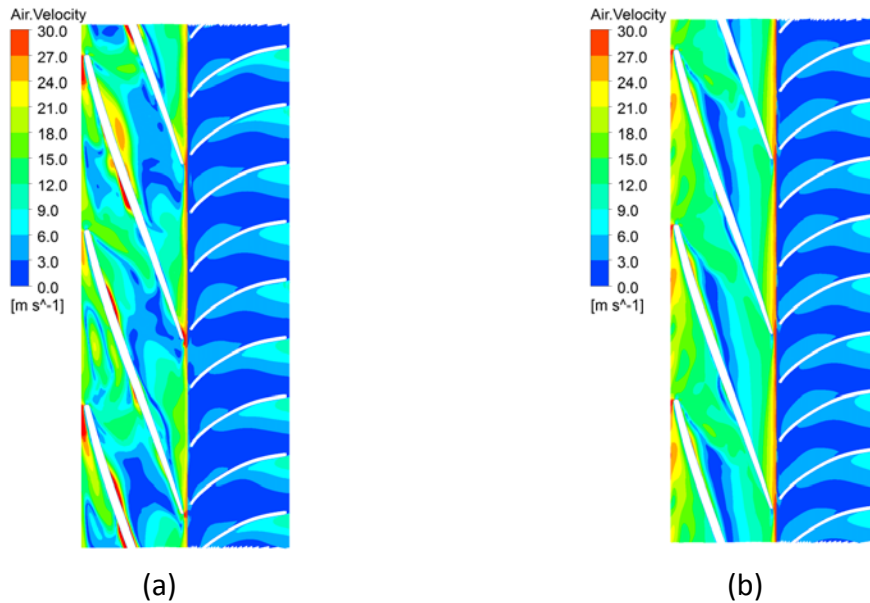


Figure 4-60: Cascade of air velocity contours at span=0.1 for the flow conditions of 25 kBPD liquid flow rate, 20% GVF, 200 psig inlet pressure and 3600 RPM (a) 1st stage (b) 2nd stage

4.3.3.4 Effect of Liquid Flow Rate

Figure 4-61 and Figure 4-62 show the 2nd stage comparison of air volume fraction contours and air velocity stream lines for liquid flow rate of 20 kBPD and 30 kBPD for the flow conditions of 28% GVF, 215 psig inlet pressure and 3600 RPM. From the Figure 4-61(a) for span=0.1 at 20 kBPD liquid flow, air is accumulated on the impeller flow path due to lower axial velocity and the accumulation area decreases with increase in liquid flow rate. Since air accumulation zone occupies the complete flow area of impeller blade at span =0.1 for lower liquid flow rate, the corresponding air velocity stream lines are not aligned with the main flow as shown in Figure 4-62(a).

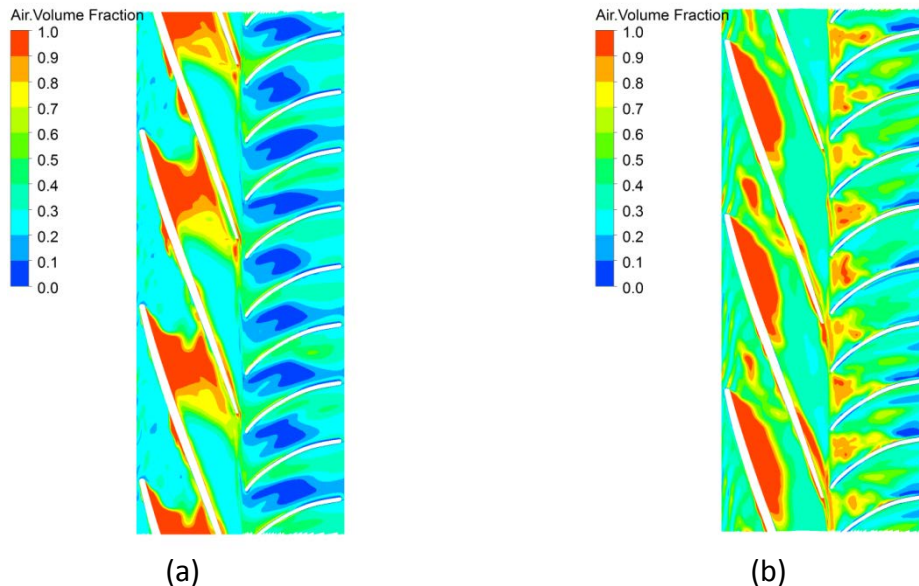


Figure 4-61: 2nd stage cascade of air volume fraction contours for the flow conditions of 28% GVF, 215 psig inlet pressure and 3600 RPM at span=0.1 for different liquid flow rates (a) 20 kBPD (b) 30 kBPD

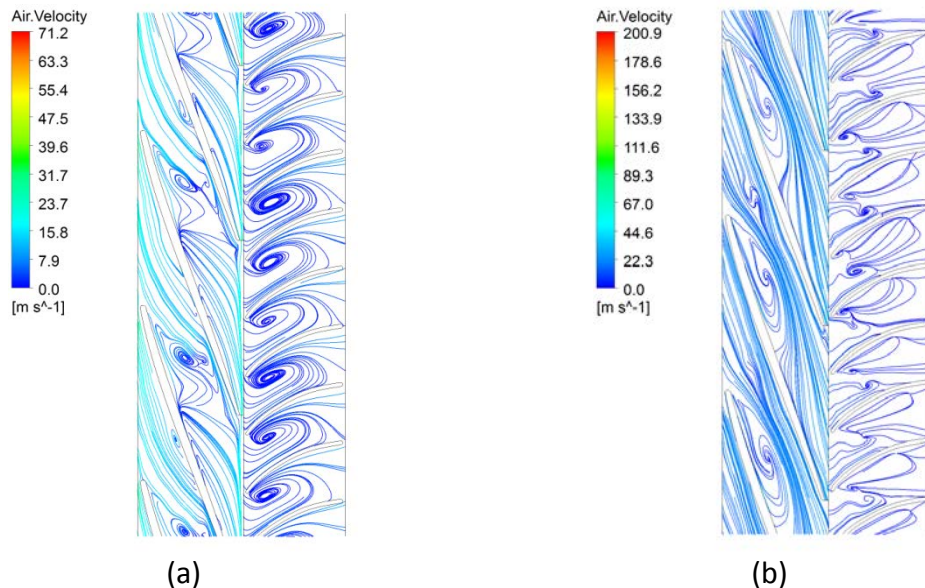


Figure 4-62: 2nd stage cascade of air velocity stream lines for the flow conditions of 28% GVF, 215 psig inlet pressure and 3600 RPM at span=0.1 for different liquid flow rates (a) 20 kBPD (b) 30 kBPD

4.3.4 Different Diffuser Designs

The main disadvantage of the helico-axial pump in comparison with other mixed flow pumps is the head produced decreases considerably with increase in flow rate. Figure 4-40 shows the 2nd stage cascade stream lines for 35 kBPD liquid flow rate and 3600 RPM, this flow condition is the BEP of the pump. From this figure for span=0.1 and 0.5 in the diffuser, considerable flow area is occupied by a separation zone which extends close to the outlet of the diffuser. Due to this the flow is non uniform at the inlet of the impeller. From Figure 4-35 the pressure rise in the pump is occurring only in the impeller, the pressure rate of increase is higher closer to the inlet of the pump impeller. One way of improving the performance is to increase the length of the diffuser so that the separation zones don't extend close to the outlet of the diffuser.

Two different diffuser combinations with 50% increase in length (design-1) and another with 100% increase in length (design-2) are simulated to study the effect of length on the performance. Since the impeller has 3 blades and the diffuser has 9 blades, there exists a blade passing frequency at 9X times the running frequency. In order to eliminate this, standard way of designing is not to have number of blades in impeller and diffuser which can be multiples. A diffuser with 7-blades (design-3) with standard length is simulated to study this effect on performance. The three designs are simulated using periodic boundary conditions with a specified mass flow rate.

Figure 4-63 shows the comparison of pressure rise for three different designs against standard condition. Two different flow rates are simulated for each design. From the figure with increase in length at higher flow rate the pressure rise is higher, the corresponding increase in pressure is from 35 to 38%. Figure 4-64 and Figure 4-65 shows the velocity stream lines for design-2 and design-3. For span=0.1 and 0.5 with the increase in length the separation zones don't extend close to the outlet of the diffuser. Due to this, a higher pressure rise is obtained. With decrease in flow rate, for increased length design the pressure rise is decreased by 20%. From Figure 4-66 which shows the cascade for different designs at lower flow rate and span=0.5, with increase in diffuser length the separation zone increases and it occupies the whole length of the diffuser because of off design conditions. For change in the number of blades (Design-3), there is no considerable difference in the pressure rise in comparison with standard conditions.

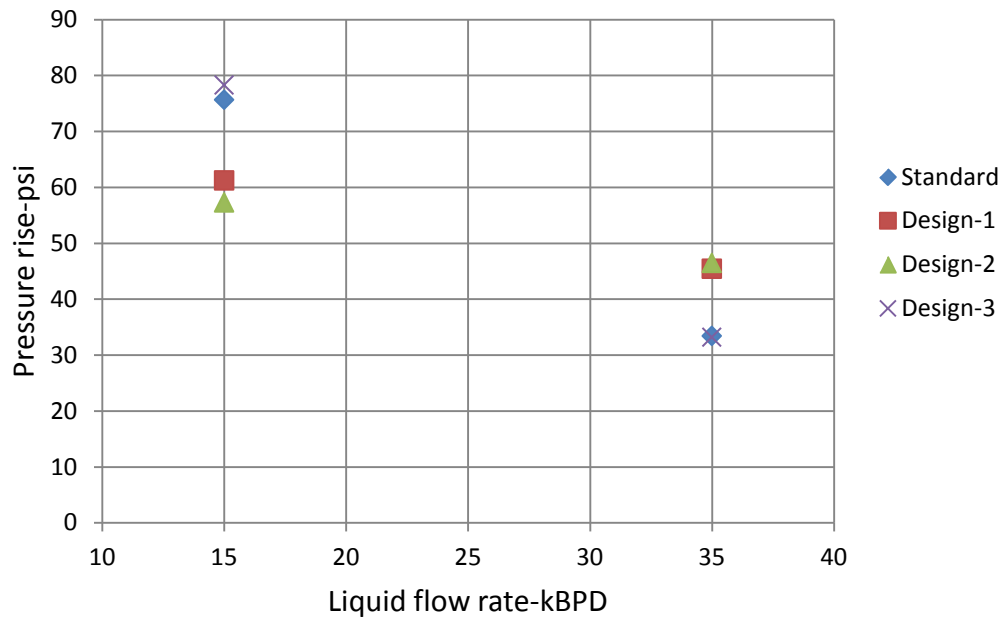


Figure 4-63: Pressure rise comparison for three different designs

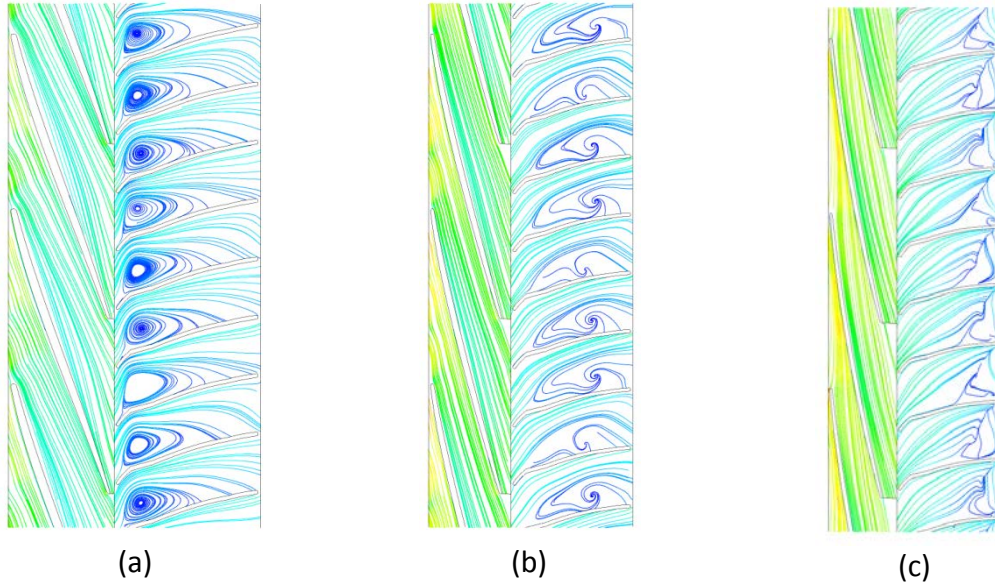


Figure 4-64: Design-2 2nd stage cascade of water velocity stream lines for the flow conditions of 35 kBPD liquid flow rate and 3600 RPM (a) Span = 0.1 (b) Span = 0.5 (c) Span = 0.9

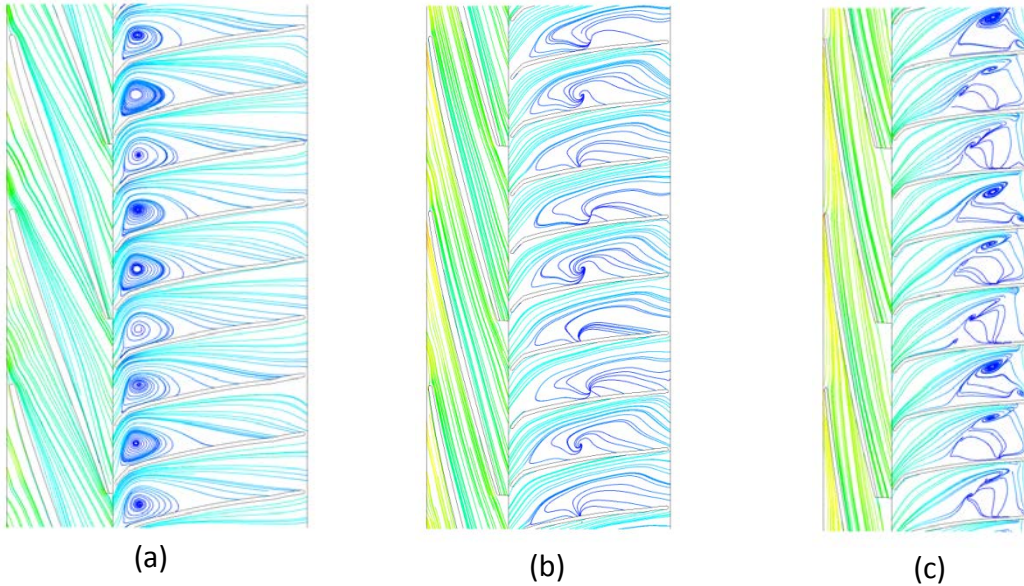


Figure 4-65: Design-3 2nd stage cascade of water velocity stream lines for the flow conditions of 35 kBPD liquid flow rate and 3600 RPM (a) Span = 0.1 (b) Span = 0.5 (c) Span = 0.9

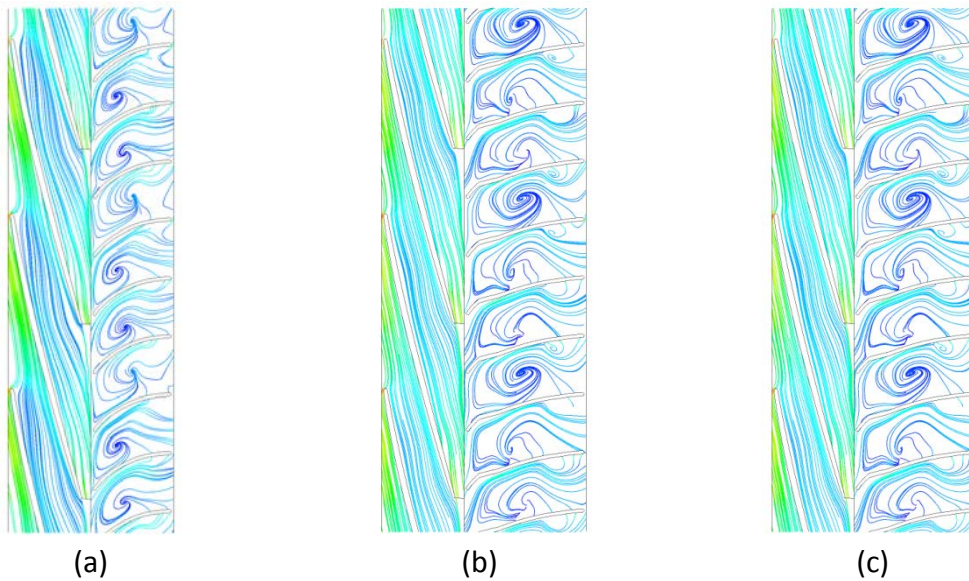


Figure 4-66: 2nd stage cascade of water velocity stream lines for the flow conditions of 15 kBPD liquid flow rate and 3600 RPM at span=0.5 (a) Standard (b) Design-1 (c) Design-2

Figure 4-67 shows the comparison of power obtained from simulations for different designs. For higher flow rates since the pressure rise is higher the power

increases for design-2 and design-3. Correspondingly for the same design at lower flow rates there is a decrease in power because of lower pressure rise. If design-2 or design-3 is chosen, the power capacity of the electric motor can be reduced from 16 to 22% even if the pump had to run at off design conditions.

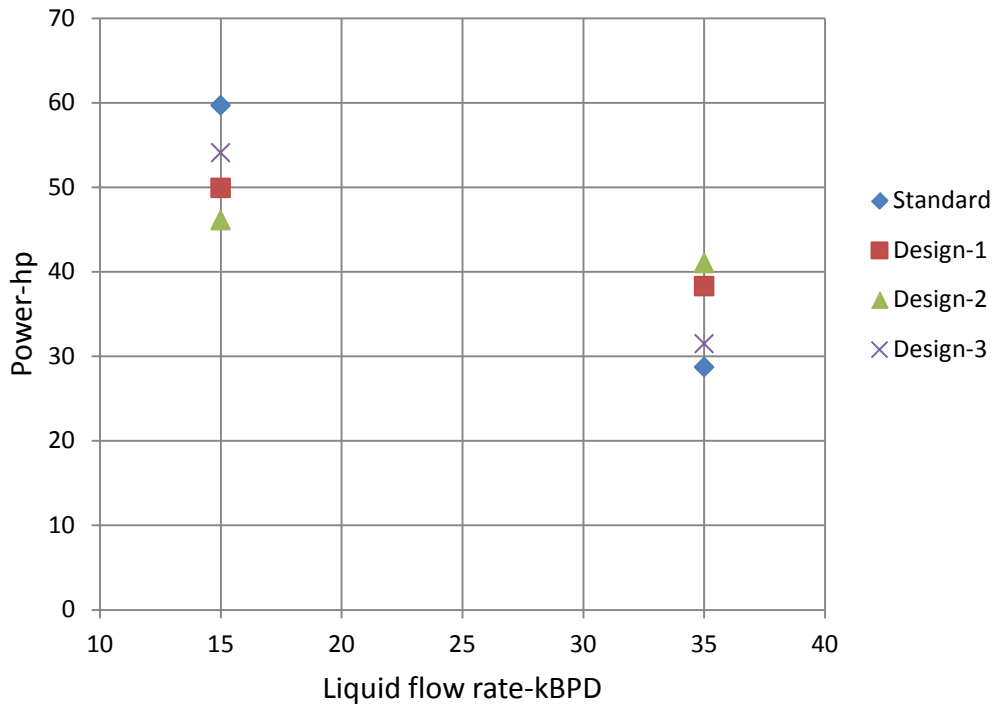


Figure 4-67: Power consumption comparison for three different designs

Figure 4-68 shows the comparison of efficiency and pressure gradient for three different designs at 35 kBPD liquid flow rate and 3600 RPM. For design-1 there is an increase of efficiency by 1% and the pressure rise is increased by 7.5% per unit length of the pump.

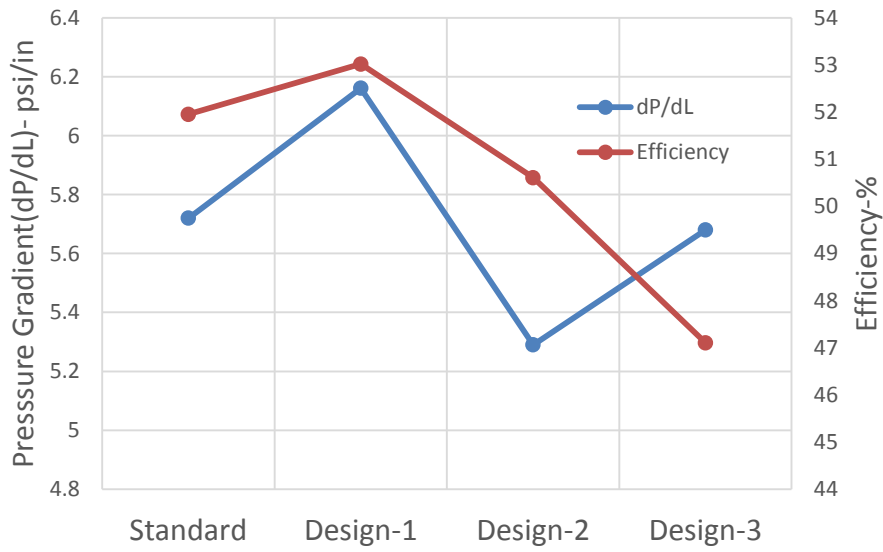


Figure 4-68: Efficiency and Pressure gradient comparison for three different designs at 35kBD liquid flow rate

5 CONCLUSIONS AND RECOMMENDATIONS

In the present study performance evaluation of a helico-axial pump is carried out experimentally and numerically. In the first part of experimental testing, multi-phase performance of an actual 4-stage pump is carried out using water and air as process fluids by varying liquid flow rate, GVF, inlet pressure and rotating speed. From the results, head rise is clearly a function of rotating speed and GVF, with a smaller effect from inlet pressure. Also, the BEP of the pump shifts to lower flow rates with increase in GVF. Detailed pressure measurements on the diffuser provided understanding about the performance and flow behavior, there is no pressure rise in the diffuser. Stage by stage pressure measurements are used to quantify the performance of the individual stages, the first stage performance is different from the subsequent stages. A new empirical model is developed to predict the head rise per stage under single or multi-phase flow conditions with a RMSE of 8.95%. From the vibration measurements, it was observed that the shaft orbit size increases with increase in GVF causing metal to metal contact.

In the second part of experimental testing, flow visualization is carried out on a single stage helico-axial pump using water and air as process fluids. The pump is designed and prototyped using polycarbonate material. Bulk flow visualization is carried out to visualize the two phase flow through the pump. At higher GVF, considerable leakage is observed from the tip clearances. Back flow is observed at the outlet of the pump from pressure side to suction side of the diffuser blade. Also 50% of

the diffuser outlet flow area is occupied by recirculation zones. Using laser and high speed camera bubble size is measured for different flow conditions in the impeller, with the average bubble diameter at 350 microns.

Stage by stage 3-D CFD simulations were carried out on two stages of the 4-stage helico-axial pump to understand the flow through the pump using ANSYS Fluent. Single phase simulations were carried out with water as process fluid using Realizable k-epsilon model. The single phase model is validated using experimental data for both the stages. From the simulation results it was observed that much of the pressure rise in the impeller is occurring closer to the inlet of the impeller. To improve the stage performance the diffuser was modified to have a uniform flow at the inlet of the impeller in a multi stage pump. The modified diffuser has shown 7.5% increase in pressure rise per unit length of the diffuser with 1% increase in efficiency at BEP. Two-phase simulations were carried out with water and air as process fluids using Eulerian multi-phase model. The model was validated using experimental data for the two stages. From the two phase simulations it was observed that the head drop at higher GVF was to slip between the phases. Because of this slip, stationary air pockets are observed on the pressure side of the impeller blade while minimizing the flow area. In order to increase the head rise at higher GVF, the impeller blades must be redesigned in order to minimize the occurrence of air pockets. Also single stage is necessary to homogenize the flow under non uniform inlet conditions.

Since these pumps are used for crude oil applications, further testing can be carried out to study the effect of viscosity on performance and empirical model can be improved to include the effect of fluid viscosity. An optical window can be installed in the 4-stage pump to measure the bubble diameter at higher rotating speeds. Since the pump performance has shown improved performance with increased length of the diffuser from single phase simulations, it has to be experimentally validated.

REFERENCES

- Barrios, L. (2007). Visualization and modeling of multiphase performance inside an electrical submersible pump. (PhD Thesis, The University of Tulsa).
- Cao, S., Peng, G., & Yu, Z. (2004). Hydrodynamic design of rotodynamic pump impeller for multiphase pumping by combined approach of inverse design and CFD analysis. *J. Fluids Eng*, 127(2), 330-338.
- Caridad, J., & Kenyery, F. (2002). Performance analysis of electric submersible pumps (ESP) handling two-phase mixtures. Proceedings of ETCE2002, ASME Engineering Technology Conference on Energy, Houston, TX, 747-753.
- Caridad, J., & Kenyery, F. (2004). CFD analysis of electric submersible pumps (ESP) handling two-phase mixtures. *J. Energy Resources Technology*, 126, 99-104.
- Chisley, E. (1997). Two-phase flow centrifugal pump performance. (PhD Thesis, Idaho State University).
- Cirilo, R. (1998). Air-Water Flow through Electric Submersible Pumps. (MS Thesis, The University of Tulsa).
- Croba, D., & Kueny, L. J. (1996). Numerical calculation of 2d, unsteady flow in centrifugal pumps: Impeller and volute interaction. *International J. Numerical Methods in Fluids*, 22, 467-481.
- Duran, J., & Prado, M. (2003, January 1). ESP stages air-water two phase performance-modeling and experimental data. Society of Petroleum Engineers,

- Estevam, V. (2002). A phenomenological analysis about centrifugal pump in two-phase flow operation. (PhD Thesis, Campinas: Faculdade de Engenharia Mecânica, Universidade Estadual de Campinas).
- Gamboa, J. (2008). Prediction of the transition in two-phase performance of an electrical submersible pump. (PhD Thesis, The University of Tulsa).
- González, J., Fernández, J., Blanco, E., & Santolaria, C. (2002). Numerical simulation of the dynamic effects due to impeller-volute interaction in a centrifugal pump. *Transactions of the ASME*, 124, 348-355.
- González, J., & Santolaria, C. (2006). Unsteady flow structure and global variables in a centrifugal pump. *J. Fluids Engineering*, 128, 937-946.
- Kirkland, K. (2012). Design and fabrication of a vertical pump multiphase flow loop. (MS Thesis, Texas A&M University).
- Lakshminarayana, B. (1991). An Assessment of computational fluid dynamic techniques in the analysis and design of Turbomachinery—The 1990 freeman scholar lecture. *J. Fluids Eng*, 113(3), 315-352.
- Lea, F. J., & Bearden, L. J. (1982). Effect of gaseous fluids on submersible pump performance. *J. Petroleum Technology*, 2922-2930.
- Majidi, K., & Siekmann, E. H. (2000). Numerical calculation of secondary flow in pump volute and circular casings using 3D viscous flow techniques. *International J. Rotating Machinery*, 6(4), 245-252.

- Majidi, K. (2005). Numerical study of unsteady flow in a centrifugal pump. *J. Turbomachinery*, 127, 363-371.
- Marchetti, M. J. (2013). Design, construction, and visualization of transparent full scale high pressure test facility for electronic submersible pumps. (MS Thesis, Texas A&M University).
- Marsis, E., Pirouzpanah, S., & Morrison, G. (2013). Cfd-based design improvement for single-phase and two-phase flows inside an electrical submersible pump. Proceedings of the ASME 2013 Fluids Engineering Division Summer Meeting, Incline Village, Nevada, USA, 1-8.
- Marsis, G. E. (2012). Cfd simulation and experimental testing of multiphase flow inside the.mvp electrical submersible pump. (PhD Thesis, Texas A&M University).
- Medvitz, B. R., Kunz, F. R., Boger, A. D., Lindau, W. J., Yocum, M. A., & Pauley, L. L. (2002). Performance analysis of cavitating flow in centrifugal pumps using multiphase CFD. *J. Fluids Engineering*, 124, 377-383.
- Murukami, M. M., Kiyoshi. (1974a). Effects of entrained air on the performance of a centrifugal pump. 1st report, performance and flow conditions. *Bulletin of JSME*, 17(110), 1047-1055.
- Murukami, M., & Minemura, K. (1974b). Effects of entrained air on the performance of centrifugal pumps: 2nd report, effects of number of blades. *Bulletin of JSME*, 17(112), 1286-1295.
- Nguyen, T. (2011). Advanced artificial lift methods-PE 571[PowerPoint Slides].

- Pessoa, R. Experimental investigation of two-phase flow performance of electrical submersible pump stages. (MS Thesis, The University of Tulsa). 2000,
- Pirouzpanah, S. (2014). Experimental measurement of multiphase flow and CFD erosion modeling in electrical submersible pumps. (PhD Thesis, Texas A&M University).
- Poullikkas, A. Effects of two-phase liquid-gas flow on the performance of nuclear reactor cooling pumps. *Progress in Nuclear Energy*, 42(1), 3-10.
- Romero, M. (1999). An evaluation of an electric submersible pumping system for high GOR wells. (MS Thesis, The University of Tulsa).
- Sato, S., Furukawa, A., & Takamatsu, Y. (1996). Air-water two-phase flow performance of centrifugal pump impellers with various blade angles. *JSME International Journal*, 39(2), 223-229.
- Schilling, R., & Frobenius, M. (2002). Numerical simulation of the two phase flow in centrifugal pump impeller. *Asme Fedsm*, Montreal, Quebec, Canada. pp. 859-865.
- Schlumberger (2000). *Gas Lift Design and Technology*.
- Sekoguchi, K., Takada, S., & Kanemori, Y. (1984). Study of air-water two-phase centrifugal pump by means of electric resistivity probe technique for void fraction measurement. *Bulletin of JSME*, 27(227), 931-938.
- Tremante, A., Moreno, N., Rey, R., Noguera, R. (2002) Numerical Turbulent Simulation of the Two Phase Flow (Liquid/Gas) Through a Cascade of an Axial Pump. *ASME.J. Fluids Eng*, 124(2), 371-376.

Trevisan, E. F. (2009). Modeling and visualization of air and viscous liquid in electrical submersible pump. (PhD Thesis, The University of Tulsa).

Turpin, L. J., Lea, F. J., & Bearden, L. J. (1986). Gas-liquid flow through centrifugal pumps-correlation of data. Proceedings of Third International Pump Symposium, 13-20.

Zhang, J., Zhu, H., Wei, H., & Peng, J. (2011). Performance test of a 5-stage helico-axial multiphase pump.52-54, 399-404.